Department of Precision and Microsystems Engineering

Sensor Calibrations with the Improved Picodrift Interferometer

Yuze Yang

Report no : MSD 2017.054
Coach : Dr. A.S. van de Nes, Ir. J.W. Spronck
Professor : Prof. Dr. Ir. J.L. Herder
Specialisation : Mechatronic System Design
Type of report : Master Thesis
Date : November 13, 2017

TU Delft Delft University of Technology

Challenge the future

Sensor Calibrations with the Improved Picodrift Interferometer

by

Yuze Yang

For the degree of Master of Science in Mechanical Engineering

at Delft University of Technology,

to be defended publicly on Monday November 13, 2017 at 12:00.

Student number: 4502051
Department: Precision & Microsystems Engineering (PME)
Project duration: October 31, 2016 – November 13, 2017

Thesis committee:

Prof. Dr. Ir. J.L. Herder	TU Delft
Dr. A.S. van de Nes	VSL (Dutch Metrology Institute)
Prof. Ir. J.W. Spronck	TU Delft
Prof. Dr. Ir. G.V. Vdovine	TU Delft

The work in this thesis was supported by VSL.

Abstract

To meet the growing demand for high precision measurement equipment, sensors with sub-nanometer resolution are becoming readily available. However, these sensors should be made traceable to a national measurement standard in order to make their results useful for comparison. Because of its high precision, traceability and ease of use, the interferometer stands out for high precision measurements. However, the laser beam of an interferometer can be influenced by temperature and pressure fluctuations. Compensation of this error is possible by sensing temperature and pressure fluctuations while performing interferometric measurements. Alternatively, a refractometer running parallel with the interferometer can be used to do the same compensation with a higher accuracy. Additionally, errors caused by external sources such as vibrations, can be compensated by adopting a highly symmetrical design. Picodrift interferometer was developed and upgraded at VSL as a calibration facility for high-precision sensors.

First, the improved design of the picodrift interferometer is evaluated, implemented and tested allowing for a controlled measurement environment and high stability. The design requirements are determined to reduce the uncertainty caused by temperature and pressure fluctuations to picometer level in one hour. Based on those requirements, a vacuum system is implemented and tested to reach a pressure level in the ultra-high vacuum regime. During the implementation, necessary experiments and tests are performed to find leakages and the reasons for an undesired beam drift related to the pressure change. Additionally, an active temperature control system with passive shield is installed. Also, various kinematic coupling mount systems are designed and manufactured to provide a good positioning stability even in a noisy environment caused by a turbo pump. As the number of the interferometer channels has been doubled to perform measurements in both vacuum and atmospheric conditions, a well planned alignment procedure is developed to align the more sophisticated optical path. To characterize the performance of the new interferometer, a dead path measurement is performed.

Second, to take advantage of the high precision and traceability, the interferometer is expanded to work as a calibration facility for external sensors of different sizes. A stable symmetrical calibration setup is designed to fit in a limited space for external measurements while minimizing uncertainty caused by temperature fluctuation and misalignment. An alignment procedure for the setup is developed. Eventually an example calibration is performed.

Acknowledgments

It is a great honor for me to work on this project at VSL. Everyday there I was surrounded by so many nice colleagues. Working in the well equipped laboratory is such a valuable experience. Firstly, I'd like to thank my daily supervisor Arthur van de Nes, who spent a lot of time and effort explaining me optical knowledge, coaching me to work on the sophisticated setup, discussing possible solutions to problems and so much more. I would like to thank Maurice Heemskerk and Siem Voogt for manufacturing all the customized parts and the advice on practical design. I would also like to thank Richard Koops and Gerard Kotte for helping me on the measurement setups and useful instructions on metrology.

Secondly, I would like to thank Jo Spronck for his tremendous help during the project. I was inspired by his critical and creative thinking in mechatronic systems. His passion and positive attitude have a big influence on me. I would also like to thank my fellow students for their interest in my project and helping me out of difficult problems.

Lastly, I would like to thank my family and friends for their love all the time.

Yuze Yang
Delft, November 2017

Contents

Chapter 1

Introduction

1.1 Background

Precision machines rely on the perfect cooperation of many different parts. A small undesired deviation may be accumulated by the following subsystems and causes a much larger error in the end. A source of deviation is quantified in terms of stability also relating to drift. Drift can be caused by temperature variation, pressure variation, external stress, electromagnetic fields, humidity, relaxation from stress after being manufactured or aging. By sensing temperature, pressure or external/internal force, drift can be compensated for based on physical laws. But aging and manufacture process caused drift poses a bigger challenge. In addition, more and more high-tech machines use hybrid materials which contain many layers of different materials together or new alloys to have some specific mechanical or electrical property. By measuring the material under different conditions, a specific set of drift parameters can be established, and the material can be characterized. This information could be used to compensate the error under same working situation. All these dependencies require a tool to do reliable measurements under different environment conditions and needs to be compatible with various sizes of materials.

For this purpose, VSL in collaboration with the TU Delft and TNO have designed and built an interferometer to measure dimensional drift. After individual components are characterized, decisions like material suitability for stability requirements can be made. Additionally, with this information, errors can be corrected with high accuracy. Because the drift is on picometer level, this instrument was called the picodrift interferometer.

Picodrift interferometer

An interferometer makes use of the wave property of laser light which consisting of a high coherent beam of light to measure length with high resolution and precision. Visible light has a wavelength of hundreds of nanometer, the resolution of an interferometer can reach down to the sub nanometer level. Because of its high precision and contact-less interface, an interferometer is widely used to perform measurements with high precision requirements in geometrical metrology.

J.D. Ellis [1] has designed a picodrift interferometer dedicated to measure dimensional drift of materials. It is a highly symmetrical, double sided heterodyne interferometer. There is a refractometer running parallel with the interferometer implemented, therefore change of refractive index and error caused by vibration can be corrected simultaneously.

After his work was demonstrated, the interferometer was transferred to VSL. It was improved for better frequency stabilization, thermal isolation and being equipped with more advanced electronic

instruments [2]. Still, there are several shortcomings that limit its ease of use and application. In this thesis a follow-up stage is implemented in order to build up an improved version which can be used under a controlled environment from ambient atmosphere to vacuum with external active temperature control.

An advanced interferometer is more than optical elements, it consists of electrical systems and mechanical systems as well. Figure 1.1 is an overview of the picodrift interferometer. To obtain good results with high stability and low noise, the requirements for the laser input is very high in terms of intensity, polarization and frequency stability. So in the laser preparation system there are subsystems like the laser source, optical systems to select and clean the polarization, a control system to lock the frequency. The middle dashed block indicates where the actual interference measurement happens. The laser will interact with the measured sample. Additionally, to compensate the influence of fluctuation of refractive index, which will cause a large error contribution, a refractometer is running parallel with the interferometer. Afterwards, the interfered signal is captured by a photo detector and transformed to an electrical signal. This signal is converted to a digital signal and processed to deliver the final result in length unit.

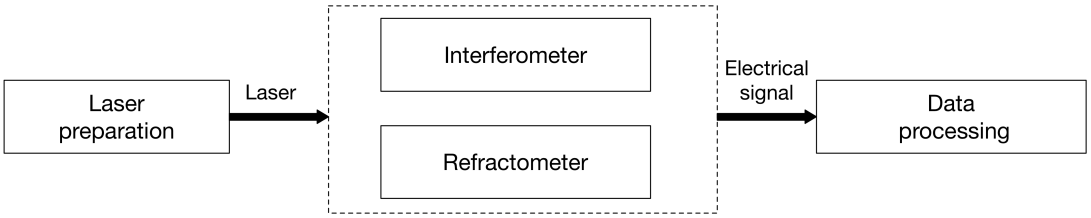

Figure 1.1: Overview of the picodrift interferometer with subsystems.

1.2 Problem definition

Before the start of this thesis, the basic concept has been developed. This thesis covers the process of the implementation of the concept and development of systems that fulfill the requirements to make sure the interferometer works as designed. A further step is taken to develop a subsystem that enables an additional function to do calibration on external sensors like capacitive sensor or interferometers making use of its high stability and traceability.

Implementation

As the interferometer is designed to do measurements on picometer level, the instrument itself must be ultra stable. Therefore the mounting of each optical elements needs to be carefully designed, manufactured and installed. Because of the limitation of space, each part is customized to fit perfectly. Additionally, all optical elements need to be aligned to work in the desired way. So adjustment has to be possible in required degrees of freedom.

Apart from that, some light properties are sensitive to environment conditions. Temperature, pressure and humidity variation will change the refractive index of the medium and cause a variation of the wavelength. Because the wavelength is the key element in length or displacement measurements, it must be kept as stable as possible. So the environment of the instrument should be well controlled. The temperature can be controlled by isolation or implementation of heat sources with a feedback control loop. In terms of pressure, optical systems are normally put in a vacuum condition where the change of pressure can be significantly low and could be monitored easily. However, the vacuum environment puts additional requirements on the design of the mechanical systems. All

the materials and structures should be vacuum compatible for low outgassing rates and no gas in evacuated components can be trapped in the structure.

After the setup is well designed, a good alignment procedure is also an essential factor for the performance of the setup. This requires the knowledge of optical elements, geometry modeling and simulation.

Calibration

A second topic covered in this thesis is the design of a calibration setup, which can take the advantage of the developed high precision traceable instrument to do calibrations on other measurement instruments. The challenge here is to make sure the length or displacement being measured is presented equally the same to both the calibrating and calibrated setup. To minimize errors down to picometer level, lots of factors should be taken into consideration. First of all, a mounting system with precise adjustment mechanism need to be designed. And methods to align all parts in the desired position should be developed. Other problems like temperature expansion related deformation and humidity causing capacitive sensor errors increase the difficulty of the design.

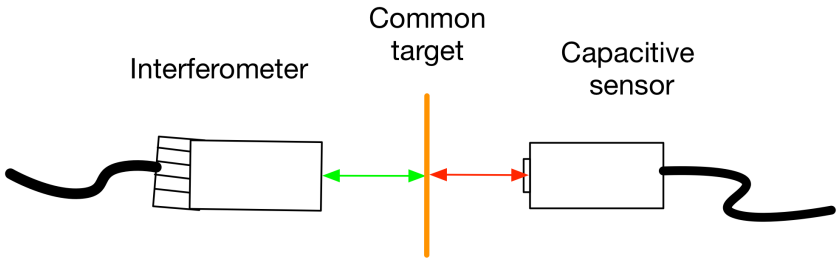

Figure 1.2: Illustrative example of calibration concept.

Figure 1.2 shows an illustrative example of the calibration setup. Both the interferometer and the capacitive sensor are facing a common target. The green and red arrows indicate the sensitive distance for the interferometer and capacitive sensor. When the target moves strictly to the left or right, it will present displacements with same magnitude but opposite directions to both sensors. Ideally the magnitude should be the same. However due to misalignment of the interferometer or capacitive sensor, a cosine error will occur. Thermal expansion of the target, probes or mounting materials will cause additional error.

1.3 Thesis objective

One focus of this thesis is to implement a new interferometer based on an improved concept. The realization covers the design of mounting systems with high stability, moreover creating a well controlled environment for the high precision instrument. Afterwards, a detailed and well organized alignment procedure is developed to guarantee a low uncertainty result. Then the stability of the instrument itself is tested to characterize performance.

More and more precision sensors with sub-nano meter resolution are available on the market. With the picodrift interferometer which has high resolution and traceability, calibration could be performed to help manufactures improve the behavior of their sensor or correct deterministic errors caused by aging or wear. So the second problem to be tackled in this thesis is to develop a sub-system for the picodrift interferometer to perform low uncertainty calibration on external sensors.

1.4 Design approach

With the problem and objective defined, a design approach is planned as follow:

- Literature study of the existing picodrift interferometer as well as necessary knowledge of optics.
- Design and construct subsystems, such as adjusters and mounting systems for the benefit of optimal alignment.
- Work on the development of the whole setup including assembly of the temperature controlled vacuum environment.
- Develop alignment procedure.
- Research and analysis of the behavior of the setup.
- Design of the calibration setup, implementation of the setup and demonstration of an example calibration for a capacitive sensor.

1.5 Thesis outline

Chapter 2 discusses the background information. It covers basic optical knowledge relevant for the understanding of the interferometer and the sub-systems such as the production of laser light, stabilization of laser frequency and functions of different optical elements. Detailed working principles of the interferometer are introduced. Improvements for the new upgraded interferometer are discussed.

Chapter 3 describes the effort made to realize the well controlled environment with respect to pressure stabilization and temperature control. A detailed construction of the interferometer is presented. The alignment procedure is developed.

Chapter 4 shows the test result of the interferometer in terms of self stability which is an important quality for high precision measurement instrument.

Chapter 5 presents the development of the calibration setup and some measurement results obtained after it was implemented.

Chapter 6 makes the final conclusion and gives recommendations for future work.

Chapter 2

Background information

2.1 Introduction to metrology

As described by BIPM (International Bureau of Weights and Measures) [3] "metrology is the science of measurement, embracing both experimental and theoretical determinations at any level of uncertainty in any field of science and technology." Its application varies from the weight scale used in the supermarket to the design of spaceship. The most important factors in metrology are standard and traceability. Standard describes specification of a certain unit. Traceability is the relation between the measured result and the standard. Metrology has a long history. Back to 259 BC [4], the first emperor of centralized imperial China Qin Shi Huang unified the standards of weights and measures across the whole country, which led to a boost of development in economy and culture. Now the standard is defined by international organization. There are institutes in each country who are responsible for the traceability to make sure the unit used is referred to the world standard.

2.1.1 Primary standard

There is a world wide acknowledged agreement for each standard unit to define its quantities called primary standard. For example, the international conference on geodesy in 1867 made the first standard of meter, which is simply a bar marked by two lines [5]. The 17th Conférence Générale des Poids et Mesures redefined one meter as the length of the path traveled by light in vacuum during a time interval of 1/299792458 of a second. However, the accuracy of this definition is based on the accuracy of the definition of second. To do this practically, a certain wavelength from HeNe laser is implemented.

2.1.2 Traceability

For the old definition, there is only one bar exists in Paris. So not everyone has access to it. Even for the new definition, it is inconvenient for people to take the complex laser source with them to do measurements. Hence various of rulers like vernier caliper and spiral micrometer are made calibrated on the standard to make it accessible to all the people in need of different accuracies. The tool calibrated based on the primary standard directly is called secondary standard. Next, the tool based on secondary standard is called third standard. This is like a pyramid with different levels from top to bottom. It could be seen that when level goes down, the accuracy is reduced. The link between a measurement tool and the primary standard is called traceability.

2.2 Optics

In this section necessary knowledge of optics to understand the working principle of a interferometer is introduced including properties of light, production of laser light and relevant optical elements used in the system.

2.2.1 Basic properties of light

Electromagnetic waves

Light is an electromagnetic wave that is described by the Maxwell equations [6].

An interferometer makes use of the wave properties of light. Light has a constant speed c of 299 792 458 $\mathrm{m\,s^{-1}}$ in vacuum governing the propagation speed of the wave. The length between two points that defines a period of oscillation is called the wavelength λ. The frequency f is the number of the oscillation periods passing the same point in one second. Frequency multiplied by wavelength defines the propagation speed c. As c is constant in a certain media, once one of them is defined the other can be derived. Frequency can be expressed by angular velocity ω as well. Assuming a sinusoidal wave has a frequency of 1 Hz, it means the phase angle it passes in one second is 2π. So the relation between the frequency and angular velocity is $\omega = 2\pi \cdot f$. To sum up, light has the following wave equation when it is observed at a fixed point on the wave:

$$\sin(\omega \cdot t). \tag{2.1}$$

The value between brackets is the phase, which defines the position of a point on the wave. In this equation the wave is only defined by time. An extra value ϕ can be introduced to set the starting point of a wave.

Polarization

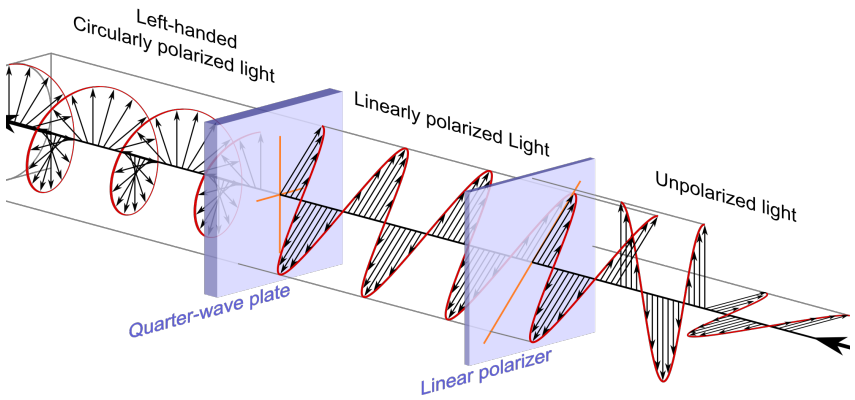

Figure 2.1: The incident beam coming from right is unpolarized. After passing through the linear polarizer, the light becomes linearly polarized. The quarter wave plate makes the light circularly polarized. (A special coherent beam of light is used to proved a clear demonstration.)

Electric field and magnetic field of light are perpendicular to each other, which can be used to define a surface. The propagating direction of light is perpendicular to this surface. For a beam of light propagating in the same direction, there can be many possible directions for its electric field confined in the perpendicular surface. If the directions are random like sunlight, it is called an unpolarized

light as shown in Figure 2.1. When electric fields of all light in this beam have the same direction and the direction is a fixed line in the perpendicular surface, the light is called linearly polarized light. When the unified direction is rotating in the perpendicular surface along the propagating direction, the light is called circular polarized light.

2.2.2 Lasers

The laser has been successfully adopted in many fields in modern life. There are laser printers, laser cutters, laser projectors and so on. In this thesis, a laser is used as a measurement tool because of its excellent properties.

Properties

Laser light is an electromagnetic wave with high coherence, diffraction limited collimation, high powers and wide tunable range. S. Ezekiel [7] explained all the properties in a clear non-mathematical way.

High coherence is the key property for laser's application in interferometry. If an ideal perfect sinusoidal wave is observed in the frequency domain, it will be a single line with zero width. In reality the wave can not be infinity coherent, so there is always a width to it which corresponds to deviation of frequency. For a laser beam, this deviation in frequency is limited as shown in figure 2.2. Besides, it has high spatial coherence, which means all the waves have their crest and valley at the same point in time. These high coherence relations are related to the way how laser light is produced. They make sure that all rays of light in the beam have the same temporal signature on the sin wave so that the interference is clearly observable and can be detected easily.

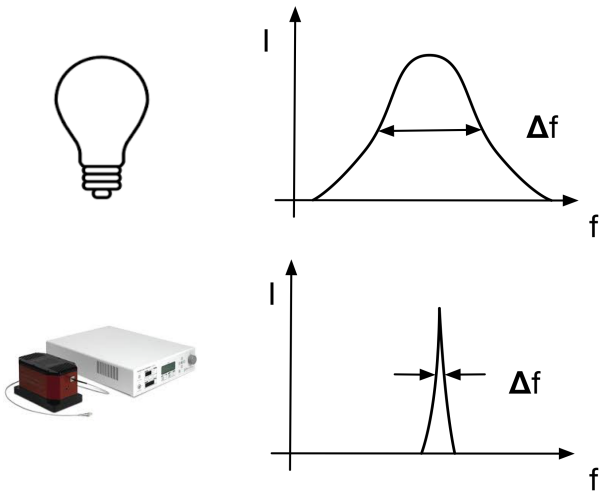

Figure 2.2: Comparison between the frequency of light from bulb and high coherent laser source. Frequencies of light coming from both sources are not identical. If it is analyzed with a spectrum analyzer the deviation from the main frequency can be observable. This graph shows that the frequency of a laser is much more uniform.

Diffraction limited collimation means that if the laser traveling in air is observed, its profile can be represented by two boundary rays of almost independent parallel lines of propagation allowing a very small angle in between which is defined by a basic physical principle:

$$\theta = \frac{\lambda}{D} \tag{2.2}$$

where D is the diameter of the laser beam and λ is the wavelength which is about hundreds of nanometers for visible light. This results in a very small value that is negligible in most cases for macroscopic beam diameter. This property enables laser to travel a long distance without much divergence in spatial aspects. Combining this property and the high coherence, the behavior of laser can be described at any position at any time.

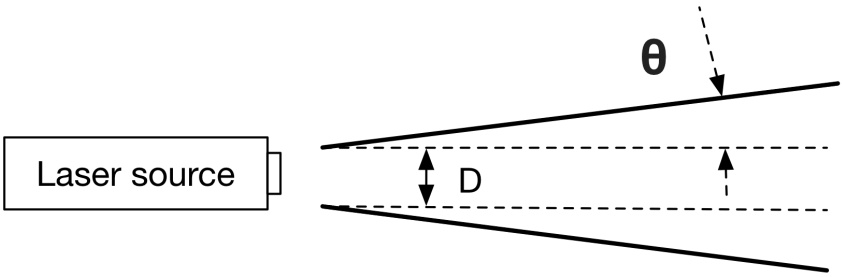

Figure 2.3: Profile of laser beam after comes out from the source.

In terms of optical power, a continuous wave laser can produce light from milliwatts to megawatts, which enables the laser to be used in material processing, fusion and military applications. Under the condition of similar frequency fluctuation levels, a laser with stronger intensity is preferred for a higher signal to noise ration. The wide tuning range is related to how the laser light is produced. Visible lasers have a wavelength from ultraviolet to far-infrared. For each kind of laser, the tuning range can be small or broad.

Production of laser light

Production of laser light is related to energy states of electrons in atoms. Figure 2.4a shows two energy states of electrons in atoms indicated as level 1 and level 2. When a photon with the correct energy interacts with the atoms, the electron on level 1 will absorb the photon and change to energy state level 2. This process is called stimulated absorption. Figure 2.4b shows the life time of the excited electron is finite. It will go back to level 1 spontaneously, the energy loss during this process is expressed by emitting a photon which has an arbitrary direction. This process is called spontaneous emission. Photons emitted by spontaneous emission will stimulate the decay of other excited electrons to level 1. This stimulation speeds up the decay process and is called stimulated emission. Both absorption and emission processes have a certain preferred frequency f related to the energy difference between the two energy states expressed by:

$$f = \frac{E_1 - E_2}{h} \tag{2.3}$$

where E_1 and E_2represent the energy levels and h is the Planck constant. This is one of the reasons why lasers have a low deviation in frequency. If the emission is more significant than absorption, there will be light coming out. It is possible when the population of electrons on level 2 is larger than the population of electrons on level 1. This phenomena is called population inversion which depends on the gain of the laser. Vice versa, if the absorption is more significant than emission , the incident beam will be absorbed. If the two processes are equal, the external light will pass through without attenuation, which means the material is transparent.

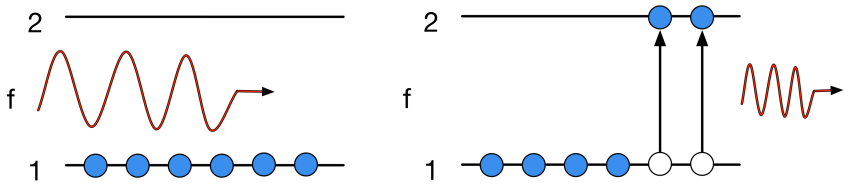

(a) Absorption. When a photon with the correct energy interacts with the atoms, electron on level 1 will absorb the photon and changes to energy state level 2.

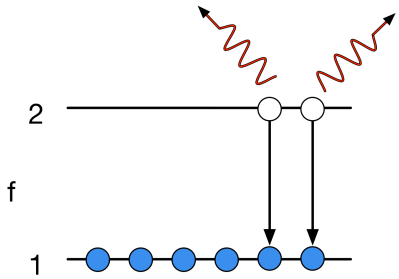

(b) Emission. Caused by spontaneous decay of the excited electron (spontaneous emission). Stimulated energy level change from interacting photons will lead to the decay of electrons at the upper energy level as well (stimulated emission).

Figure 2.4: Two kinds of interactions between photons and atoms.

The electron system shown above has two energy levels called a two level system. However it is impossible to have a population inversion as at last the two levels can be balanced. the population inversion, as electrons always prefer the low energy level. To solve this problem the following three level system is introduced.

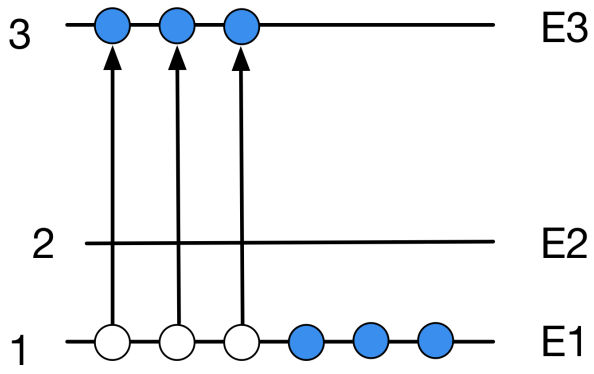

Figure 2.5: Three level system.

First, the electron is pumped up from level 1 to level 3. Because level 2 is empty, as long as there are electrons on level 3 the population of electrons on level 3 is larger than level 2. Using this trick, the population inversion is easy to achieve. In the examples above, absorption energy comes from photons. There are all kinds of other different ways of triggering this process. For example optical pump, atom collision and electron collision.

Take as example the He-Ne (Helium-Neon) laser (see Figure 2.6). It combines the electron pump and atom pump. First the absorption is between external electron and Helium atoms. Part of the energy from the external electron gets absorbed by the helium electron. The excited helium electron goes to energy level m. Collision between the helium atom with excited electron and the Ne atom transfers the energy to the Ne atom. When the Ne electron falls back to a lower energy level, a

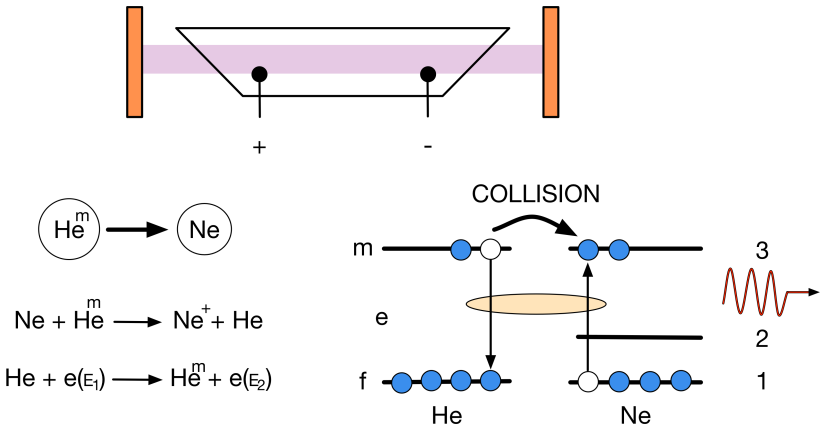

Figure 2.6: Concept of He-Ne laser source [7]

photon is emitted. Spontaneously emitted photons are traveling in all directions. To achieve a high spatial coherence and minimize deviation in frequency, two parallel mirrors are introduced to select light in the preferred direction and frequency, as a consequence spatial and temporal coherence is guaranteed. As shown in figure 2.7, emitted photons get reflected back and forward between the two mirrors. The electromagnetic waves can be compared as a stationary wave oscillating on a string between two nodes. In this configuration only the waves that have wavelength matches the string length can exist, which is expressed as

$$\lambda = \frac{2L}{n} \tag{2.4}$$

Where λ is the wavelength of the laser, L is the length between the two mirrors and n is an integer determing the number of periods in the string.

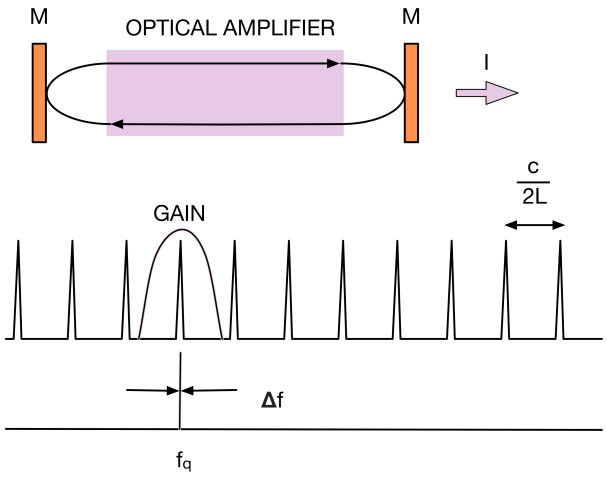

Figure 2.7: Frequency selection process during laser light production. First, laser light is selected by the two-mirror defining cavity to have a set of frequencies with difference of $\frac{c}{2L}$ between each other. Then the gain of the population inversion selects one of the frequencies as the final dominant frequency for the laser beam.

Light has a propagation speed of c in vacuum. If this is transferred into the frequency domain, the potential frequencies will be $f = \frac{n \cdot c}{2L}$. This way, a series of frequencies with difference of $\frac{c}{2L}$ between each other are selected. As n is an arbitrary integer, the wavelength is not unique yet. Since the amplifier or gain medium has a preferred frequency, the wavelength permitted in the tube is narrowed down. Beams not perpendicular to the parallel mirrors will be absorbed by the walls. Only the mode

matching the optical cavity will be amplified. The selected mode is determined by the lowest loss rate of the cavity in combination with the highest gain of the medium. If one of the mirrors is not perfectly reflective, a part of beam will pass and laser can be observed outside the cavity.

2.2.3 Basic optical elements

In the interferometer many optical elements are used in order to guide the laser beam in the desired path. Their function and principle are discussed as follow.

Optical fiber

As laser light propagates in a single direction, laser guides such as fibers form convenient tools to deliver light to a desired location. Normally a fiber consists of three layers from inside to outside: the core, the cladding and the jacket. The core is the inner most material that the light beam travels through. Cladding is the layer outside of the core. It has a different refractive index from the core resulting in total internal reflection happens and coupling the light to the core. For large core diameter fibers, the laser beam can be depicted as zigzagging through the fiber. The jacket is the outer layer that protects the fiber from external influences. Normally, the diameter of the core is of the level of a few micrometers. The outer diameter of the jacket is of the level of a millimeter.

Fibers can be subdivided into single mode fibers and multi mode fibers corresponding to how many different transverse modes of laser are allowed. The basic transverse mode is the TEM_{00} mode, which lowest order has a Gaussian profile in the center. In single mode fibers, the core is very small so that only the mode in the center can travel through. In multi mode fibers, the core diameter is larger, so other modes besides the TEM_{00} order mode can travel through the fiber as well.

Wave plate

A wave plate is an optical elements that can alter the polarization of a laser beam. Two types of wave plates are widely used: half wave plates and quarter wave plates. The half wave plate changes the polarization of a linear polarized beam by 90 ° when proper aligned. Quarter wave plate can convert a linearly polarized wave into a circularly polarized beam and vice versa. If two quarter wave plates are placed in a row and aligned correctly, the polarization of the beam can be shifted by 90 ° which is equivalent to the function of a half wave plate. Misalignment of the wave plate will influence the purity of the polarization resulting a mix when the interference signal is being processed.

Beamsplitter

A beamsplitter can split a beam into two beams with preferred light distribution. For example, a 50/50 beamsplitter can split a beam into two beams with half of it transmitted in the original direction while the other half is reflected by an angle of 90°. This can be realized by a half mirror coating. As the main function of a beamsplitter is to guide the beam into the desired path, misalignment may cause asymmetric in the system or decrease the light intensity received by the photo detector.

Polarized beamsplitter

The polarized beamsplitter works almost the same as the non-polarized beamsplitter but the split is based on a preferred polarization distribution. For example, only the beam with vertical polarization

could pass in the original direction while the beam with horizontal polarization will be reflected by 90°. Besides the geometrical influence, misalignment of the polarized beamsplitter will result in an undesired polarization, which will cause beam mix in the end.

Retro reflector

Basically a retro reflector works as a mirror. However, additionally, it is designed to reflect any beam back parallel to the original incident beam.

Collimator / Fiber coupler

A collimator is a part consisting of one or a set of lenses to focus the laser beam to a fiber, or to collect the diverging radiation exiting from a fiber to form a single parallel profile.

2.3 Interferometer

2.3.1 Interference of laser

An interferometer makes use of the wave property of light. When two coherent beams with similar frequency and same polarization overlap, interference can happen. If the two beams are in phase then constructive interference happens, the intensity will be 4 times brighter as that of a single beam. If the two beams are out of phase, then they will cancel each other and the interfered signal will have zero intensity. This is called destructive interference. The basic construction of an interferometer consists of two beams including one reference beam and one measurement beam. The reference beam is the one kept stationary all the time, while the measurement beam is the one that can be modified by the measured target. When the target generates a displacement, the interference between the measurement beam and the reference beam will alternate between constructive interference and destructive interference. By counting this alternation and multiplying with the wavelength, the displacement can be derived.

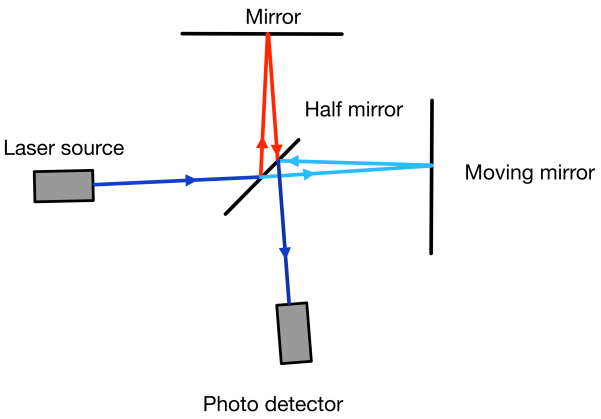

Figure 2.8: Simplified concept of Michelson Interferometer. The angle between incident and reflected beams is exaggerated to distinguish them. An actual interferometer can be more complex. For example, additional polarization sensitive optic elements are required to guide the light path in the preferred direction.

The most famous interferometer is the Michelson Interferometer. A simplified concept is shown in Figure 2.8. The function of it is to measure the displacement of the moving mirror. The laser beam comes from the laser source (dark blue) is split into two perpendicular beams by a half mirror. Each of the beams gets reflected by a mirror. The red beam with stationary mirror is the reference branch and the blue one with the mirror attached to a movable target is the measurement beam. These reflected beams get combined at the half mirror where interference happens. This interference signal (dark blue) is detected by the photo detector. Eventually, the signal is processed to get the displacement of the mirror.

2.3.2 Homodyne and heterodyne interferometer

As the interferometer discussed in 2.3.1 uses the same frequency for both the reference and measurement beam, it is called the homodyne interferometer. Besides, the interferometer can only measure the displacement of one mirror. When a block of material is the measurement object, only the surface attached to the mirror can be detected. This is called the single sided interferometer.

An example of a heterodyne double sided interferometer is shown as below.

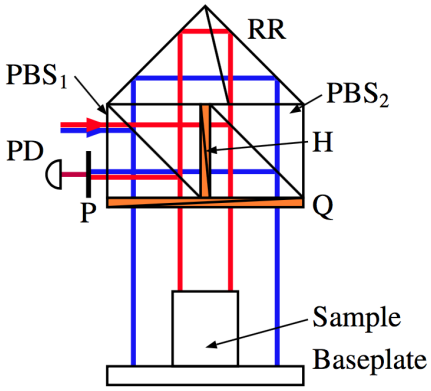

Figure 2.9: Example of a heterodyne interferometer developed by Okaji and Imai [8].
[1]

In Figure 2.9, a single sided heterodyne interferometer is used to measure the thermal expansion coefficient of the sample. The red beam detects the top surface of a sample. As the expansion needs to be calculated from the displacements between two points, the interferometer uses the reference beam to target the base where the sample resides on. The two beams coming out of the source have slightly different frequencies and orthogonal polarizations. The red beam has the polarization that could pass through PBS_1 (Polarizing beamsplitter) directly for the first time. Then it goes through a half wave plate H, which changes its polarization by 90°. When it passes through the second polarized beamsplitter PBS_2, it will be reflected to the sample. The mirror surface on the sample will reflect it. During this process the beam passes through the quarter wave plate Q twice, which changes its polarization by another 90°. This enables the beam to pass through PBS_2. Afterwards, the beam is reflected by a retro reflector (RR), goes through PBS_1 and is reflected by the mirror attached to the sample surface. As it passes through Q again, the change of polarization makes sure the beam is reflected by PBS_1 and gets detected by photo detector PD. As the blue beam has a different polarization, it will travel in opposite order through the beamsplitter. But in the end the two beams are combined and interfere at the photo detector.

Hetrodyne measurements have the advantage that the detected interference signal is not sensitive to the fluctuation in intensity of the laser source, which is a problem for homodyne interferometers. And hetrodyne signal will have a better result in terms of pink noise.

2.3.3 Quantitative model for interference

After solving the Maxwell's equations, the detectable signal at a fixed point can be expressed as

$$\vec{E_x}(t) = E_x cos(\omega t + \phi)\vec{x} \tag{2.5}$$

where $\vec{x}$ indicates the oscillating direction, $\vec{E_x}(t)$ is the electric field in x direction, E_x is the magnitude, ω is the angular frequency and ϕ is the phase offset. For an interferometer there will be two waves $\vec{E_m}$ and $\vec{E_r}$, where m refers to the measurement beam and r refers to the reference beam. At a specific point in space, they are expressed as:

$$\vec{E_m}(t) = E_m cos(\omega_m t + \phi_m)\vec{m} \tag{2.6}$$

$$\vec{E_r}(t) = E_r cos(\omega_r t + \phi_r)\vec{r}. \tag{2.7}$$

In case of interference these two waves will be added together:

$$\vec{E_{int}}(t) = \vec{E_m}(t) + \vec{E_r}(t). \tag{2.8}$$

The photo detector will not sense the electric field directly, instead it will detect the irradiance which is also referred as the intensity of the laser beam in the unit of power. The relation between irradiance and electric field is given by

$$I \propto \frac{c\epsilon}{\eta} /\vec{E}/^2 \tag{2.9}$$

where c is the speed of light, ϵ is electric permittivity, η is refractive index. The irradiance of the interference signal is derived by substituting 2.8 to 2.9:

$$I = \frac{c\epsilon}{\eta} /\vec{E_m} + \vec{E_r}/^2. \tag{2.10}$$

The square of the absolute value of a vector is equivalent to taking the dot product with its complex conjugate

$$I = \frac{c\epsilon}{\eta}(\vec{E_m} + \vec{E_r})^* \cdot (\vec{E_m} + \vec{E_r}), \tag{2.11}$$

as the multiplication of two vectors is equal to the multiplication of the magnitudes and the cosine of the angle between them, it is expressed as:

$$I = \frac{c\epsilon}{\eta}\left\langle /\vec{E_m}/^2 + /\vec{E_r}/^2 + 2E_m E_r cos(\alpha) \right\rangle. \tag{2.12}$$

Making use of 2.9, equation 2.12 is equivalent to

$$I = I_m + I_r + \frac{c\epsilon}{\eta} 2E_m E_r cos(\alpha). \tag{2.13}$$

Substitute 2.6 and 2.7 into 2.13:

$$I = I_m + I_r + \frac{c\epsilon}{\eta}\left\langle 2E_m E_r cos(\omega_m t + \phi_m) cos(\omega_r t + \phi_r) cos(\alpha) \right\rangle. \tag{2.14}$$

In this case, α represents the angle between the reference beam and the measurement beam, which is the difference in polarization. This shows that for laser beams with orthogonal polarization interference will not happen, as this term becomes zero only leave two DC terms. For interferometers the measurement and reference beams have the same polarization and $cos(\alpha)$ equals to 1.

According to trigonometric identity:

$$2cosAcosB = cos(A+B) + cos(A-B), \tag{2.15}$$

equation 2.14 equals

$$I = I_m + I_r + \frac{c\epsilon}{\eta}\left\langle 2E_mE_r cos\big[(\omega_m+\omega_r)t+(\phi_r+\phi_m)\big] + 2E_mE_r cos\big[(\omega_m-\omega_r)t+(\phi_r-\phi_m)\big]\right\rangle. \quad (2.16)$$

As the frequency of light is very high, it can not be detected by the photo detector, not to mention the twice of that frequency. So the first temporal term averages out meaning only the slow oscillating term will contribute. Making use of equation 2.9 again, the interference signal is simplified to

$$I = I_m + I_r + 2\sqrt{I_mI_r}cos\big[(\omega_m-\omega_r)t+(\phi_r-\phi_m)\big] \quad (2.17)$$

If the two beams have the same intensity $I_m = I_r$ the following result is derived:

$$I = 2I + 2Icos\big[(\omega_m-\omega_r)t+(\phi_r-\phi_m)\big] \quad (2.18)$$

Homodyne interferometer

For homodyne interferometer the two beams have the same frequency meaning that $\omega_m = \omega_r$. The interference signal becomes

$$I = 2I + 2Icos((\phi_r-\phi_m)). \quad (2.19)$$

It could be verified that when constructive interference happens, the two beams are completely the same in space and time. And the phase difference will be zero. The interference signal ends up to be $4I$. If the two beams are out of phase, which gives a phase difference of 90°, the interference signal is zero. Hence when the traveled distance between the two lasers move relative to each other in space, the relative phase will change and the interference signal will alternate between zero and $4I$ following a cosine function. Knowing the relation between phase angle and wavelength, the relative motion can be derived backwards. However, as the phase is calculated from an irradiance measurement, the key to achieve high precision measurements with homodyne interferometer is to keep the intensity as stable as possible, which is quite a challenge.

Heterodyne interferometer

For heterodyne interferometers the measurement beam and the reference beam originate from the same laser source. But an additional frequency Δf is generated for one of the beams resulting a difference in frequency. The interference signal for heterodyne interferometers becomes:

$$I = 2I + 2Icos(\Delta\omega t + (\phi_r-\phi_m)) \quad (2.20)$$

Now the phase difference is not the only factor influencing the shape of the cosine wave. It becomes a wave mainly oscillating at frequency Δf.

2.4 Picodrift interferometer

The picodrift interferometer is a double sided heterodyne interferometer. As shown in Figure 1.1 the interferometer is made of three parts: laser preparation system, interferometer and the data processing system. In this section each of them will be introduced.

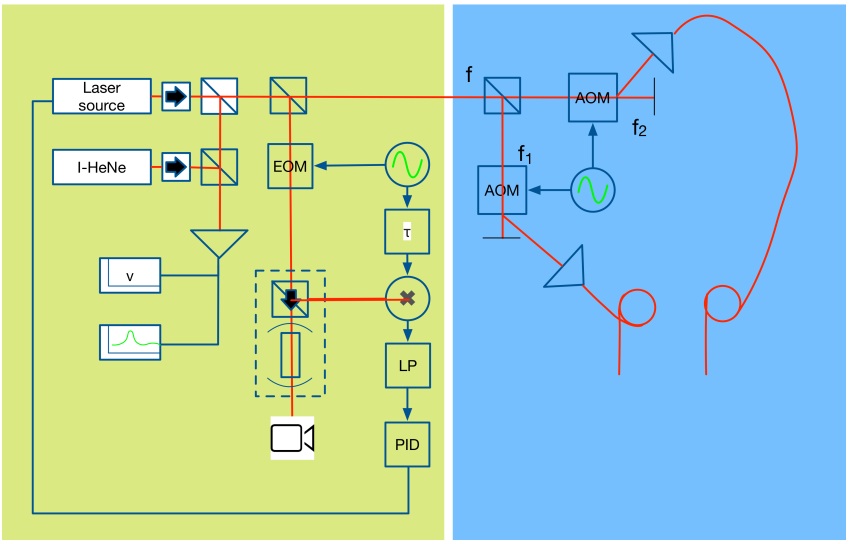

Figure 2.10: Laser preparation system. The green part is the laser source with control loop to stabilize the laser frequency. The blue part is where the beam is separated into two different branches with an offset in frequency using two AOM (Acousto-optic modulator). [2]

2.4.1 Laser preparation

As expressed by Equation 2.20, the heterodyne interference signal is sensitive to the laser difference frequency. If the laser frequency varies during the measurement, the phase detected will change as well which will influence the accuracy of the result when translated into displacement. Additionally, even though the heterodyne interferometer is not sensitive to intensity variations, if the beam becomes too weak after passing all kinds of optical elements, the obtained noise to signal ratio will be high and reduces the quality of the result. Therefore a laser source with sufficient power is used in combination with an additional control loop, which applied the PDH method to stabilize laser frequency. After stabilization, the laser beam is split into two beams with a small offset in frequency. Afterwards, the polarization should be selected and cleaned before the beams enter the interferometer as the interferometer expects a selected polarization state as input. An overview of the laser preparation setup is shown in Figure 2.10.

Fabry Pérot cavity for frequency selection

The Fabry-Pérot cavity is introduced to select the laser frequency. It has a similar resonator structure [9] as the cavity described in 2.2.2 used to build up the laser resonator. It consists of two mirrors with a certain distance in between to allow the laser beams to resonate. As defined by the distance between the two mirrors, only the laser with a specific frequency can be transmitted. By sensing the transmitted laser signal using a photo detector after the cavity, the deviation from the cavity frequency can be estimated. This deviation is used to stabilize the laser frequency using a feedback loop control. The quality of stabilization depends on the dimensional stability of the distance between the mirrors. However two problems will be caused by simply detecting the transmitted intensity. The laser light coming from the laser source has not only frequency instability but also has instability in intensity. This means the change in intensity will cause errors during the feedback process. This can be solved by measuring the reflected beam on the other side of the cavity. At resonance frequency, the reflected beam has zero intensity, which is independent from the incident laser intensity. The second problem is that the shape of the reflected beam intensity response in the frequency domain around the resonance frequency is symmetrical, which causes the control system to have to try two direc-

tions to make the corresponding change. To overcome this problems, PDH (Pound–Drever–Hall) laser frequency stabilization is introduced.

Pound–Drever–Hall laser frequency stabilization

As shown in Figure 2.10, the Pound–Drever–Hall laser frequency stabilization method [10] [11] is used in combination with the Fabry Pérot cavity. It consists of an EOM (Electrical optical modulator) which stands for electrical optical modulator, mixer, low pass filter and a control system. The modulation generated from the oscillator gets mixed with the laser frequency in the EOM. So the laser traveling into the cavity has a carrier frequency which is the actual laser frequency together with two side frequencies because of the mixing. Then this signal is detected by the photo detector. The frequency information is contained in the amplitude of the signal with the frequency from the mixer. The signal from the oscillator is used again to separate the mixed signal from the reflected laser. A low pass filter LP is used to eliminate the main frequency from the laser. The remaining signal is called error signal which is an unsymmetrical signal. It can be used to determine in which direction the frequency should be adjusted. A PID controller is used to control the current of the laser source in order to provide a frequency stabilized laser to the interferometer.

2.4.2 Picodrift interferometer

A picodrift interferometer with low nonlinear error and high symmetrical design was developed by J.D. Ellis. It has a double sided interferometer which measures the dimensional change of the sample using the laser beam reflecting from mirrors on two sides of the sample. At the same time, another interferometer works as refractometer, which is built highly similar to the measurement interferometer. But instead of measuring the sample, the laser beam travels through a vacuum tube. By sensing the variation between the refractometer's measurement and reference beam, the refractive index can be determined over the length of the vacuum tube. This derived value is used to compensated the error of the interferometer caused by temperature and pressure influenced refractive index fluctuation. Figure 2.11 depicts the working principle and how the beams propagate through the interferometer.

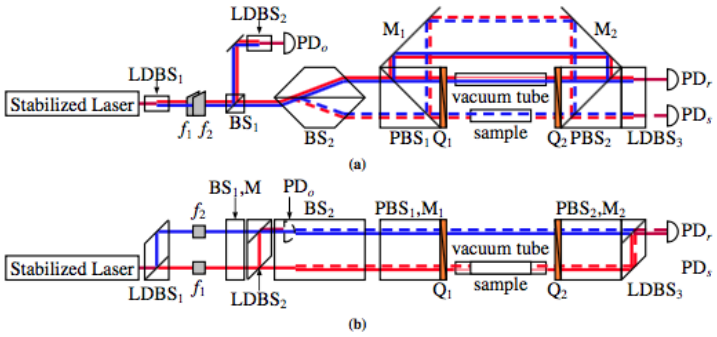

Figure 2.11: Top view (a) and front view (b) of Picodrift interferometer [1].

In Figure 2.11, the frequency stabilized laser beam comes from the left side. It's separated by the $LDBS_1$ (lateral displacement beamsplitter) into two beams, one at the top and one at the bottom. These two beams travel through two acoustic optic modulators to have an offset frequency f_1 and f_2. Then a beam-splitter BS_1 is used to take part of the beams to a photo detector to do a reference measurement. After the beamsplitter, the other part of the beams go through BS_2 where they are separated into four beams. The blue line on top corresponds to the reference beam with frequency f_2, while the red color at the bottom corresponds with the measurement beam with frequency f_1.

The dashed line is the interferometer which measures the sample directly and the solid line is the refractometer.

For these four laser beams, there are two kinds of light paths: First, the measurement beam sensing both surfaces of the sample. Second, the reference beam for the interferometer and the two beams for the refractometer. The polarization of the laser has been selected to be vertical with respect to the base before $LDBS_1$. It means all beams have the same vertical polarization before polarized beam-splitter 1. For the beam sensing two surfaces of the sample which is indicated by the red dashed line, it first propagates through PBS1 which transmits the vertically polarized beam. The quarter wave plate Q_1 changes the laser to be circularly polarized. The mirror attached to the surface of the sample reflects the beam back to Q_1 which changes the circularly polarized beam to a linearly polarized beam again, but with horizontal polarization with respect to the base. Now, when this horizontal polarized beam travels to the polarized beam splitter for the second time it will be reflected by 90° and reflected by mirror M_1 then mirror M_2. For the same reason it will be reflected by the mirror attached to the other side of the sample and travels through the PBS_2, reflected by the lateral beam splitter $LDBS_3$, interferes with its reference beam and gets received by the photo detector PD_r. For the other three beams, after going through the quarter wave plate, they will pass through air or the vacuum tube and directly come to the quarter wave plate Q_2 and change their polarization to horizontal direction, before being reflected by PBS_2 by 90°. Afterwards they will be reflected by M_2, M_1, PBS_1, pass through Q_1, air or vacuum tube, come to Q_2 which will change their polarization back to vertically polarized and pass through PBS_2, ultimately being received by the photo-detector.

After the photo detector, the electrical signal is analyzed by a lock-in phase detection to acquire the phase information. Then this phase information is translated to displacement.

2.4.3 Improved picodrift interferometer

The improved interferometer increases the number of interferometer channels from two to four which can be divided into two sets of interferometers containing a measurement interferometer and a refractometer. One set of them is covered in the vacuum environment which provides precise displacement or dimensional measurement with variable pressure control. While the other set is partially exposed to the atmosphere allowing easy access to do measurement in open environment. Additionally, temperature control is implemented by a breadboard underneath connected to a circulator to vary the temperature. The basic laser path is similar to the old design. The improvement is implemented by using two beamsplitters, which splits the incident beam into 4 parallel beams. In Figure 2.12 the gray box is the vacuum chamber where most of the interferometer optical parts are located. The small white rectangle around S_1 indicates the are open to atmosphere, where atmospheric measurement can be taken.

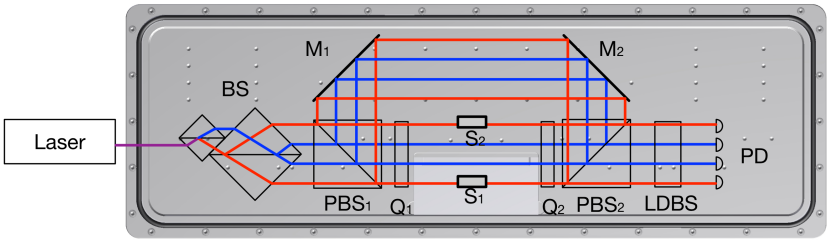

Figure 2.12: Improved picodrift interferometer. Red line indicates measurement interferometer, while blue line is the refractometer.

As shown in Figure 2.12, all optical elements are located in a customized vacuum chamber. The sealed envirounment will provide a very stable measurement condition in terms of pressure. To evac-

uate the air from the chamber, it is connected to a turbo pump and an ion pump. The chamber sits on a breadboard which is temperature controlled. The entire setup is located on a stable damping table with low vibration.

The advantages of the new upgraded picodrift interferometer are listed as below:

1. The stabilized strong laser source together with the in house frequency standard creates a reliable laser with low uncertainty.
2. The high symmetrical design compensates most of the errors, which may be picked up during the light path.
3. The separated laser beams for the heterodyne interferometer largely removes the periodic error.
4. Parallel refractive index compensation minimize the influence of the change of temperature and pressure on the measurement result.
5. The controlled measurement environment can be used to do measurement at various environmental conditions.
6. The separated measurement space in atmosphere makes it easy to operate without influencing the alignment of the optic path.

Chapter 3

Implementation of the upgraded interferometer

This chapter describes the implementation of the upgraded interferometer based on the design shown in Figure 2.12. It covers the realization of the controlled environment in terms of pressure and temperature, design of mounting systems for different optical elements and the alignment of the optical path for the entire interferometer.

3.1 Environment control

The environment control mainly focuses on the realization of the vacuum system and the temperature regulation system. Both of them will help improve the stability of the refractive index and enable the simulation of different measurement conditions. Additionally, the stabilized temperature environment will minimize dimensional change due to thermal expansion.

3.1.1 Design objectives

As described by equation 2.20, the direct measured property of the interferometer is the intensity of the light available at the photo detector, which is related to the phase parameter. This intensity is translated into displacement in the post data processing. This conversion between phase and displacement is described as follow:

$$\phi = \frac{2\pi N \eta \Delta z f}{c} \tag{3.1}$$

where

N is the interferometer index ($N = 2$ for this picodrift interferometer)

η is the refractive index of the media where the light passes through

Δz is the displacement

f is the laser frequency

c is the speed of light.

In this equation, N and c are constants. The terms left are η, Δz and f. To have the phase truly reflecting the change of displacement, η and f need to be kept constant. For example, if the requirement

is to allow an uncertainty of 10 pm for a measurement range of 100 µm, which equals a fraction of $1/10^7$, this fraction needs to be applied as maximally allowed frequency and refractive index fluctuation. The laser used in the picodrift interferometer has a frequency of 4.7376×10^5 GHz (speed of light is 299 792 458 m / s, wavelength is 632.8 nm). And the refractive index in vacuum is 1. So the allowed variable range for the frequency should be below 47 MHz and the change of refractive index should be below 10^{-7}, The stabilization of the laser frequency has been discussed in 2.4, while the refractive index is influenced by temperature, pressure, humidity and air composition. For standard dry air, the refractive index can be described by the Edlén equation [12] and its improved version [13] [14]:

$$(\eta - 1)_{TP} = \frac{P(\eta - 1)_\lambda}{96095.43} \frac{1 + 10^{-8}(0.601 - 0.00972T)P}{1 + 0.003661T} \tag{3.2}$$

$$(\eta - 1)_\lambda \times 10^8 = 8342.54 + \frac{2406147}{130 - \lambda^2} + \frac{15998}{38.9 - \lambda^2} \tag{3.3}$$

where

P is the pressure of the air where the laser beam passes through (Pa)

T is the temperature of the environment (°C)

η_{TP} is the refractive index in dry air

η is the refractive index in the actual environment, $(\eta - 1)_\lambda$ is the refractive index as function of the wavelength

λ is the wavelength of the laser beam (µm).

For moist air with a partial pressure of f, the corresponding refractive index η_{TP} is calculated by:

$$\eta_{TPf} - \eta_{TP} = -f(3.7345 - 0.0401\lambda^2) \times 10^{-10} \tag{3.4}$$

where f is the partial pressure.

Taking the equation as an estimation for the vacuum situation, it can be derived that to achieve the uncertainty of 10 pm for a measurement range of 100 µm, the pressure variation should be controlled with stability better than 10^{-3} mbar, and the temperature stability should be better than 1 mK. Detailed relations can be found in appendix A.2.

3.1.2 Vacuum system

When the pressure drops below 1×10^{-3} mbar, the fluctuation of pressure is small, and will not play a significant role in the change of refractive index. However the starting pressure for the vibration-free ion pump is below 1×10^{-5} mbar. This sets the desired pressure for the vacuum system to be below 1×10^{-6} mbar which is on the UHV (ultra high vacuum) level. To realize this vacuum environment, two factors limiting the lowest pressure a system can reach have to be minimized: leakage and outgassing.

Overview of the vacuum system

As shown in Figure 3.1 a customized aluminum box is used to provide the vacuum environment for the optical elements. The box is closed with a large rectangular lid. Bolts and nuts are used all around to fasten the connections. The gaps between the box, lid and flanges are sealed by o-rings. There is an open compartment at the front surface of the box for measurements. At the two sides of the compartments, there are two small windows to allow the measurement beams to come out of

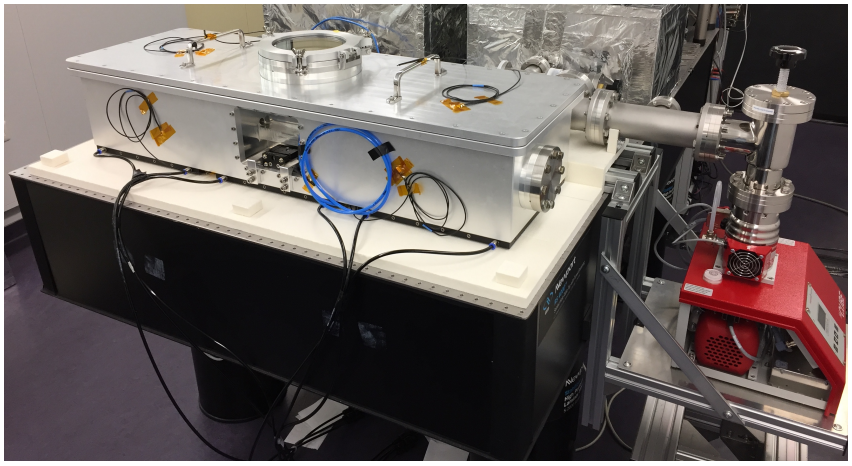

Figure 3.1: Configuration of the vacuum system.

the vacuum environment into atmosphere. Two other observation windows are incorporated in the box: one on top of the lid and the other one at the back of the box to have quick access into the box and for observation of the experiment. Feedthroughs of fibers and cables for sensors and actuators are realized by special flanges obtained either from the optics manufacturer or vacuum suppliers. A turbo pump integrated with a membrane pre-pump is used to provide initial pumping to get the pressure down to 10^{-5} mbar. From then on, the ion pump at the back of the box takes over to provide a vibration-free pumping.A schematic drawing of the vacuum system is shown in Figure 3.2.

Initially, the turbo pump was connected to the vacuum chamber via a flexible bellow to reduce the vibration from the pump transferred to the interferometer. However, during the test it was found that when the pump sucked the air out, the bellow would contract completely and all vibration damping abilities were lost. Additionally, the pump could be lifted up by the bellow, as a consequence all weight was exerted on the vacuum chamber, causing an asymmetry into the system. To resolve this problem, the bellow was replaced by a rigid connector. The pump was hang by a mounting station which was clamped to the isolation table. The vibration caused by the pump is transferred to the instrument. To make sure the pump is lifted by the feet underneath not by the tube to the vacuum chamber, alignment was done iteratively.

To evacuate the system, first all connections are closed by bolts and nuts. Especially, the top lid is fastened to the vacuum box in a symmetrical order. And each time only a small turn can be made to ensure the load is distributed evenly to all the bolts. The venting screw of the turbo pump should be fastened. Check and make sure the two valves are opened. Turn on the integrated turbo pump to start the pumping. When the pressure goes below 1×10^{-5} mbar, the ion pump can be turned on. As soon as the ion pump is working at full load, the valve close to the turbo pump can be closed. At this point, the turbo pump can be turned off to let the ion pump work alone without vibration. The function of angle valve 2 is to isolate the laser cavity from the rest of the system. Because the vacuum box may not always be required to be at ultra low vacuum depending on the required measurement conditions, but the laser cavity is always required to be evacuated in order to provide the most stable laser frequency.

Leakage

The sealing provided by o-rings can not be perfect. For a vacuum level of 10×10^{-7} mbar, the allowed leakage should be lower than 20 by 20 μm^2 [15]. As all metal parts are air tight, meaning no air can penetrate through the metal surface and get into system, the most likely leakage would happen between the metal and o-rings connections. It strongly depends on the quality of the o-ring, cleanli-

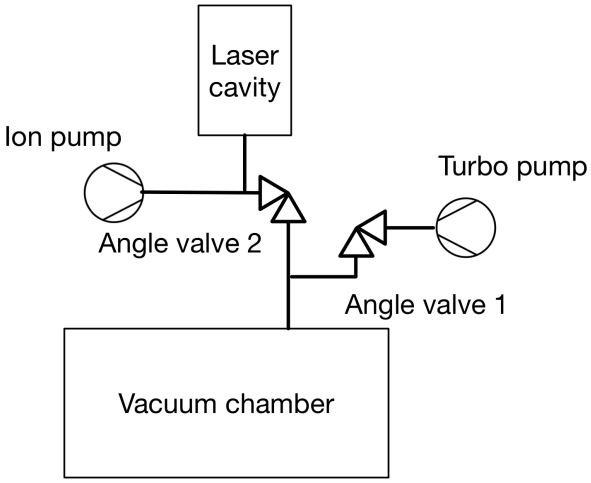

Figure 3.2: Schematic drawing of the vacuum system.

ness of the connection surface and the tightness of the mating. In A.3 a leak test was performed and discussed.

Out gassing

The other important factor that influences the final pressure is the surface of the used elements. Air can be trapped at the surface of materials for different reasons, for example, by grease left by humans' hands or manufacture processes, crusts of metal surface or just small spaces will not allow air to be evacuated. As the pressure goes down, this air may get evacuated eventually but it will be a very slow process, which makes it longer to evacuate the chamber to the desired pressure. This phenomenon is called outgassing. Different materials have different outgassing rates. Material like brass, which has a relatively high outgassing rate, should be avoided. To minimize the outgassing rate, surfaces of materials should be cleaned before they are used in vacuum. The cleaning procedure can be varied based on physical or chemical properties of the used materials.

Table 3.1: Parts used in vacuum and corresponding materials.

Parts	Materials
Bolts, Nuts, Washer	Stainless steel
Ring for optical window	Aluminum
Kinematic coupling mount	Invar (Nickel–Iron Alloy)
Optics	Various of glass

Metal parts have two major contamination sources [16]: oil (carbon in it can combine with other elements to contribute to out-gassing) and smut (an oxide layer on the metal surface that may trap gas).

In order to clean the oil, dish washer detergent or organic solvents (acetone) can be used. As they roughly have the same effect, both can be used to make sure the hydrocarbons like oil are removed.

The smut on different materials has different properties which requires different chemical product for treatment. For the smut on aluminum, Almeco 18 is a well acknowledged product. It is an alkaline detergent (ph 9.2 10g/L) to etch the surface. It can be followed by other detergent treatments, however the negative effect of that is unclear. The etching process should be well controlled, otherwise, it will cause dimensional change to the parts. The chemicals used for steel and aluminum are different.

As the pressure requirement is not extremely low in our application, this step could be skipped. The optics was not cleaned except for standard optics cleaning techniques making sure the optic quality was guaranteed.

In the paper of R.J. Reid [17] cleaning process based on different application conditions are discussed as well as some agents for the surface treatment. Based on the requirements of the interferometer and the availability of the cleaning equipments and chemical products, the following process is set to be applied on most of the elements (excluding the optical parts) that are present in the vacuum box.

1. Ultrasonic cleaning with mild dish wash detergent at 60°C for 20 min (If it takes too long, the aluminum may change color)
2. Demi water rinsing at room temperature for 2 min
3. Ultrasonic cleaning with acetone (flammable, boil point 56°C) at 20°C for 15 min
4. Wait for the evaporation of acetone
5. Bake (If applicable)

Wearing of gloves is mandatory for any operation within the vacuum box.

Pressure test

After the cleaning of parts and the leak test, the desired pressure was reached. By recording the pressure during evacuation, a pressure change as a function of time could be plotted as shown in Figure 3.3.

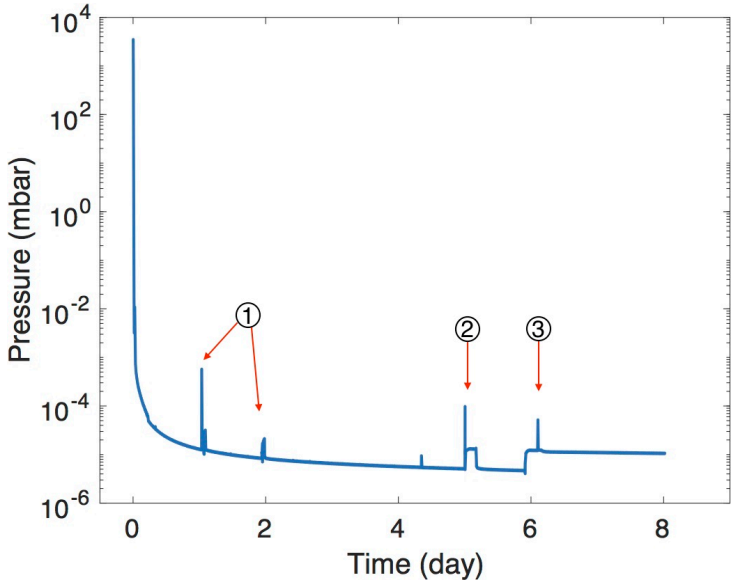

Figure 3.3: Pressure change during the evacuation. As the sensor is designed to work at high vacuum, the measured result above 1 bar is not accurate.

It can be observed that at the beginning of evacuation, the pressure dropped rapidly under the pumping of the membrane pump. At a pressure around 1×10^{-2} mbar, some peaks occurred. This could be the evacuation of some trapped air. The release of gas from the enclosed volumes increased the pressure suddenly indicated by label 1. However it was still under control of the pump. As the pressure went further down, it became difficult for the turbo pump to suck more air out, the decrease of the

pressure slowed down. After 5 days of pumping, the angle valve was opened, this action introduced some pressure change due to the higher pressure in the laser cavity indicated by label 2. After the pressure got in equilibrium again, the ion pump was turned on. This also introduced some distortion in the pressure indicated by label 3. Finally in day 6 the valve close to the turbo pump was closed leaving the ion pump work alone. The final pressure reached in the end is 6×10^{-7} mbar.

3.1.3 Temperature control

Temperature gradient always plays an important role in the field of precision instrumentation. For the picometer level interferometer, temperature changes have an influence on the refractive index, which is one of the major sources of error. Additionally, temperature change influences the dimension of materials used in the setup. All elements including laser source, beam splitters, stages and the vacuum box will change size because of thermal expansion. The interferometer is located in a clean room environment with a temperature control stabilities better than 0.1 K . Two methods are used to obtain an even better stability for the instruments as shown in Figure 3.4.

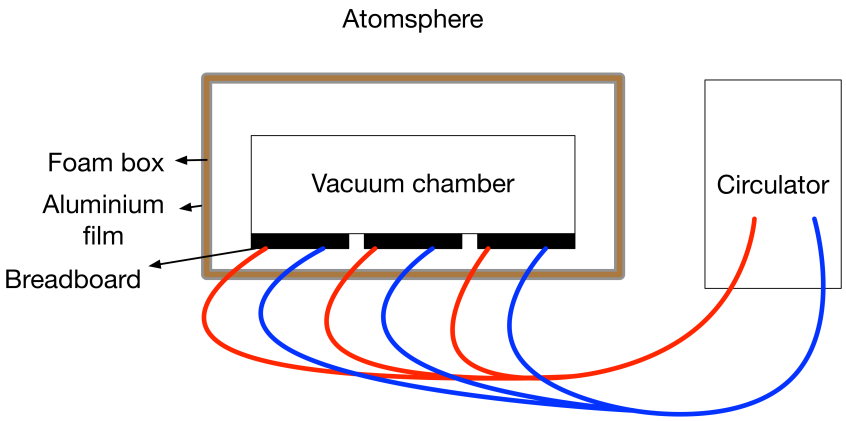

Figure 3.4: Simplified model of the temperature control system. The vacuum box is shielded with an aluminum coated foam box. The breadboards under the vacuum chamber are temperature controlled by an external circulator. The red line shows the output pipe of the circulator while the blue line is the input pipe for the circulator

.

Water circulator

A circulator is taken to drive water through the breadboards underneath the vacuum chamber. The circulator is able to control the temperature with a stability better than 0.01 °C. By keeping the temperature constant at the breadboard, it acts as a heat sink with a constant temperature. Thus the whole setup is less influenced by environment temperature fluctuation. Additionally, it enables the interferometer to do measurements under different temperatures to study the material behavior.

The circulator is put outside of the clean room to minimize vibration and the temperature influence because of its heating and refrigerator system. Two 6 m long tubes used for inflow and outflow are introduced to get the water into the breadboard in the lab room. As the room temperature is controlled at a certain degree, when the temperature set for the circulator is different from the room temperature there will be heat transfer between the tube and the environment. This needs to be noticed when a specific temperature is required as a measurement condition.

Foam box

The vacuum box is made of aluminum which is a good thermal conductor. This means the temperature change of environment can be easily transferred to the box. However, when the box needs to be heated up or cooled down, it will take a long time to reach an equilibrium point due to the many elements and materials involved. In lab conditions, because of the circulator underneath a significant temperature gradient can occur. During this process a huge amount of energy needs to be provided to reach the desired point. To solve this problem. A thermal shield is designed. There are three kinds of heat transfer: conduction, convection and radiation. A foam box fulfills the requirements to minimize each of them. A thick layer of foam with low thermal conductivity has a high resistance during conduction. The box shields the inside from air flow around the box, which minimizes convection. Additionally, a layer of aluminum foil can reduce radiative heat transfer. High thermal conductivity of the foil can make the temperature distribution around the box more uniform and reduce temperature gradients.

Temperature stability test

After the thermal system is implemented a stability test was performed. The temperature sensors are divided into two categories according to their different measurement target: air temperature sensors and material surface temperature sensors. Based on the measurement results shown in Figure 3.5, it can be seen that the temperature stability at surfaces is better than 1 mK in one hour and the stability in air is better than 2 mK in one hour.

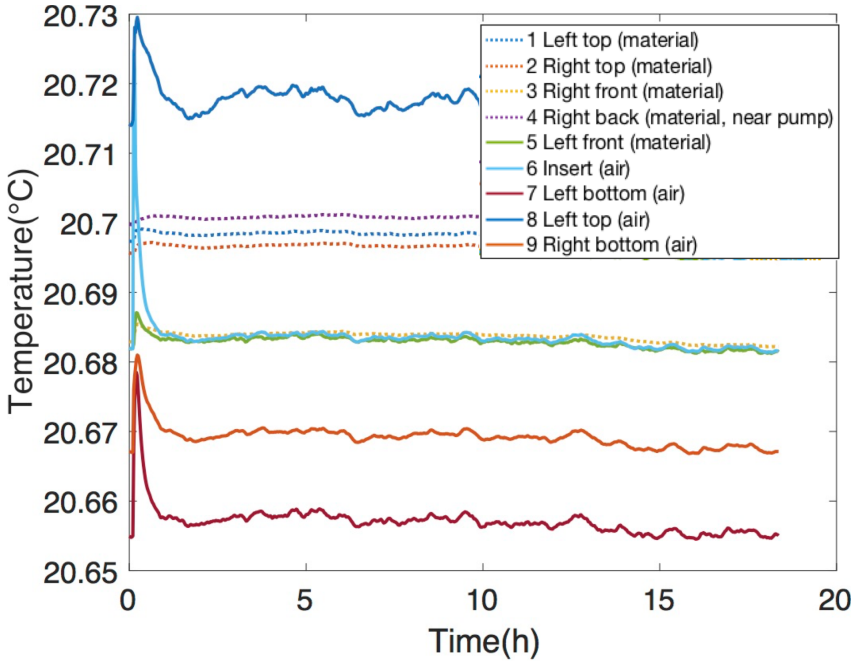

Figure 3.5: Temperature stability test. It can be seen that the temperature stability of each surface is better than 1 mK in one hour and the stability in air is better than 2 mK in one hour.

3.2 Mounting systems

For an optical system there are a lot of couplings between individual optical elements. To have a stable setup with optimal alignment, mounting mechanisms for the optical elements are very im-

portant. In this section, the mounting systems for collimators and beamsplitters are designed.

3.2.1 Mount for collimator

In comparison with the old two channel interferometer, the upgraded interferometer has four channels as shown in Figure 2.12. To achieve a highly symmetrical system, the four beams have to be parallel to each other with an equal space in between. The difficulty to collect all the four laser signals together at the same time is increased. In order to receive the interference signal after the beam combiner, 4 collimators are used in parallel. As shown in Figure 3.6, the original design was to mount all the 4 collimators on an invar disk without a specific alignment possibility for the individual collimator. For each collimator there is a corresponding screw to fix it after manual alignment. However in the actual alignment procedure, it was found that the screw and the invar disk together fully determined the position of a collimator which means that even after the optimal position is found, the collimator will still revert back to the initial position as soon as the screw is fastened. Additionally, the space between each of the collimators was not enough to allow individual optimization. When one of them was adjusted, the others will be influenced. So in the original design the alignment was never successfully realized.

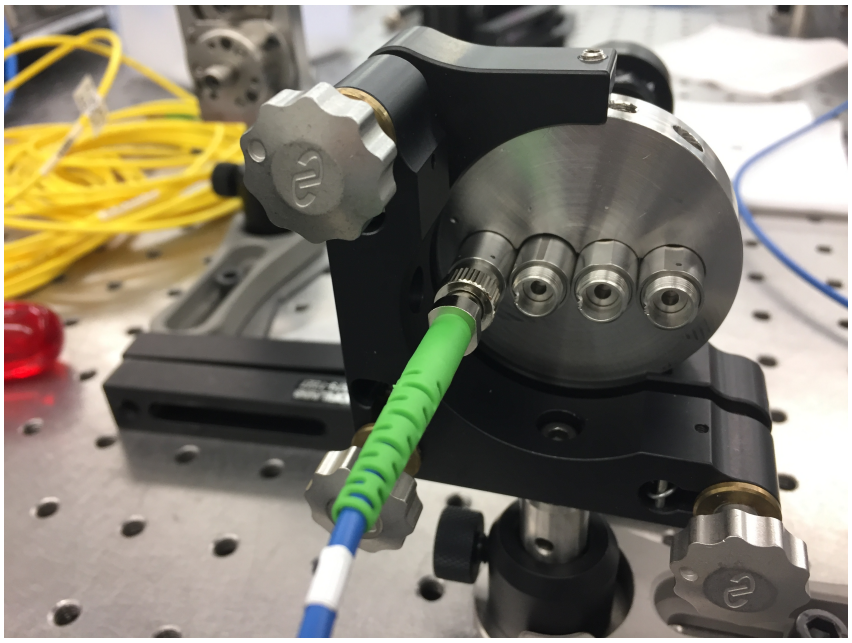

Figure 3.6: Back view of the old collimator mount. It was designed to adjust the position of the collimator individually and use the set screw to fix the position. However the screw together with the surface of the hole fully determine the position of the collimator. No matter what adjustment was made, it always reverted back to the initial position when the set screw is fastened.

As a consequence a new mount was designed to over come these problems.

Design constrains

- The outer diameter of the mount should be 2 inch to fit in a commercially available Newport mirror mount.
- Each collimator should be able to be adjusted individually with at least two degrees of freedom (rotation in x and rotation in y).

- The adjustment of one collimator should not influence the others.
- The collimators should be allowed to be rotated to align the orientation of polarization.
- The fixing mechanism should be strong enough to reduce sensitivity to vibration.
- Kinematic coupling is preferred in terms of precision measurement.

Design implementation

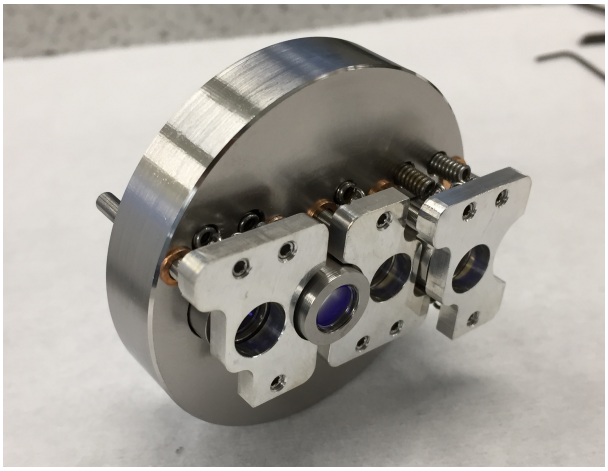

Figure 3.7: Newly designed collimator mount.

The new mount was designed as shown in Figure 3.7. It is made of four parts: the invar base, springs, fine adjusters and the fixation plates. Collimators are fixed on the fixation plates by a screw. Each fixation plate is pushed out with three fine adjusters. At the same time three springs connecting to the invar base pull the fixation plate to the invar base. Kinematic coupling is realized by the ball on top of the fine adjuster and the v groove on the fixation plate. As the springs will only provide the pull force without constraining it in any direction, the fixation plate is fully determined by the fine adjuster. After the test, this mounting device proved to fulfill the design requirements.

3.2.2 Mount for beamsplitter

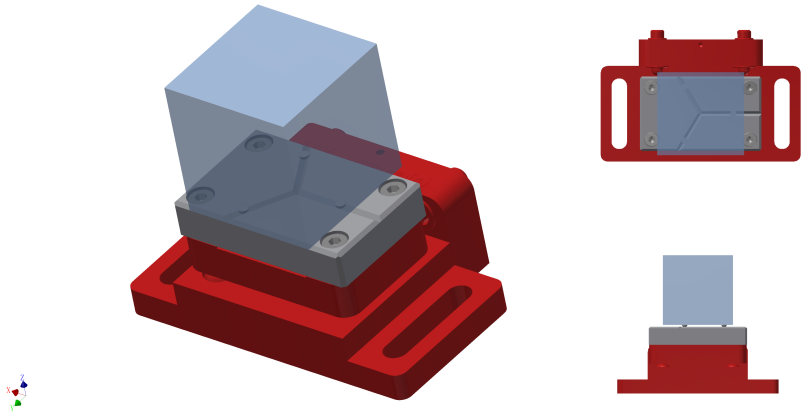

Figure 3.8: Kinematic coupling of optic elements realized by 3 balls and the v groove.

Inside the vacuum box, each optical element is adjusted by a Newport stage which has 4 degrees of freedom. There is a block of aluminum introduced between the stage and optics. It is used to realize the kinematic coupling in combination with the half balls glued under the optics as shown in Figure 3.8. By choosing different thicknesses for the blocks, the center of different optics can be aligned of the same height.

The contacting points form an equilateral triangle in order to make sure that when the dimension of the object changes due to thermal expansion, each edge of the triangle will have the same expansion, which keeps the center stationary. So that the relative position of each optic will not be influenced.

3.3 Alignment of the interferometer

The precision of the pico level interferometer relies on its highly symmetrical design, which will compensate the fluctuations coming from temperature change, pressure change, humidity change etc. This requires a lot of effort on the accurate alignment to achieve the designed optical path. At the meantime, the complex optical path increases the difficulty of alignment. To make the alignment process easier and get all the required optics glued, a pre-alignment was made outside of the clean vacuum chamber on a isolated optical table. After the pre-alignment was made and all optics glued, they were transferred into the vacuum chamber and aligned to be ready for operation.

3.3.1 Polarization

As the interferometer makes use of polarization for the path selection of the light beams, it is important to make sure the polarization is well defined for each part of the optical system. Otherwise, the interference signals end up at the receiver side will be mixed, causing noise during the data processing as signals can not be separated from each other. The general polarization is defined to be vertical, which means the incident laser beam should have a polarization vertically oriented before it enters the wave plate for the first time. All the fibers have a pin at the connection part while all collimators have a slot. When they are connected, the pin goes into the slot. This locks the relative rotation of the two components. The perfectly prepared polarization is transferred to the collimators through polarization-maintaining optical fibers. By rotating the collimator, the polarization can be modulated to the desired orientation. Rough alignment could be done by making sure that all slots of the collimators are pointing to the same angle. A polarized beamsplitter is employed to check the polarization of the laser comes out of a fiber. By minimizing or maximizing the light intensity, the desired polarization could be checked.

3.3.2 General alignment procedure

Alignment of the two collimators on the source side

The light delivery optics consist of an invar plate with two collimators positioned up and down as shown in Figure 3.9. Each collimator is vacuum compatible and installed in combination with a three degrees of freedom mirror mount. The function of it is to generate two parallel input laser beams with a separation of 20 mm in between.

Alignment procedure:

- Adjust the collimators to make sure the laser beam is collimated. The collimation is related to the focus of lenses. By adjusting the three screws together and observing the wave front diameter change through the laser path, optimized collimation could be reached.

- Rotate the collimator relative to the mirror mount, so that the laser beam exiting the collimator has a vertical polarization relative to the base. A polarized beam splitter can be used to obtain the optimal polarization correction. Adjustment can be done by angle rotation based on the read out of a photo detector behind the polarized beam splitter.
- Adjust the mirror mount so that the two beams are parallel to each other. Details can be found in appendix A.4.1. (The spatial position can be adjusted roughly at the beginning to ensure a good starting position, by using a ruler and take the frames of vacuum chamber as reference.)

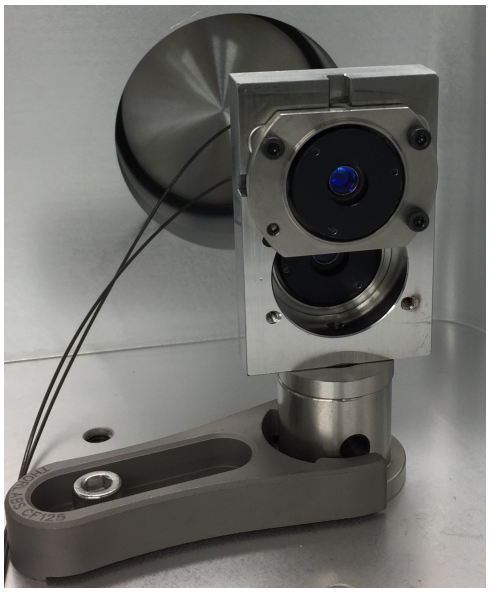

Figure 3.9: Two collimators mounted up and down. This part acts as the laser source for the inside of the interferometer.

Alignment of the four collimators on the receiving side

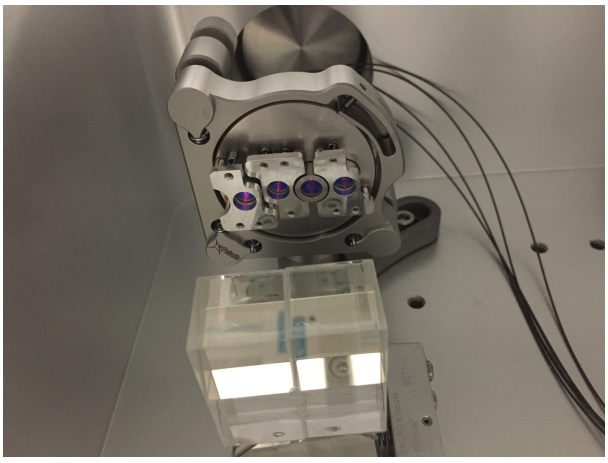

Figure 3.10: Four collimators on the receiving side. Through the fiber connected to these collimators, the interference signal is detected by photo detectors outside of the vacuum chamber.

The four collimator on the receiving side need to be aligned before the 4 way beam splitter. As it can be used to check the alignment result, this will help the alignment later. Because the photo detector is not sensitive to polarization, the collimator angle defining the coupled polarization is not very

important. As this is a customized part, the center of all four fiber couplers are already defined by the hole on the Ivar plate. The main task will be adjusting the tilt angle of the 4 collimators so that the 4 parallel laser beams can be successfully coupled into them. To make it easy to operate, it could be done the other way around. First fibers are used to connect the collimators with the laser source, so that there will be laser comes out from the collimator. A mirror is put in front of the collimators to provide the reflection. If all the four laser beams reflected by the mirror can be coupled back to the collimator, the parallelism of the four collimators is accomplished. An external setup is used to provide the laser source and detect the reflected beam which needs to be separated from the input beam. It has the following configuration:

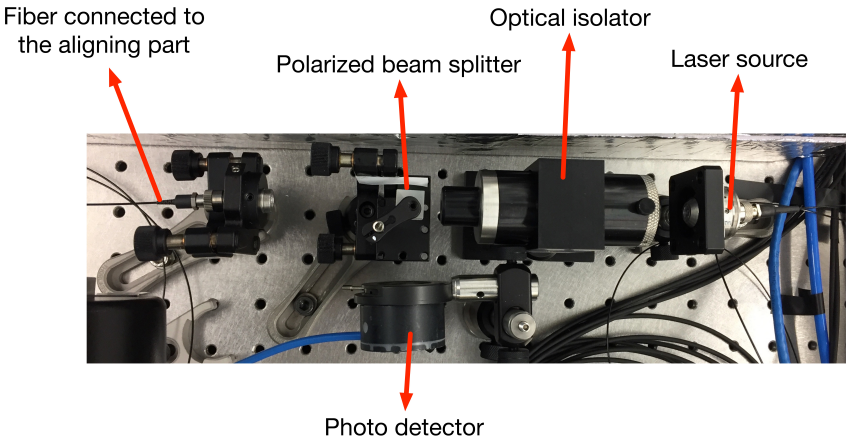

Figure 3.11: Setup used to separate and measure the reflected laser.

Laser from the source goes into an isolator which prevent the laser beam going back to the laser source by rotating its polarization. Then the beam passes through a polarized beam splitter which is used to select the polarization of the beam so that only a specific polarization can pass. This beam is sent to a collimator and delivered via a fiber to the collimator being aligned. Then it passes through a quarter wave plate, gets reflected by the mirror and passes through the quarter wave plate for a second time, which rotates the polarization in total 90°. If the alignment is correct, the reflected beam will be coupled back into the collimator. Because the polarization has been rotated by 90°, it will be reflected by the polarized beam splitter, and detected by the photo detector. Optimization is realized by finding the maximum intensity.

Alignment of the 4 way beam splitter

After the 4 collimators are aligned, it could be used to align the beam splitter. The 4 way beam splitter is made of two non-polarizing 50/50 beam splitters as shown in Figure 3.12. A CAD drawing of the light path is made to understand the geometry relationship in Appendix A.4.2.

An incident beam passes through the beamsplitter from left to right. Because of refraction, each time it travels trough a surface between air and solid, the direction changes. The reflection coating will split the original beam into two beams when it passes through. On the right side, four parallel beams with separation of 10 mm are generated. The incident angle, relative position and the overlap between the two beam splitters need to be aligned precisely.

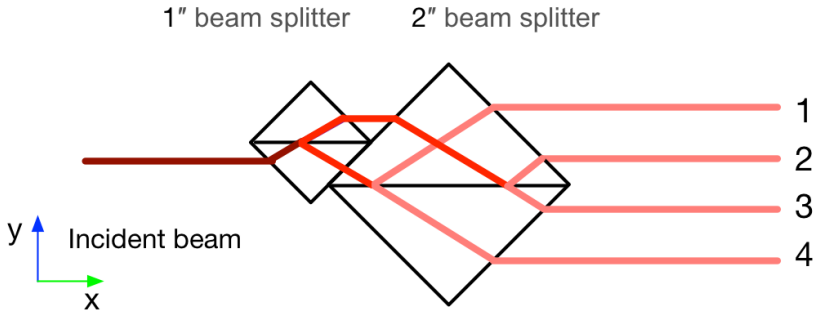

Figure 3.12: Two combined beam splitters split the incident beam into 4 equally spaced beams.

First the laser source is adjusted to provide the incident beam at the desired position. The two beam splitters are positioned roughly at the correct point. The four beams as well as the corresponding collimators are labeled from 1 to 4 from top to bottom. By exaggerating the mis-alignment, the following rules are discovered.

- Beam 3 is only sensitive the the relative angle between the 4 way beam splitter and the incident beam, disregarding how much the overlap of the two beam splitters is.
- Beam 1 and Beam 3 are coupled by the overlap of the two beam splitters. As the position of beam 3 has been defined previously, by changing the overlap, Beam 1 can be modulated.
- Beam 2 and Beam 4 are coupled together. They can be adjusted by the translation of the two beam splitters in y direction.

Based on the rules found, the following procedure is developed:

- Rotate the 4 way beam splitter relative to the incident beam until Beam 3 is coupled in the corresponding collimator.
- Adjust the overlap of the two beam splitters until Beam 1 is coupled in the corresponding collimator.
- Adjust the relative position of the beam splitter and the incident beam in y direction, untill Beam 2 and Beam 4 are coupled.

When all the beams are coupled, the alignment is finished. The two beamsplitters are glued together with a UV-curing adhesive so that step 2 can be skipped in the following alignments.

Alignment of the entire system

First, the collimators used as laser source and laser receiver are introduced into the vacuum box. Their relative position can be roughly determined by Figure A.8.

Second, the 4 way beamsplitter is introduced into the system. Based on previous developed procedure and the geometrical drawing, precise alignment can be accomplished.

Finally, the beam splitters, wave plate and the mirrors are introduced which will influence the light path. The collimators on the receiving side need to be slightly adjusted individually to optimally couple the light beam in again.

Chapter 4

Dead path measurement

After the alignment of the instrument was finished, a dead path measurement was performed. In this measurement there is no target object present. Thus all the four channels have the same optical path. The laser beams of the interferometer just passes through air or vacuum symmetrically. The result obtained from this test shows how much displacement the instrument will record in a stationary state indicating the stability of the instrument itself.

In case the measurement requires a vacuum environment, as the evacuation will deform the vacuum box resulting in a loss of signal, a pre-misalignment has to be made to compensate the beam drift due to the deformation. This will introduce an asymmetry into the system. To avoid this asymmetry and exclude the thermal fluctuations caused by the pump, the test was performed at atmospheric pressure without evacuation. The valves were closed and all bolts and nuts were fastened to provide a invariable pressure. The circulator underneath the vacuum chamber was turned on for temperature stabilization. As there was a problem with one of the photo detectors when the test was performed, only two channels inside the box were used for the test as shown in Figure 4.1

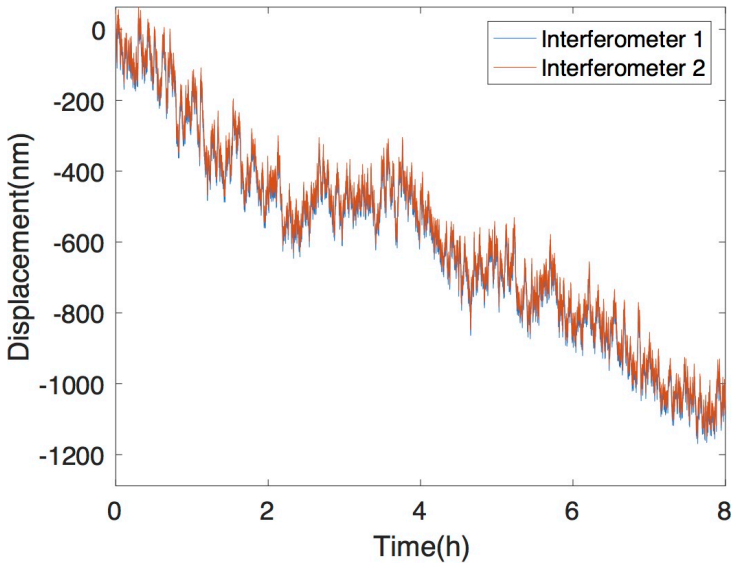

Figure 4.1: Results from a 8 hours dead path measurement. The displacement values presented here are converted from the recorded phase information.

It can be seen that during the 8 hours measurement, the total drift is 1200 nm for both interferometers. This can be attributed to the fluctuation of the external conditions including temperature variation and pressure variation for the beam preparation setup. Because of the highly symmetrical de-

sign, the two signals have strongly correlated. They almost completely overlap with each other. To observe the differential displacement, a subtraction is performed between these two channels. Now the variation is around 0.3 nm during the entire measurement process as shown in Figure 4.2.

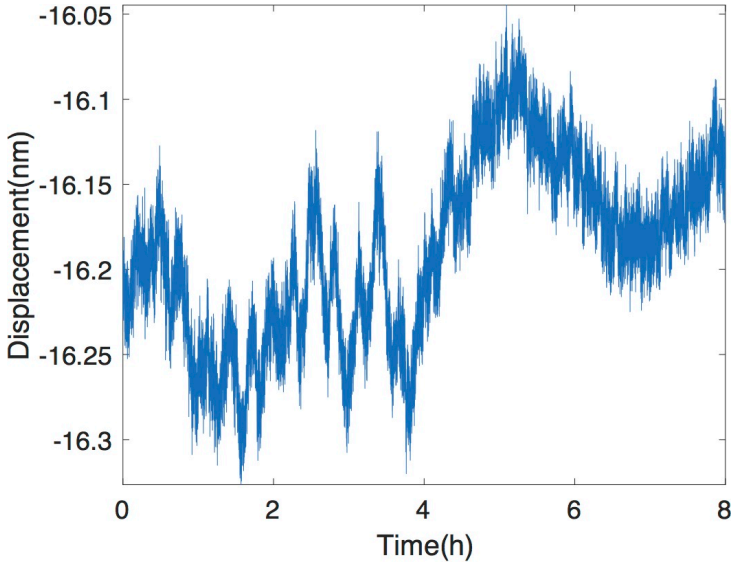

Figure 4.2: Differential result of the two interferometer channels. The refractive index and common mode vibration are compensated due to the symmetrical design. The remaining observed displacement can be attributed to the difference in environmental conditions for the two interferometers, a path length difference between the two interferometers, or asymmetries in the interferometers. The first two effects will correlate with the index of refractive measurement.

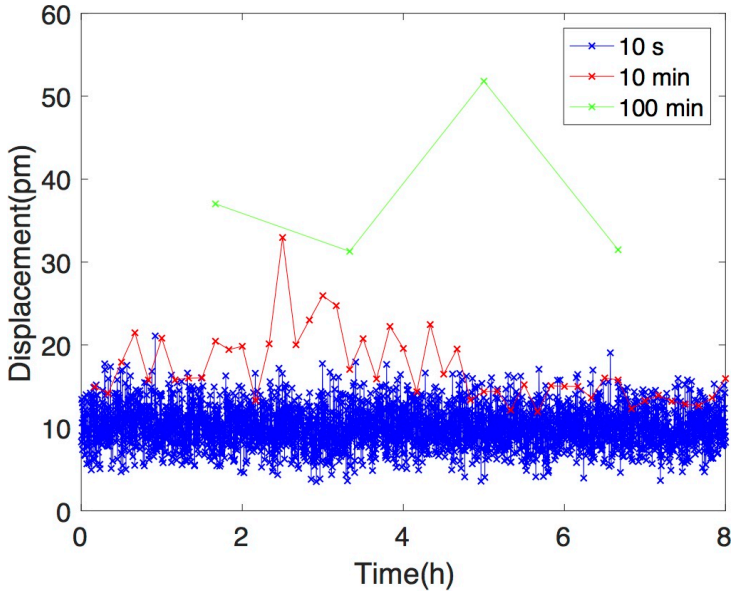

Figure 4.3: The standard deviation for intervals of 10/s, 10/min and 100/min as a function of time for the entire measured data.

The total observed difference is about 200 pm. To analyze the stability of the instrument, the standard deviation was calculated of the differential signal. Three analyzes were made for different time scales. The sampling frequency of the measurement is 30 Hz, but to reduce the data processing time an average is taken and only data points at 1 s interval are taken. The total 30 thousands points were

divided into small intervals of 10 points, 600 points and 6000 points separately which is equivalent to a range of 10 s, 10 min and 100 min. The results shown in Figure 4.3 represents the standard deviation for the 10 points, 600 points and 6000 points. From these values the stability can be observed. It shows in the interval of 10 s the stability of the whole system is around 10 pm. For an interval of 10 min the stability is around 20 pm and 40 pm for 100 min.

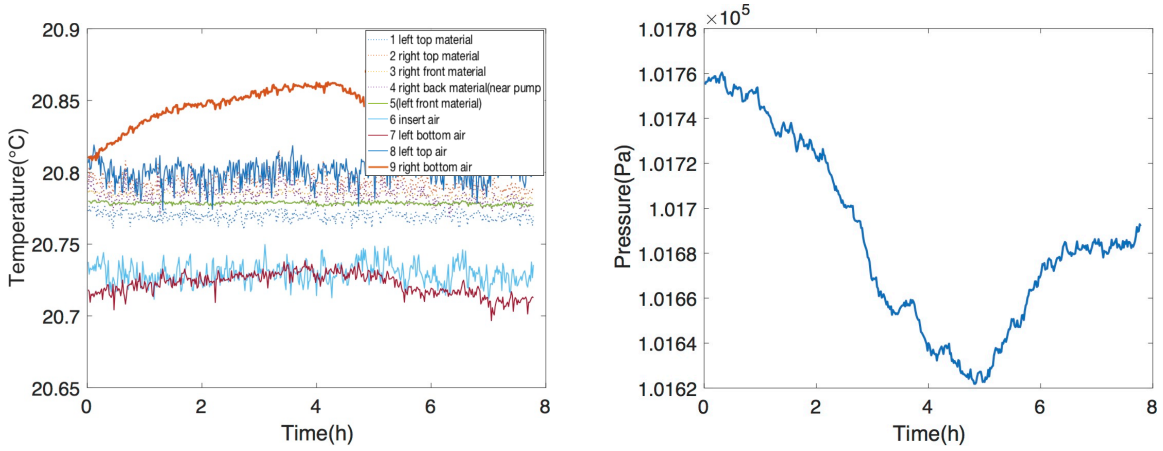

(a) Recorded temperature change during the dead path measurement.

(b) Recorded pressure change during the dead path measurement.

Figure 4.4: Recorded environment condition during the dead path measurement.

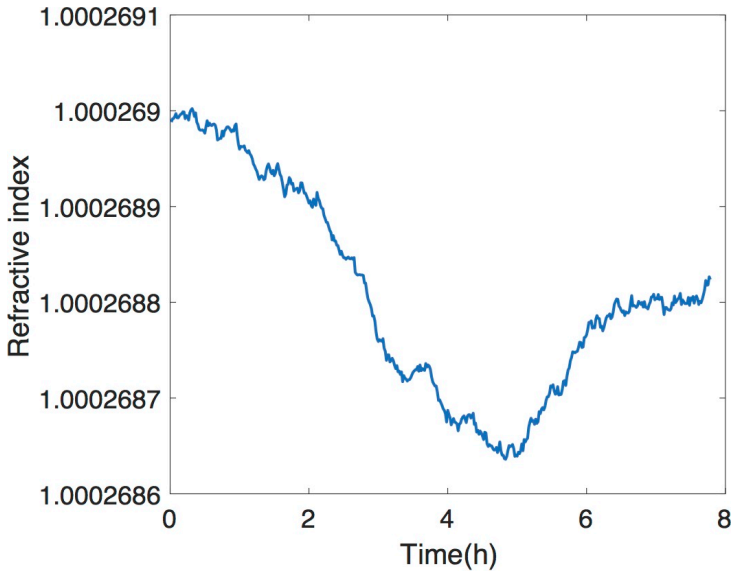

Figure 4.5: Change of refractive index during the dead path measurement. Comparing to the temperature change, It is still correlated to the change of pressure.

During the measurement, the temperature and pressure were recorded as shown in Figure 4.4. Based on this information the refractive index can be calculated as shown in Figure 4.5. Comparing it with the dead path measurement result after compensation in Figure 4.2, it could be found the correlation still presents especially at the crests and the valleys. As the change of refractive index is mainly caused by pressure fluctuation, the measurement result is expected to be improved after the vacuum box is able to evacuate without deformation.

For the later calibration, a measurement duration is expected of a few minutes, resulting in a stability of the interferometer of approximately 15 pm.

Chapter 5

Implementation of the calibration setup

Precision displacement sensors with nanometer resolution can mainly be divided into three categories: capacitive sensors, inductive sensors and interferometers. These sensors should be made traceable to a national measurement standard in order to make their results useful for comparison. Because of its high precision [18] the Fabry–Pérot interferometer [19] [20] [21] has a wide application on precision measurements. For example, 0.3 nm uncertainty in a range of 4 µm has been reached [22]. However, the main focus of these researches is on the build up of the interferometer itself not on the calibration process. When precision comes down to the picometer level, the calibration mechanism becomes a challenge. The instrument doing the calibration and instrument being calibrated together need to be considered simultaneously. In this chapter, the improved picodrift interferometer is being adapted to serve as a calibration instrument.

5.1 Capacitive sensor

Capacitive sensors make use of the property of a capacitor consisting of two conductive surfaces. When a voltage is applied to the two surfaces, a positive charge and a negative charge will be associated with the surface connected to the negative and positive electrode, respectively. If the electrodes get reversed, the attracted charge for each surface will reverse accordingly. By applying an AC voltage, an AC current will be generated. The magnitude of the current depends on the capacitor's capacitance which is determined by the following equation:

$$C = \epsilon_r \epsilon_0 \frac{A}{d} \tag{5.1}$$

where

C is the capacitance

A is the overlap area of the two surfaces

ϵ_0 is the electric constant ($\epsilon_0 \approx 8.854 \times 10^{-12} \mathrm{F} \cdot \mathrm{m}^{-1}$)

ϵ_r is relative static permittivity. It is a material property of the media in between the two surfaces (for vacuum environment, $\epsilon_r = 1$)

d is the distance between the two surfaces.

According to this equation, if the gap d between the surfaces changes while keeping the other parameters constant, the capacitance will change correspondingly. The change in capacitance will lead to

a change of current, which can be monitored using an ampere-meter. Knowing the relation between current, voltage and capacitance, the change in the gap could be derived backwards. Based on this principle the capacitive sensor can only work when a displacement is generated. Because of this, it's called a relative position sensor. Normally, commercial capacitive sensors provide an output in terms of voltage. And the change in voltage is proportional to the displacement with a factor called sensitivity, which can be expressed by the following equation:

$$S = \Delta V / \Delta d \tag{5.2}$$

where

S is the sensitivity

ΔV is the change in output voltage

Δd is the change of the gap, which is the displacement being measured.

5.2 Calibration principle

As discussed previously, a capacitive sensor is a relative position sensor. This means the actual gap size is unknown. However after calibration using external devices, the actual distance can be related to the sensor's output. This way, the gap size is directly linked to the output voltage enabling the sensor to perform absolute measurement.

The design is made to cover both relative and absolute measurement calibrations. To realize the calibration, the capacitive sensor and the interferometer are going to measure a similar displacement. Results from the interferometer will be used to calibrate the capacitive sensor. As the interferometer is also a relative measurement device, the relative measurement calibration is straightforward. However, for the absolute measurement calibration, the capacitive sensor probe and its target need to have a physical contact to initialize the measurement. This is taken as a starting point for the interferometer marked as zero for the absolute distance. From then on, the relative distance measured by the interferometer can be taken as the absolute distance between the probe front surface and the target.

The capacitive sensor chosen as a calibration example is from Lion Precision with the probe C3-D and controller DMT 22 (Appendix B.2). This sensor has a working range from 125 μm to 375 μm. In order to have a detailed measurement with enough data, the target is required to move slowly and smoothly. This means the displacement should be generated with a high resolution while keeping the vibration at a low level. The actuator chosen to generate this motion is SLC 2475 from Smaract B.2. It has a resolution on nanometer level. The detailed property of this actuator and it's behavior is carefully tested in Appendix A.6.2.

5.3 Design of the calibration stage

5.3.1 Objective

To calibrate at the sub-nanometer level, the stage should hold the capacitive sensor, the target and the mirrors for the interferometer as stable as possible. The displacement generated by the actuator needs to be transmitted by the target and measured by both instruments as similarly as possible. The objectives are set as follows:

- The difference between the actual displacement and the measurement result from the interferometer caused by the calibration stage should be smaller than 5 pm.
- The difference between the actual displacement and the measurement result from the capacitive sensor caused by the calibration stage should be smaller than 10 pm.

5.3.2 Constrains

Temperature gradient

Temperature has always been one of the most important factors that can influence accuracy of precision measurement setups. When one assumes a 1 mm thick aluminum plate is used as the target, under a temperature change of 0.1 °C, the thickness will expand or shrink 22×10^{-7} m , which is 2.2 µm. Comparing to the picometer level requirement, the value is much more than desired. Temperature variation can be separated into two situations: temperature gradients with respect to space and temperature gradient with respect to time. Assuming the capacitive sensor, reflective mirror of the interferometer and the target are made of the same material, they will have same CTE (coefficient of thermal expansion). If the temperature at any point of the setup can change with the same value at the same time (temperature gradient with respect to space is zero), by recording the temperature gradient with respect to time and proper calculation, the error could be compensated completely. This requires the material to have a conductivity as high as possible to transfer heat instantly all over the setup. Any temperature gradient in space will cause an unsymmetrical thermal expansion, which decreases the accuracy of the calibration. To prevent this, heat transfered to this setup needs to be well controlled.

Misalignment

Misalignment can easily introduce an asymmetry into the calibration setup leading to the difference between the displacements presented to the calibrating and the calibrated instrument. This includes the misalignment between the measurement and reference target within each instrument and the misalignment between each other.

Space

The structure of the vacuum box of the interferometer limits the space available for the calibration setup as shown in Figure 3.1. The gap between the inner beam and the wall is only 2 mm. This sets the boundary for mirror size, mirror mount, and the way how calibration can be executed. Additionally, the cable of the capacitive sensor requires some space to be relaxed, otherwise it may cause undesired distortion of the sensor or break itself.

Undesired actuator motion

In practice, the actuator will not only generate motion in the required direction, but also an undesired rotation. This rotation will cause a difference in the detected displacements for the two instruments, which may destroy the quality of the calibration.

Others

Aiming at the picometer level is indeed challenging as there are many possibilities that will induce an uncertainty that needs to be minimized or compensated. Apart from the constrains discussed above, the quality of the mirrors, vibrations, the mounting method for the capacitive sensor and mirrors, and the electrical isolation of the sensor need to be taken into consideration.

5.3.3 Concept generation

Based on the constrains and objectives, two conceptional designs were generated. They are distinguished by the angle between displacement direction and measurement direction.

Parallel concept

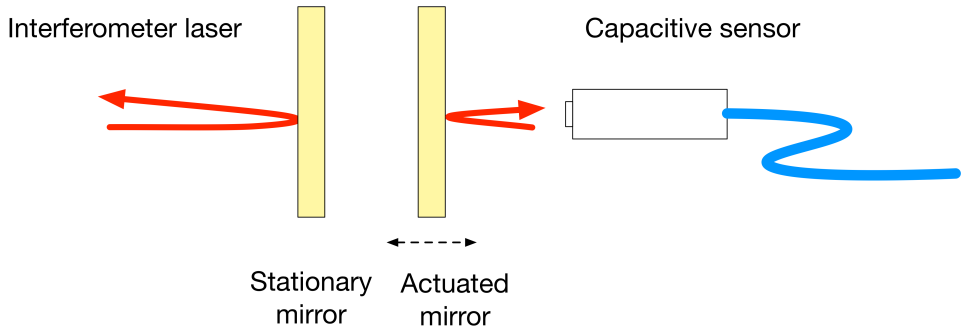

Figure 5.1: Parallel design concept for the calibration setup. The displacement direction is parallel with the measurement direction.

When it comes to dimensional measurements, the Abbe error will be one of the fundamental issues to be considered. It is also known as the amplification of angular errors. “If errors in parallax are to be avoided, the measuring system must be placed co-axially with the axis along which the displacement is to be measured on the workpiece. [23] ” It means that if the sensor is placed away from the measured target, an error caused by angular error will be amplified. To completely avoid this error, the laser beam, capacitive sensor probe and the moving target should be in line. A similar design has been applied by H. Haitjema [24] on a Fabry-Perot interferometer which is also currently at VSL. However, it is not very practicable for the picodrift interferometer.

Assume the Abbe principle is followed strictly. The capacitive sensor must target the back of the mirror at the same point where reflection is supposed to happen for the interferometer laser beam as shown in Figure 5.1. But the capacitive sensor probe will block the laser beam from reaching the mirror surface. An improved concept as shown in Figure 5.2 is developed.

However this design will cause a lot of errors as a result of temperature fluctuations:

- Thermal expansion and vibration of the stationary mirror is measured by the interferometer alone. The capacitive sensor will not detect anything from it.
- Thermal expansion of the actuated mirror can be measured differently because of the mirror thickness.
- The two mirrors have to be mounted on some mounting system underneath. Due to the length of probe head, the material will be relatively long and could cause a large uncertainty when compensating for thermal expansion errors.

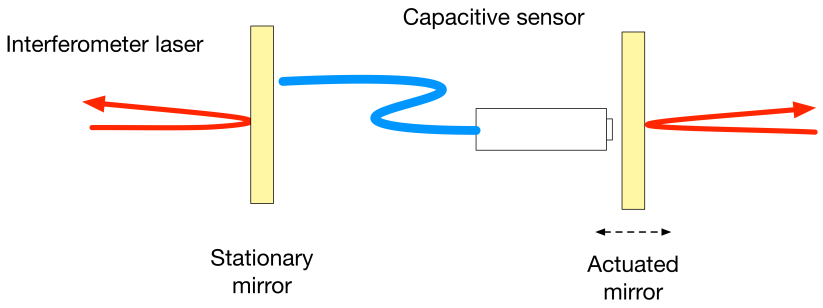

Figure 5.2: Parallel calibration concept to avoid Abbe' error

- The unpredictable behavior of the mount for the capacitive sensor will also cause additional error because of thermal expansion.
- Thermal expansion of the capacitive sensor probe will introduce error that can only be detected by itself.

Improved parallel design concept

To decrease the large uncertainty due to thermal expansion, an improved concept was designed as shown in Figure 5.3.

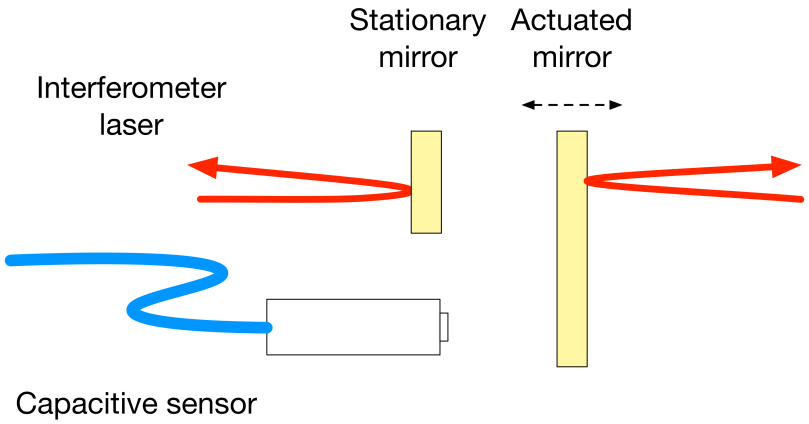

Figure 5.3: Improved parallel calibration setup design concept. The capacitive sensor probe is fixed together with a stationary mirror.

Now the capacitive sensor is mounted together with the stationary mirror. The actuated mirror is coated with gold on two surfaces so that it can be used as the target for both the interferometer and the capacitive sensor. In this configuration, thermal expansion of the mounting system underneath can be ignored as it will effect both instruments at the same time in the same way. For the interferometer the sensitive distance is between the two outer surfaces of the gold coated mirror. But for the capacitive sensor the sensitive distance is from the front of the probe to the inner surface of the actuated mirror. The difference is the thickness of the two mirrors plus the distance between the front of the probe and the inner surface of the stationary mirror. As this configuration violates Abbe's principle, the related error has to be compensated afterwards.

Perpendicular design concept

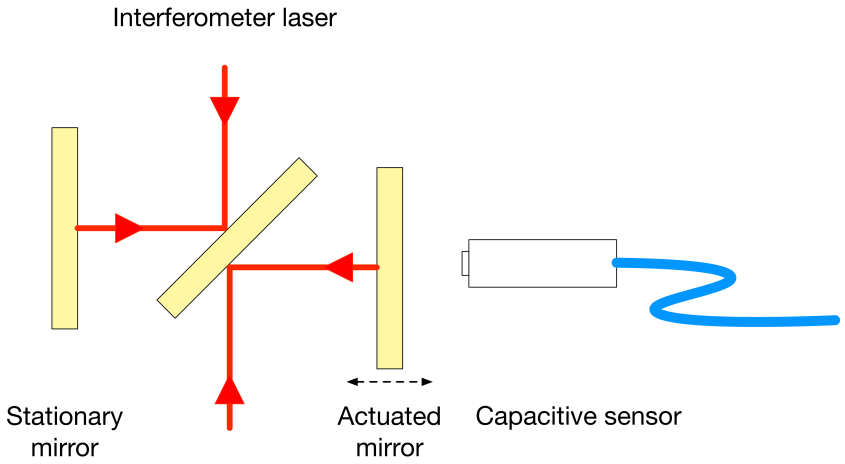

Figure 5.4: Perpendicular concept for the calibration setup. The displacement direction is perpendicular to the measurement direction.

In the perpendicular design concept, the capacitive sensor is no longer constrained by the small measurement space of the interferometer. Cable and probe of the capacitive sensor can stick out of the instruments as shown in Figure 5.4. This makes the setup more adaptive for sensors with different sizes. The down side is that this design causes a lot of errors including the thermal expansion error as discussed during the first parallel concept. Also the perpendicular concept will need extra alignment efforts to make it work properly.

Improved perpendicular design concept

Inspired by the Wheatstone bridge, a more symmetrical design as shown in Figure 5.5 allows compensating errors.

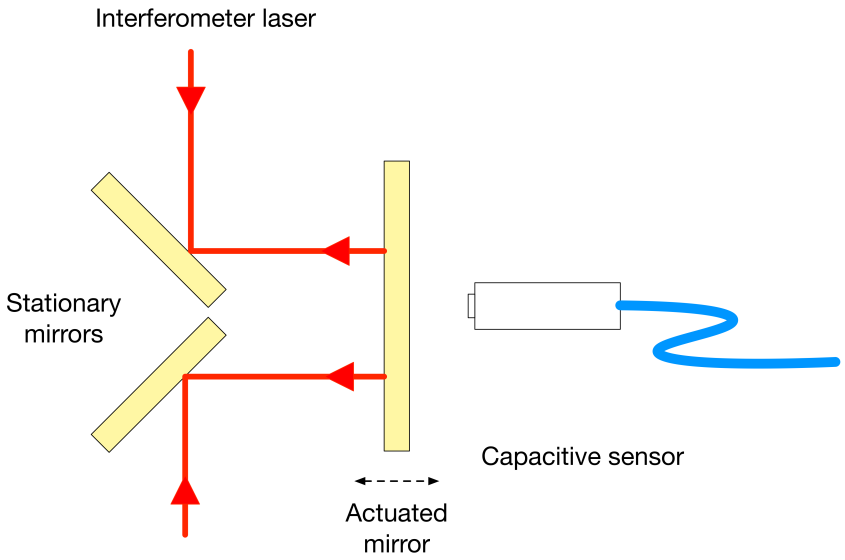

Figure 5.5: Improved perpendicular concept.

The two laser beams are deflected by two 45° inclined stationary mirrors to be delivered to the actu-

ated mirror. On the other side the capacitive sensor is facing the actuated mirror. When the actuated mirror moves, the signal is captured by both instruments. The symmetrical design enables the alignment of the actuated mirror to not be so critical. This is because information from the two measured point can average out the tilting and rotation of the target. However the thermal expansion error is still not fully resolved. The alignment of the mirrors remains critical.

5.3.4 Calibration setup

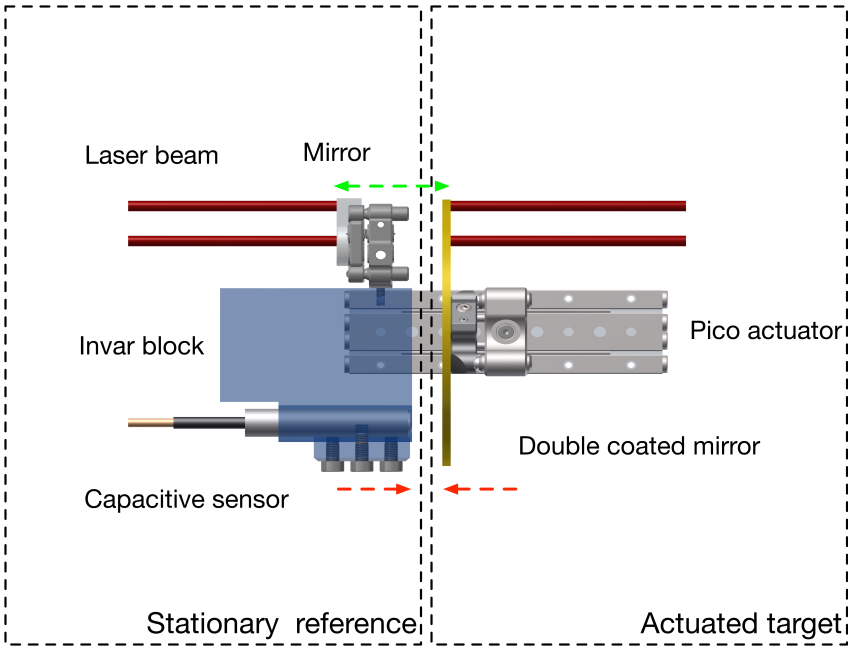

Figure 5.6: Top view of the calibration setup. The stationary reference part and the actuated part are both mounted on a customized aluminum base. The stationary reference is mounted by kinematic coupling while the actuated part is mounted by bolts. Underneath the aluminum base is a commercial stage providing adjustment with four degrees of freedom.

Based on all the arguments and the possibilities, the improved parallel design was chosen to be developed and implemented further. The setup can be divided into two parts: the stationary reference and the actuated target. The stationary part is made of invar which is a metal with low thermal expansion coefficient B.1. The capacitive sensor probe and the reference mirror for the interferometer are mounted on the invar block shown as semitransparent in Figure 5.6. Mounting of the capacitive probe is realized by the clamp along three lines, which prevents any translation or tilt on both lateral and longitudinal axises. Mounting of the mirror is assisted with a commercial kinematic mount with three degrees of freedom, which will help in the alignment process. The actuated target part consists of a piezo linear stage and a two side coated mirror. It has a customized semicircle shape and is coated with bare gold. The gold surface makes it conductive for the capacitive sensor and reflective for interferometer laser. When calibration is performed, the invar block with reference mirror and capacitive sensor probe is kept stationary. The piezo stage will generate a displacement which is transferred to the gold mirror. As the gold mirror is a common target, this displacement is sensed by both instruments. Then measurement result from the interferometer is used to calibrate the capacitive sensor.

5.4 Alignment procedure

In order to minimize geometrical misalignment errors, the following alignment procedure is developed.

Capacitive sensor probe and target

For an interferometer, the straightness of the laser beam provides a reference for the alignment of the target. But the alignment between the capacitive probe and its target is a challenge as the only geometrical reference that can be used is the front surface of the probe. To make sure the surface is parallel with respect to the target, an external autocollimator is used. Firstly, a mirror is adhered to the probe front surface with the reflective surface against the probe surface. Then the autocollimator is used to measure the relative angle between this mirror and itself. After that, the invar block together with the capacitive sensor probe is removed from the base. Now the target mirror is exposed to the autocollimator. Using the mirror mount attached to the target, the relative angle between the target and the autocollimator can be adjusted to be similar as the previously measured value. Now the probe and the target are parallel using the autocollimator as a reference. Afterwards, the invar block is put back on the base. As the probe has no individual adjuster, its position relies on good repeatability of the kinematic coupling. According to the test, the best repeatability with minimum error could achieve $1''$. During alignment the attached mirror is assumed to be parallel with the probe, but the surface quality may cause some extra uncertainty.

Stationary and actuated mirror of the interferometer

To have the stationary and actuated mirror interact with the laser beam, they are required to be aligned parallel to each other. Firstly, a double coated mirror with two parallel surfaces (error below $0.1''$) is used to set up a measurement system with two autocollimators parallel aligned against each other. Then the calibration setup is put between these two parallel autocollimators with the mirror surfaces facing them. Irrelevant reflective surfaces are blocked by paper, only leaving the two mirrors exposed. Because the actuated mirror is already aligned (as it is the same part used as the capacitive sensor target), the stationary mirror mount and stage underneath could be adjusted to make the two mirrors parallel to each other based on the readout of the autocollimators.

Calibration setup and the interferometer

Now, the stationary and actuated parts are aligned. Next, the calibration setup can be put into the measurement window area, by adjusting the base stage, the two laser beams from the interferometer will interact with the stationary mirror and the actuated mirror, which have been aligned parallel to each other in the previous step. Optimal alignment is obtained by having the maximum signal from the photo detector, which indicates how much laser light can follow the old path when no objects were present. With the finalization of this step, the entire setup is aligned.

5.5 Uncertainty analysis

In this section, the uncertainty caused by thermal expansion and misalignment for the calibration setup is discussed and quantitatively characterized.

5.5.1 Temperature variation

Thermal expansion of the calibration setup can be divided into three parts. The first part is caused by the actuator stage and the aluminum base underneath. Because the expansion will lead to a relative displacement between the reference and actuated part which can be detected equally for both the interferometer and the capacitive sensor, this part can be ignored.

The second part is the uncommon sensitive path for interferometer and capacitive sensor. For the interferometer, the sensitive path is from the stationary mirror surface to the actuated mirror indicated by the green arrow in Figure 5.6. The sensitive path for the capacitive sensor is from the front surface of the probe to the gold coated mirror surface indicated by the red arrow. The difference is the thickness of the actuated mirror and the distance from the probe front surface to the stationary mirror. As the thickness of the mirror is known, the corresponding thermal expansion can be compensated. The distance from the probe front surface to the stationary mirror can be eliminated by a customized mirror mount to bring the uncoated surface of the stationary mirror closer to the probe.

However, errors can be caused in the previous process. Material properties are determined in a specific condition, which means the thermal expansion coefficient may not be fully applicable for the material being used. And the distance is hard to be measured accurately due to the errors introduced by the mounting method, the manufacturing error, and so on. Considering these factors, the uncertainty of the manufacturing accuracy is estimated to be 100 µm. During a measurement, the environment temperature is well controlled to have a thermal stability below 1 mK/h. The thermal expansion coefficient for Invar is 1.5×10^{-6} m/m°C. This results an uncertainty of 0.15 pm in calibration .

5.5.2 Misalignment

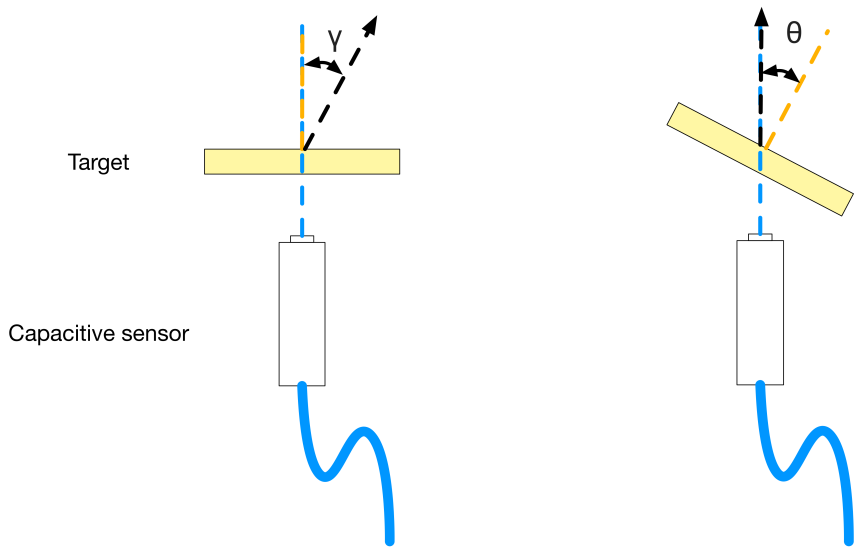

(a) Misalignment between the measured direction and the direction of displacement.

(b) Misalignment between the probe surface and the target surface.

Figure 5.7: Two kinds of errors caused by misalignment of the capacitive sensor. The blue line indicates the normal direction of the probe, the orange line is the normal direction of the target surface. The black line is the direction of motion of the target.

Cosine error

The cosine error is used to describe the situation where the target does not move collinear with the measured path but with an angle γ deviating from the normal line as shown in Figure 5.7a. It is a purely geometrical error. Because the interferometer and the capacitive sensors are facing the same target, as long as the common target does not tilt, the effect of cosine error will be the same for both. As the measured displacement does not need to be the same as the displacement generated by the actuator, this error will not play a role during calibration.

Angle between the probe and its target

In comparison with the interferometer, the capacitive sensor is less sensitive to pressure and temperature fluctuation. However, if the probe is not perfectly orthogonal to the target, a geometrical error will be introduced. According to the manufacturer [25], the error caused by this misalignment is estimated by the following equation:

$$U = \left(\frac{1 - \sqrt{1 - (\frac{r \cdot \theta}{d})^2}}{2} \right) \cdot d \cdot k \tag{5.3}$$

where:
U is the error caused by this misalignment

r is the radius of the probe sensor area in meters

d is the probe to target gap, directly under the probe center axis in meters

θ is the probe to target angle in radians

k is the experimentally determined constant to account for field fringing errors.

According to Equation 5.3, the relation between the misaligned angle and the resulting error is plotted in Figure 5.8. Based on the alignment procedure, this alignment is mainly limited by the accuracy of autocollimator. After a stationary test, the accuracy of the autocollimator is found to be $0.4''$ (A.6.1). This accuracy will be accumulated to be $1.6''$ during alignment as the autocollimator is used multiple t5imes. Because the invar block is relocated once during alignment, the repeatability error caused by this relocation is $10''$ according to multiple tests. In total, the $11.6''$ misalignment will lead to an uncertainty of 9.8 pm.

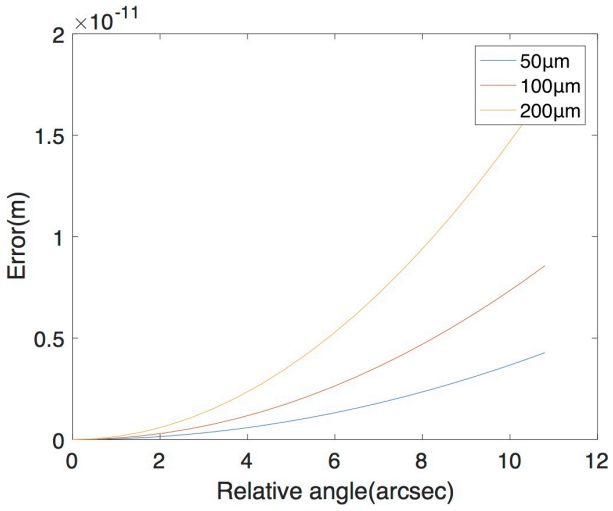

Figure 5.8: Error caused by misalignment of capacitive sensor calculated with the gap sizes of 50 µm, 100 µm and 200 µm.

Stationary and actuated mirror for the interferometer

A similar alignment procedure as previously discussed is applied to the stationary and actuated mirror for the interferometer. So the 1.6″ error remains the same resulting in an error in length of 0.003 pm, which is neglect able. Different from the way how capacitive sensors work, the interferometer uses a laser to do the measurement. As a property of light, the laser beams are considered as straight in design. To have the interferometer still receiving the reflected laser beam after the calibration setup is put on its channel, the stationary mirror and actuated mirror must be perpendicular to the laser beam. This sets a limit for the angle error between these two mirrors.

Abbe error

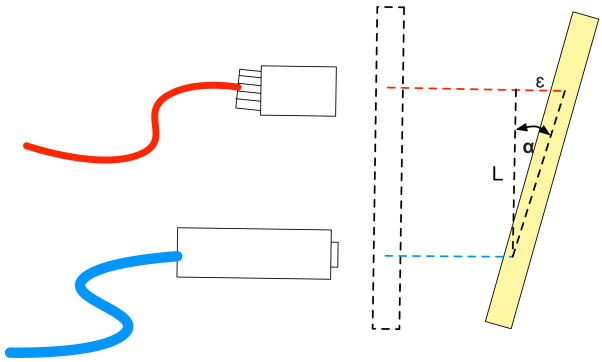

Figure 5.9: Abbe error.

Another significant error in this setup is Abbe error illustrated in Figure 5.9. This is a simplified drawing of the calibration setup. The laser head is indicated by collimator connected to the red line while the capacitive sensor is connected to the blue line. They are both facing to the same gold mirror target and supposed to measure how much the target moves during the calibration. In practical, the target does not only generate a translation straight to the right or left, but also an undesired rotation α. This angle, combined with the distance between the two sensor heads L causes an extra displacement ϵ sensed by the interferometer. If this error is not compensated during calibration, it will be taken as the capacitive sensors own error and be attributed to the sensor property, which decreases its accuracy. This error is called Abbe's error and described as the error caused by non-collinear measurement to the target. To have a rough estimate of the magnitude of the error, the rotation of the actuator is measured by an autocollimator described in A.6.2. During a travel distance of 25 mm, the rotation along the x axis is 12″ and the rotation along the y axis is 50″. But it was found that the rotation has a good repeatability. After five measurements, the largest deviation is under 2″. Taking the distance between the capacitive sensor probe and the interferometer channel as 20 mm, the uncompensated Abbe error will still cause an uncertainty of 0.2 nm. The solution is to employ another interferometer channel parallel to the measurement channel as shown in Figure 5.6. By comparing the displacement from both channels, the Abbé error between them can be estimated. Based on that, the rotation angle of the target can be derived and compensated from the calibration. Quality of this compensation depends on the manufacture precision. During the example calibration, it was found that the rotation of the stage is only 0.04″ for a displacement of 100 µm. So a 0.1 mm manufacture error will cause an uncertainty up to 19 pm.

Uncertainty of the inside of the interferometer

The uncertainty of the interferometer is estimated based on the previous dead path measurement. In a duration of 10 min, the uncertainty of the calibrating instrument is 15 pm.

Table 5.1: Uncertainty analysis for a calibration range of 100 µm.

Uncertainty source	Uncertainty	Contribution
Uncompensated thermal expansion		0.15 pm
Misalignment of capacitive sensor head and target	11.6″	9.8 pm
Misalignment of interferometer reference and target	1.6″	0.003 pm
Rotation of actuator	4″	19 pm
Interferometer uncertainty	15 pm	15 pm

5.6 Calibration examples

Because of the large vibrations (of the level of hundreds of nanometers) of the actuator stage during motion due to stick-slip principle, the calibration has to be made discontinuously. The entire calibrated range is divided into small intervals. The actuator is used to generate small displacements of hundreds of nanometer each time. After each motion, several seconds is allowed to wait for the stabilization of the system before the next step. The entire measurement looks like a stair shape in the plot of displacement versus time as shown in Figure 5.10. The measurement range of the calibrated capacitive sensor is 250 µm. Settings of the actuator controller is listed as follow: closed loop mode, maximum control frequency of 50 Hz, displacement of 10 µm, velocity of 10 µm s^{-1}, and an acceleration of 20 000 µm s^{-2}. As described in 5.3.4, the two interferometer channels are used to do the measurement at the same time aiming to determine the rotational error during the motion. The interferometer in the vacuum chamber measuring the refractive index is used to compensate for external vibration.

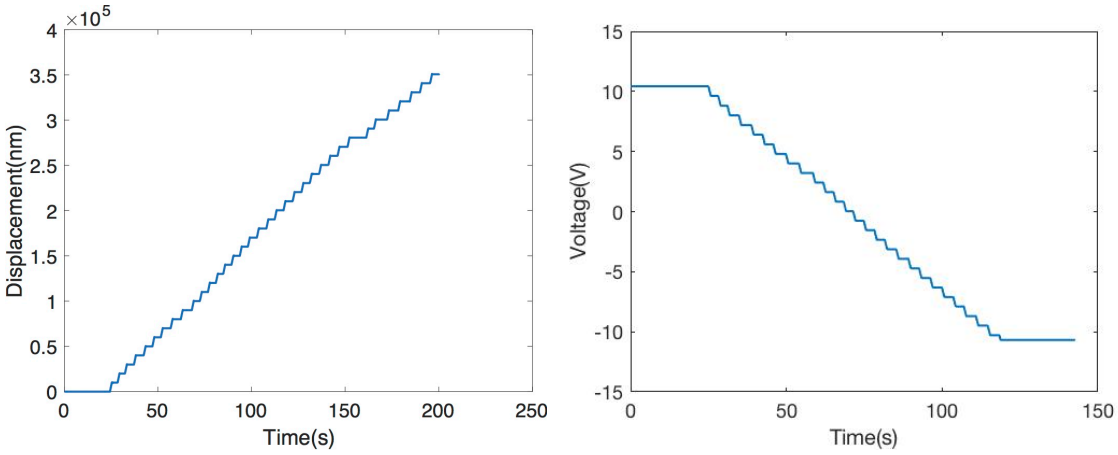

(a) Displacement measured by the interferometer.

(b) Output of the capacitive sensor.

Figure 5.10: Results of the two instruments for the same displacement generated by the actuator. Because of the large vibrations of the actuator stage, a discontinuous calibration was preformed. The entire measurement looks like a stair shaped plot as the displacement versus time plot. After 280 µm, the capacitive sensor is out of range.

With measured results for both instruments available, a calibration could be made. Using a fit algorithm the sensitive function for the capacitive sensor is determined to be

$$\Delta V = 7.935 \times 10^{-5} \cdot \Delta x \tag{5.4}$$

with sum of squares of the residue of 0.083 V and root mean square error of 0.0183 V.

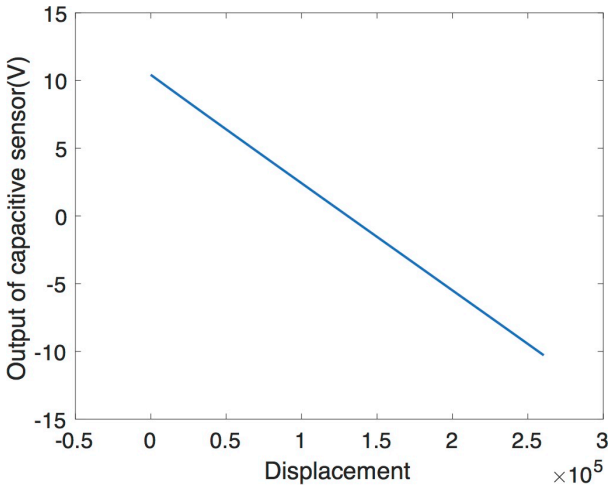

Figure 5.11: Calibration diagram. The calibration data is taken at similar time stamps. During each stationary step, the position measured from the interferometer and the voltage output from the capacitive sensor are averaged. These two sets of data are used to make this diagram.

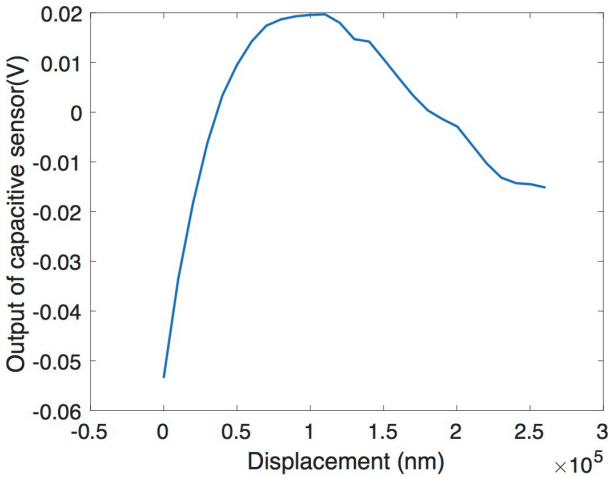

Figure 5.12: Residue after the linear fit.

An important uncertainty considered during the design is the rotational error caused by the actuator during the displacement. A subtraction is made between the two interferometers signals as shown in Figure 5.13. During the total displacement of 280 µm, The maximum difference is 5 nm. The largest deviation happens at the first 150 µm. In the following 100 µm, the difference goes down to 1 nm. Taking the distance between these two channels to be 1 cm, the rotation of the actuator is only 0.04″. Using the sensitivity calculated previously, the measured voltage from the capacitive sensor can be interpreted as displacement. The difference between the measurement results from the two instrument can be compared. As the interferometer has no non-linear problems, the difference sensed by these two channels are purely caused by rotation of the target stage. However the difference between

the capacitive sensor and the interferometer channel is 1 µm. This large difference can not be explained by the rotation alone. According to geometrical model, the largest value can be expected is below 10 nm. Additionally, the correlation of the difference between the capacitive sensor and the interferometer and the residue after the linear fit is very high. Then it can explained by the nonlinearity error of the capacitive sensor.

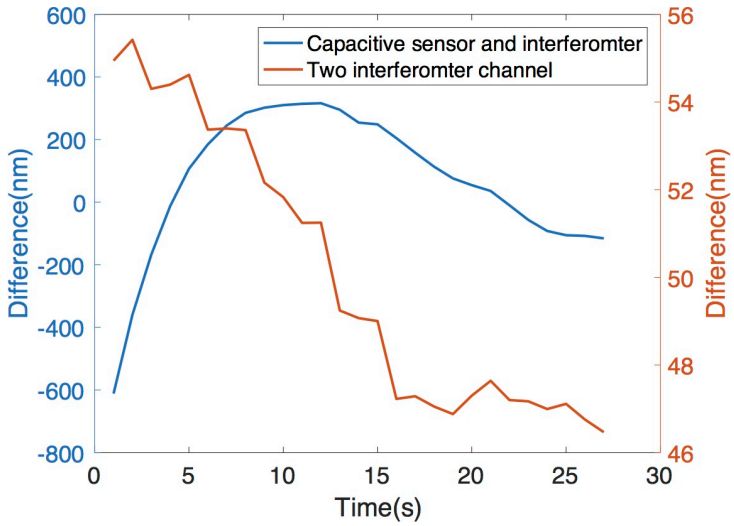

Figure 5.13: Difference between the two interferometer channels and the difference between the capacitive sensor and one of the interferometer channel.

Chapter 6

Conclusions & Recommendations

6.1 Conclusions

In this thesis, the improved Picodrift interferometer was implemented and tested to make dimensional drift measurement with a better stability and controlled environment. Additionally, a calibration setup was successfully designed, implemented and demonstrated in practice.

Firstly, to realize a controlled environment, the vacuum box was assembled including the necessary sealing elements, turbo pump, pump station, valves and flanges for the feedthroughs. A clean procedure for elements to be placed in vacuum was developed, based on the material properties aiming at UHV (ultra-high vacuum). With the help of a Helium leak detector, a final pressure was reached of 6×10^{-6} mbar. An active temperature control using an external circulator and passive shielding of foam box renders the temperature stability better than $1\,\mathrm{mK\,h^{-1}}$. An optimal alignment plan was determined and executed to make the interferometer work according to the designed optical path. The highly symmetrical optical system and the customized kinematic coupling keeps the stability of the interferometer below 10 pm. The long term stability was bellow 40 pm for a duration of an hour.

Secondly, a parallel calibration setup was designed, manufactured and implemented in order to calibrate an external precision sensors. During the design stage, the uncertainty caused by thermal expansion, misalignment and undesired motion of actuator were considered and minimized resulting in an uncertainty of 30 pm. A calibration of a capacitive sensor was successfully demonstrated resulting in a sensitivity of the sensor of 0.079 V/µm and nonlinearity of 0.4% over the full range of 250 µm path.

6.2 Recommendations

In terms of operation of the interferometer, a few of recommendations are proposed to improve the setup further.

One of the most unexpected problem was the drift of the laser beam from the desired point resulting in a complete loss of the interference signal. It was found to be caused by a deformation of the vacuum box due to the pressure change during evacuation. The current temporal solution is to make a pre-misalignment before the system is evacuated. However, this introduces in asymmetry into the system which may decrease the accuracy of the refractive index and vibration compensation. Besides, this offset needs to be experimentally determined depending on how the lid is fastened by the bolts and nuts to the box body. A better permanent solution would be to detach the optical

elements from the base of the vacuum box and put them on a separate plate that is kinematic coupled to the base.

Beam drift is not the only problem caused by the deformation of the vacuum box. According to the vacuum leakage test, the largest leak is detected at the connection between the lid and the body. A COMSOL model has proved that the deformation of the box may lead to a nonuniform sealing around the o-ring, which causes the large leakage. If the vacuum box will be replaced in the future, it is recommended to divide the large opening at the top into several smaller openings so that the box will have a stiffer structure and each opening will be less influenced by the deformation.

At this stage, the temperature is controlled by the external circulator, which stabilizes the temperature by sensing the input flow temperature. This mechanism is inefficient. Improvement is possible by feeding the temperature information inside the foam box to the water circulator directly and build up a better temperature control loop.

A more symmetrical 4 way beam splitter and beam combiner have been designed and analyzed as shown in Appendix A.4.2. With this improvement, the beam intensity distribution will become more uniform which will provide a better compensation for refractive index and vibration. Additionally, the new beam combiner will make the coupling of laser beams to the collimator easier due to a more symmetrical structure.

During measurements it was found that the interference signal is very sensitive to the vibration of the segment of the laser fiber which feeds the laser into the vacuum box. This indicates that either the fiber is damaged or the polarization coupling of the fiber feedthrough is not very stable. Further research and experiments can be performed to explore this sensitivity. A different fiber/fiber feedthrough can be considered to remove this dependency.

Appendix A

Appendix

A.1 Uncertainty of the 4 way beam splitter

The 4 way beamsplitter is one of the components that still have room to be improved. The current version is made by two beam splitters as shown in Chapter 2. However, because of the unsymmetrical design and error of the 50/50 beam-split coating which was designed for 45° incidence, the intensity of the laser beams coming out are not equal. Additionally, due to the in house gluing technique the quality is not guaranteed. Hence a new concept was generated as shown in Figure A.1. It is made of 4 pieces of fused silica and has a more symmetrical design. To make sure the design fulfills the requirements in terms of light intensity and geometrical alignment, the following error budgeting was established.

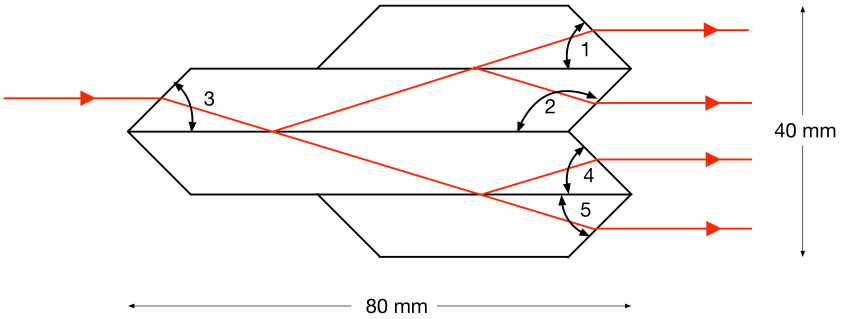

Figure A.1: A symmetrical 4 way beam splitter.

Assuming the 4 beams are required to have a parallelism better than 30 arcsecond, and the separation should have an error better than 0.1 mm the design accuracies can be determined. When the influence of one parameter is being studied the other parameters are set to be the correct values. The following table shows the maximum error allowed for the above mentioned accuracy.

A.2 Calculation of refractive index

Using MATLAB the relation between the pressure, temperature and refractive index could be estimated from the Edlén equation 3.2 3.3. The plot is shown as below:

Table A.1: Error budgeting.

Label	Nominal Value	Error	Induced error
1	45°	0.01°	30″
2	135°	0.01°	30″
3	45°	0.02°	30″
4	45°	0.01°	30″
5	45°	0.01°	30″

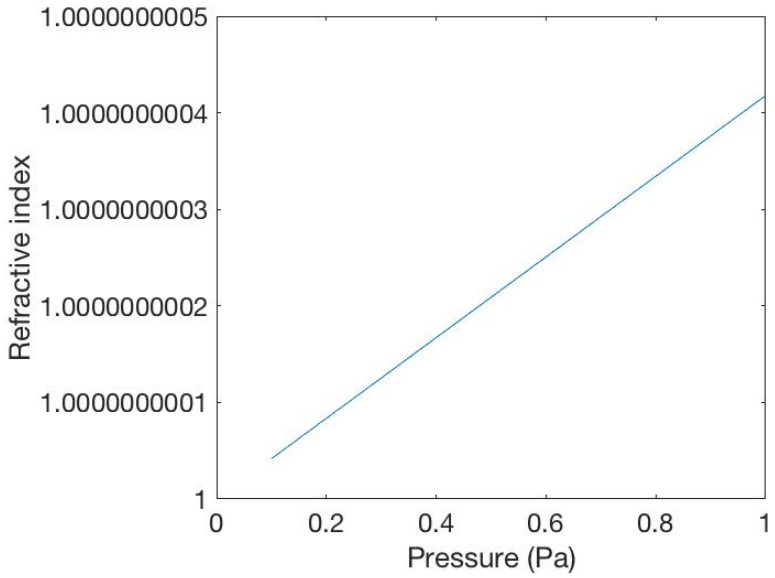

Figure A.2: Change of refractive index with respect to the change of pressure.

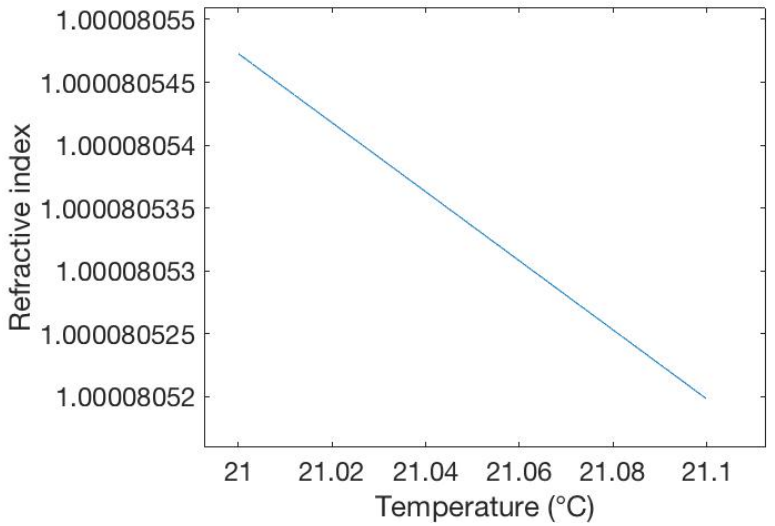

Figure A.3: Change of refractive index with respect to the change of temperature.

As the function used to plot these figures for the vacuum environment is out of the specified valid range, it can only be used as an estimate.

A.3 Leak detection

There are many ways to detect a leakage in a vacuum system. The most common ones are listed below.

A.3.1 Thermal detector

This methods is suitable when a large leakage is expected. It assumes that the leakage is so large that the air flow from the leak is accelerating the air locally, which speeds up the evaporation from an applied volatile solution nearby. The evaporation causes a change in temperature that can be detected using a thermocouple.

A.3.2 Using Alcohol

This method makes use of the molecular size of alcohol to penetrate through a leak into the vacuum chamber. Because of the sudden pressure change the alcohol will freeze to become solid and fill the leakage temporarily. This will cause a pressure change that can be measured by the barometer. Some other chemicals may also be used, but the change in pressure may be purely caused by the mixing of gas with a different molecule size. This method is easy to be applied, but the alcohol may dissolve the o-ring and enlarge the leakage.

A.3.3 Leak detector

A leak detector is a professional instrument to determine the leakage which is applied in the following test. It consists of a turbo pump and a helium detector. When it is switched on, the turbo pump evacuates the chamber and senses the helium vented in the flow. Helium gas is sprayed around the possible leakage areas to allow it to enter the chamber. By measuring the density of the helium gas in the flow, the size of the leakage can be determined.

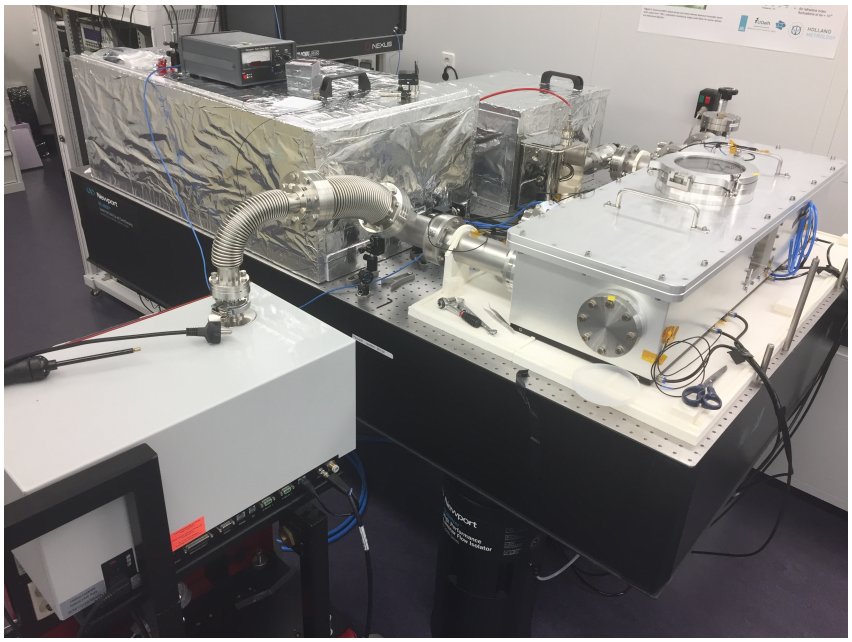

Figure A.4: Picture of the instrument when the leakage is being detected.

The leak detection has been performed twice. During the first test, the leak detector was connected to the chamber via a 6 mm tube which is too small for the large chamber. The flow is so slow that the response time is larger than 2 min, which means whenever helium is sprayed around a leakage it takes two minutes for the flow to reach the detector and get sensed by the machine. And it takes even longer to wait for it to be completed evacuated and allow for the next test. During the second test, a larger tube was used which has the same diameter as the opening of the pump. The response time is reduced significantly to several seconds. The following result is generated indicating the size of each possible leakage.

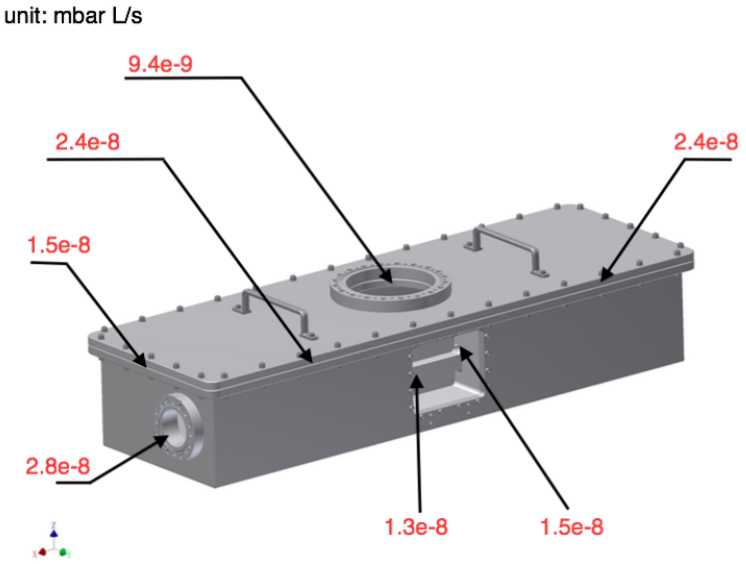

(a) Front of the instrument.

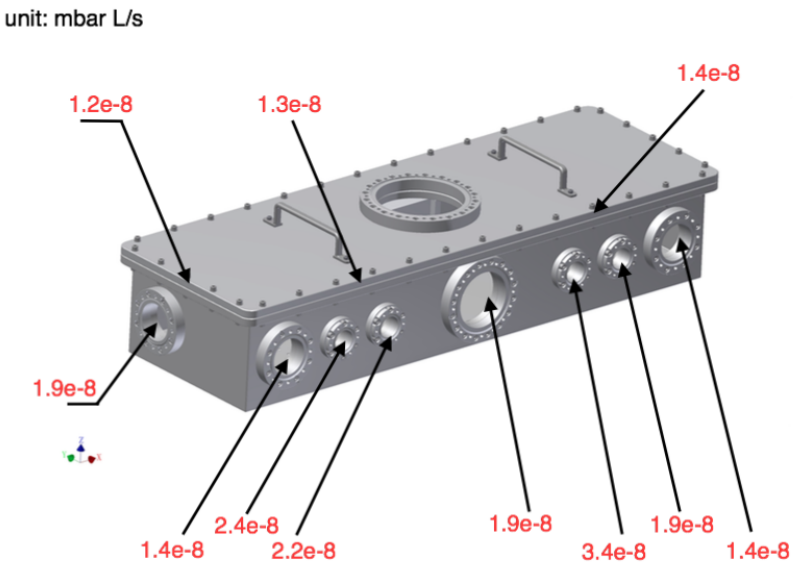

(b) Back of the instrument.

Figure A.5: Leakage rate detected during the first test.

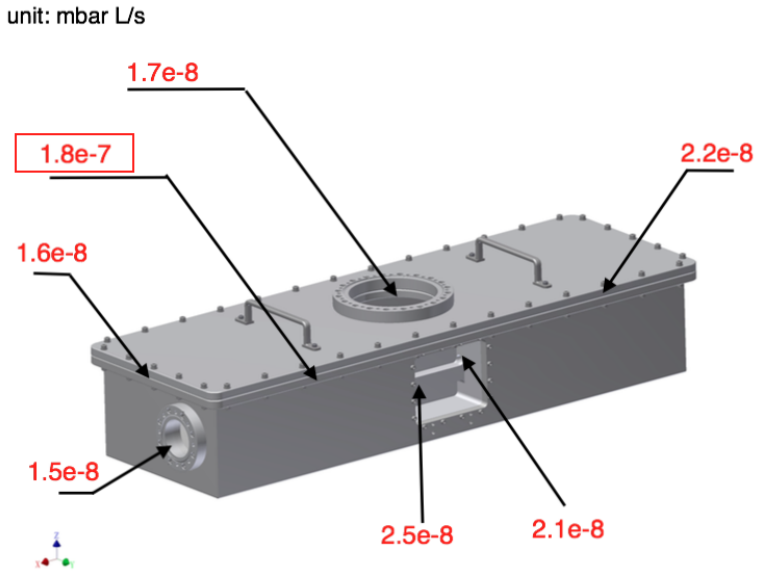

(a) Front of the instrument.

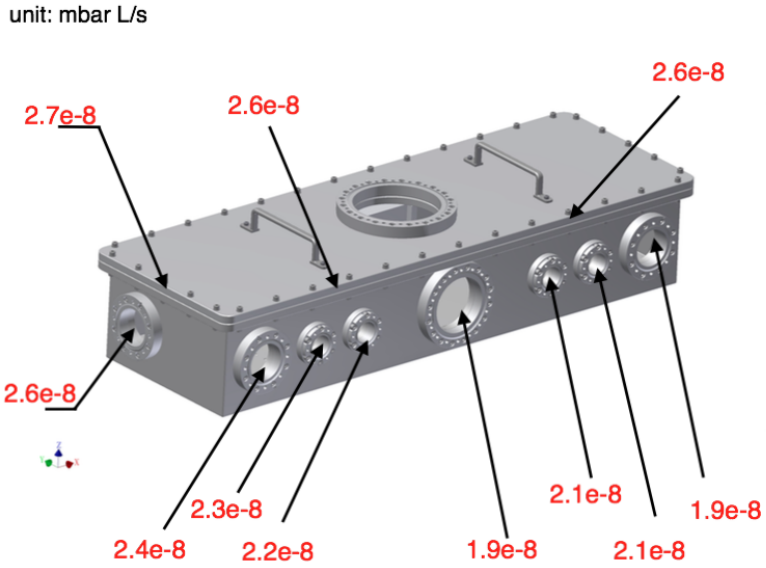

(b) Back of the instrument.

Figure A.6: Leakage rate detected during the second test.

The measured values are given in the unit of mbar L/s, which is calculated by the following equation:

$$Q_L = \frac{\Delta p \cdot V}{\Delta t} \tag{A.1}$$

where Q_L is the leakage rate

Δp is the pressure change in the measurement period

V is the volume

Δt is the measurement period.

According to the result, the gap between the lid and the chamber is the place where the largest leakage happens. It is one order larger than the other spots. This shows the sealing of the o-ring was not

tight enough. Cleaning or replacing of the o-ring should be considered. As the other spots are below this position. The other leakages may not be caused by a local sealing problem but the gas sucked into the chamber via the top large leak point. So the sealing of the lid had the priority to be solved. Temporarily the problem is solved by cleaning the o-ring with acetone and symmetrical fastening of the bolts.

A.4 Alignment

A.4.1 Laser source

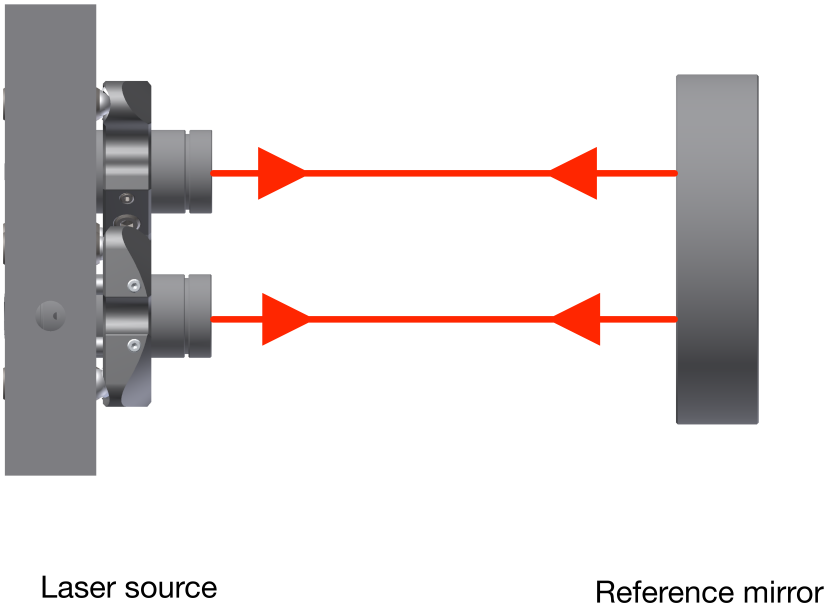

Figure A.7: Alignment of parallel laser beams.

A mirror is used to help achieve the parallelism alignment for the two collimators. Two fibers are connected to the collimators to guide the laser out to the target mirror. Both the target mirror and the invar plate are fixed during the alignment process. By adjusting the mirror mounts to have the reflected laser beams couple back into the collimator, it can be prove that both laser beams are perpendicular to the reference mirror, which meas that the two laser beams are parallel to each other.

A.4.2 Four way beam splitter

To help align the 4 way beamsplitter, the following drawing was made.

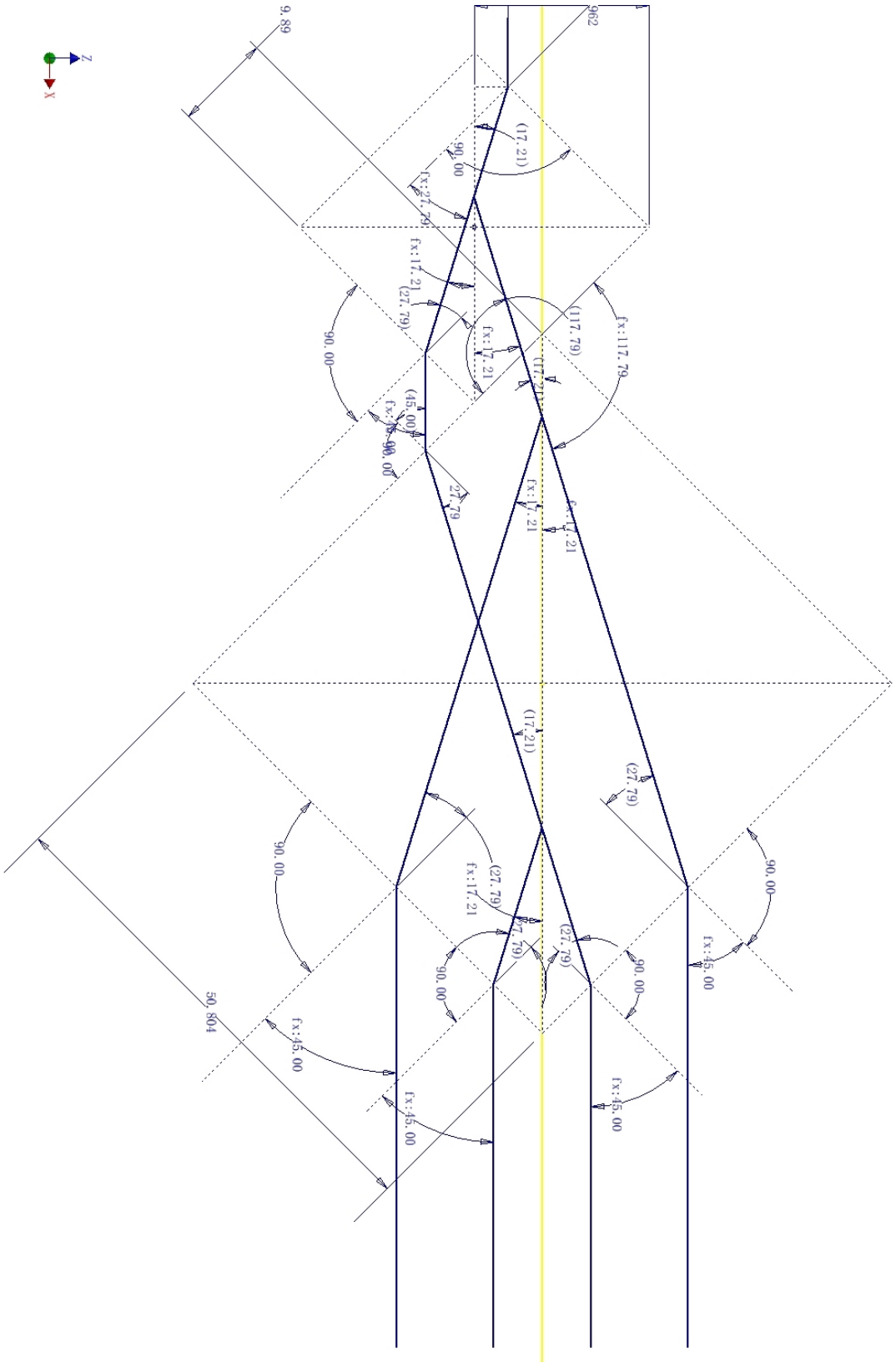

Figure A.8: CAD drawing with notation of geometry dimensions (units in mm).

A.5 Deformation of the chamber

A deformation of the chamber was noticed as the beams drifted away as pressure went down. There are many other factors that may cause the problem. According to the first COMSOL model the deformation was on micrometer level which is not significant comparing to other factors like the change of refractive index. However in a later stage when all the bolts and nuts were used to have a better sealing of the setup to perform a serious measurement, the beams drifted away even before the vacuum pump was started. This drew the attention to the deformation of the chamber again. The COMSOL model was revised, and a more realistic geometry and constrains were modeled to obtain a better simulation.

A.5.1 First COMSOL model

In the first COMSOL model the aluminum chamber is modeled as one part. The optic windows and all bolts and nuts were left out. Assuming that the pressure is exerted on the chamber from every direction, it becomes an isotropic situation. The physical constraints placed are one atmospheric pressure at all outer surfaces and a fixed point constraint at the upper four corners. The maximum deformation is on the level of micrometer which is comparable with the displacement caused by the change of refractive index. So after this first simulation, the deformation of the chamber due to pressure was not determined dominant.

A.5.2 Second COMSOL model

During a test to seal the setup properly, all bolts and nuts were used and fastened. Comparing the signal to the one before the bolts were fastened and after showed that the signal was halved. This drew attention to the deformation of the box again, since the refractive index will not change just because of the extra force from the tighter sealing. A more serious model was made to mimic the realistic situation. The lid and the bottom parts are separated by rubber o-ring which has considerably lower stiffness as compared with aluminum. So, in the second model the chamber was left open to have no support at the top. The physical constraints were the same: one atmospheric pressure at the surfaces, and fixed point constraints at the upper four corners. The simulated results are presented in A.9 - A.12.

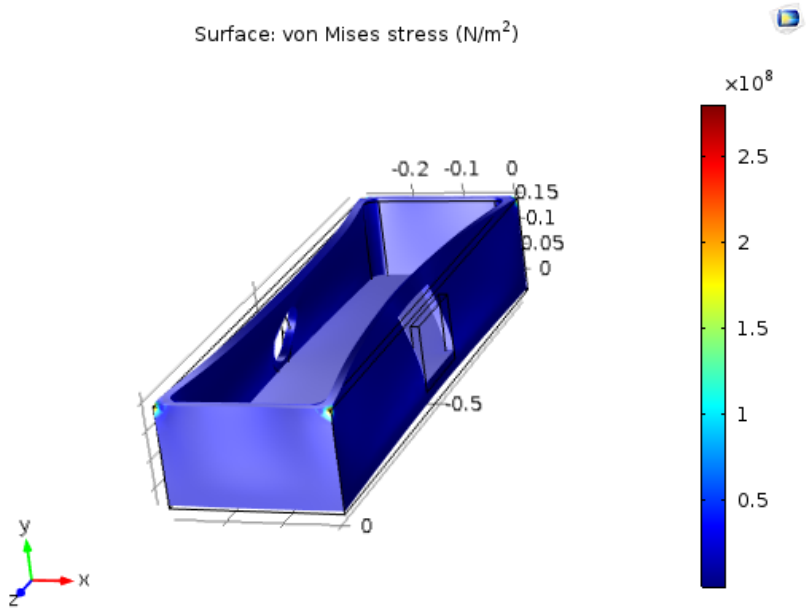

Figure A.9: Exaggerated representation of the deformation of the vacuum box due to the pressure difference.

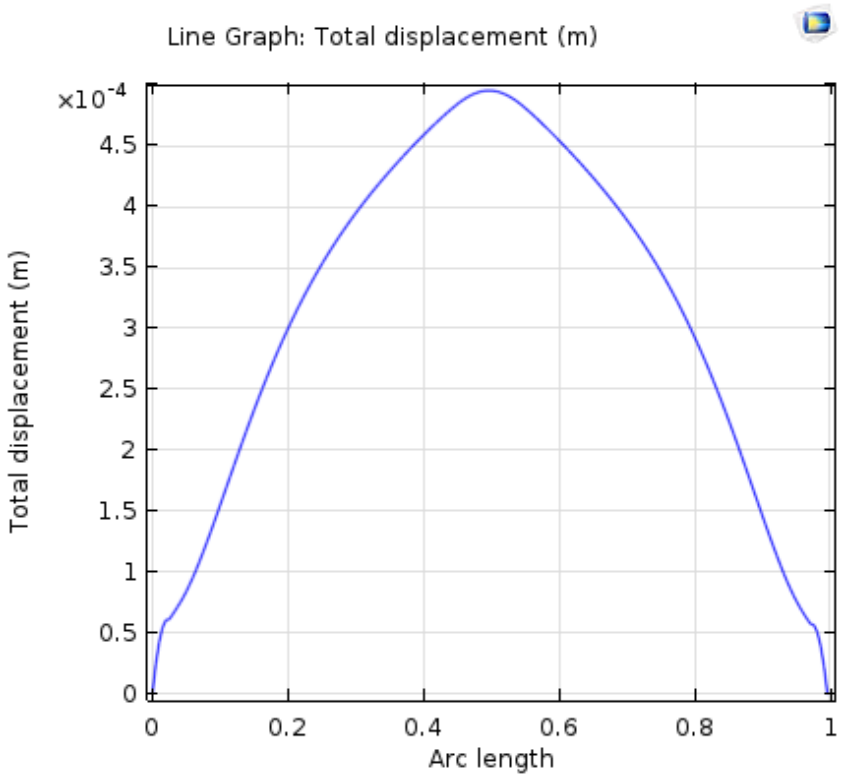

Figure A.10: Exaggerated representation of the deformation of the upper surface of the vacuum box.

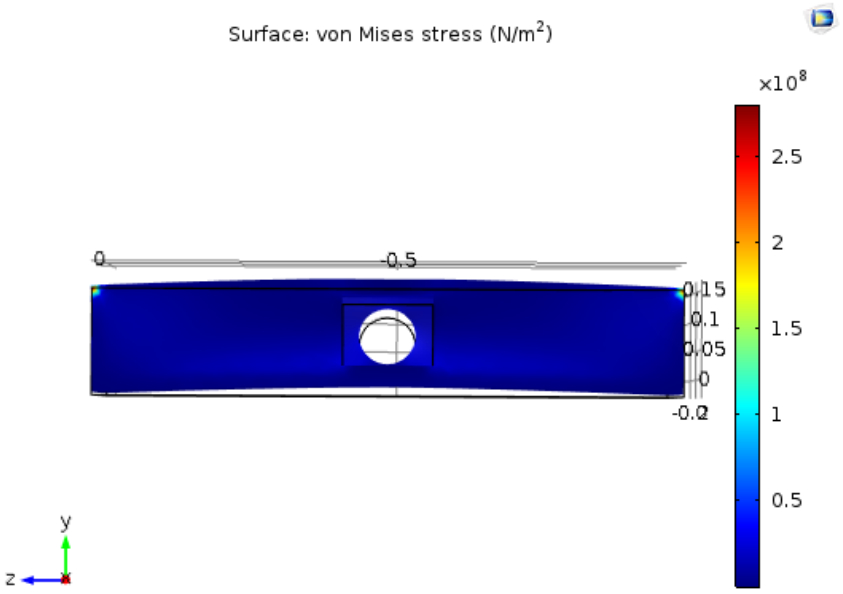

Figure A.11: Exaggerated representation of the deformation of the vacuum box due to pressure difference.

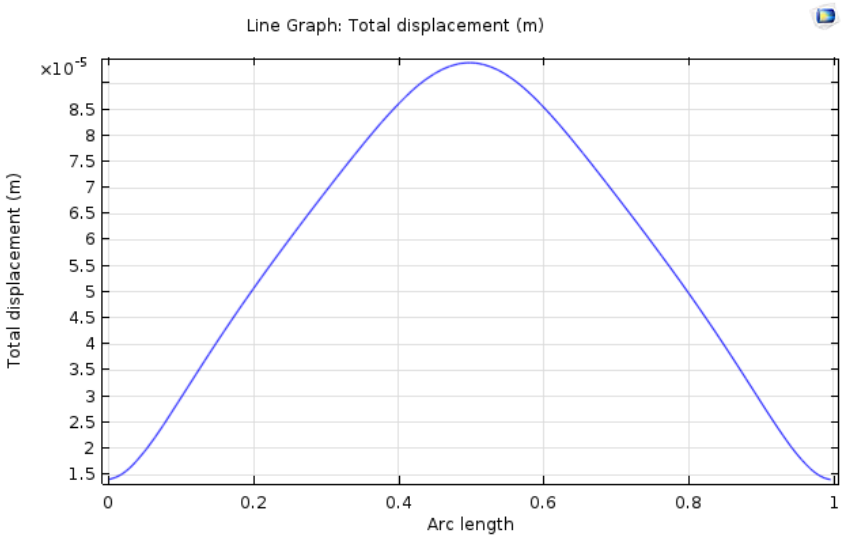

Figure A.12: Exaggerated representation of the deformation of the lower surface of the vacuum box.

The results show that the deformation of the lower surface in the direction of the laser beam could reach the level of millimeters. As the laser travels straight from the source, the pressure induced drift is determined by the slope of the deformation where the laser source is located. Taking the length of the vacuum box into consideration, the beam drift due to this pressure caused deformation is around 0.5 mm which matches the drift as captured by a CCD camera.

A.6 Rotational measurement

As the undesired rotation of the piezo actuator may introduce a large uncertainty during the calibration operation, the magnitude of the rotation has to be characterized by an autocollimator. In this section, the stability of the autocollimator itself is tested. Afterwards, the autocollimator is used to measure the rotation of the actuator as a function of displacement.

A.6.1 Stability test of the autocollimator

In this test the autocollimator is aligned to be perpendicular to a stationary mirror. The result shown below is the stability of the autocollimator itself.

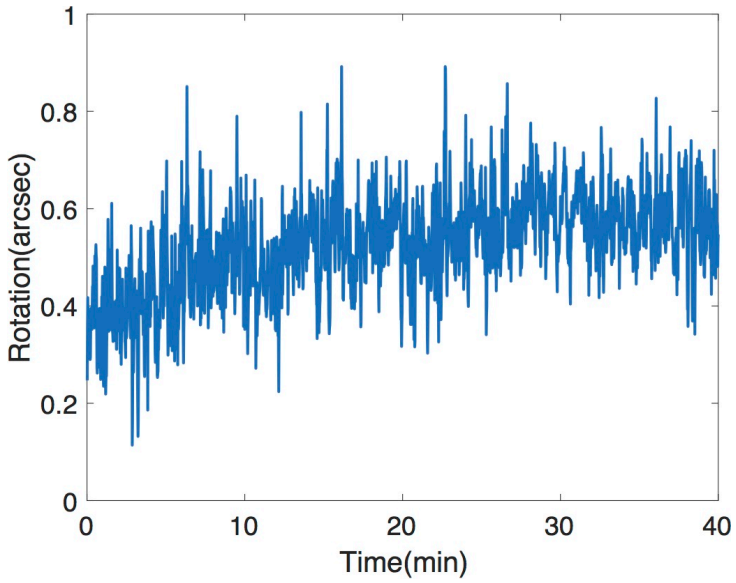

Figure A.13: Stability of the autocollimator in x axis.

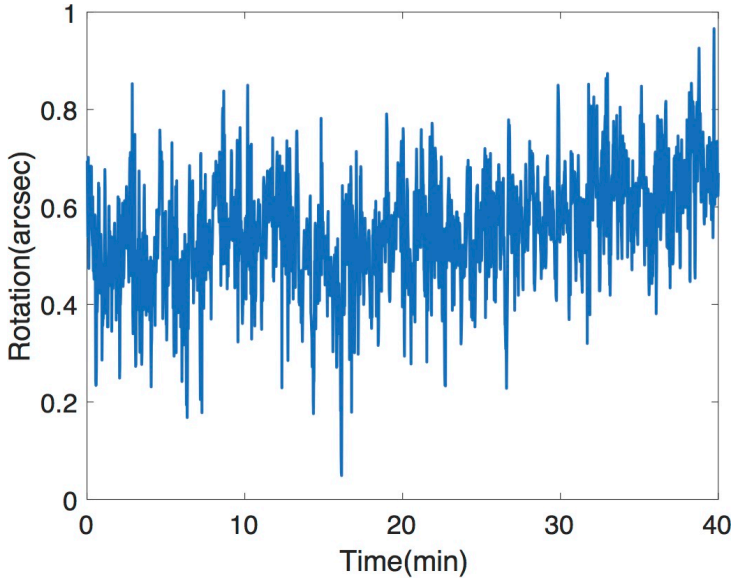

Figure A.14: Stability of the autocollimator in y axis.

It can be seen that the stability can reach below 0.4″ in a period of 1 min, which corresponds to the duration of a single calibration.

A.6.2 Rotation of the piezo actuator

Measurement of the actuator

The behavior of the actuator has an important influence on the calibration measurement. The undesired rotation around x axis and y axis is measured as shown in Figure A.15. Direction convention is indicated by Figure A.16

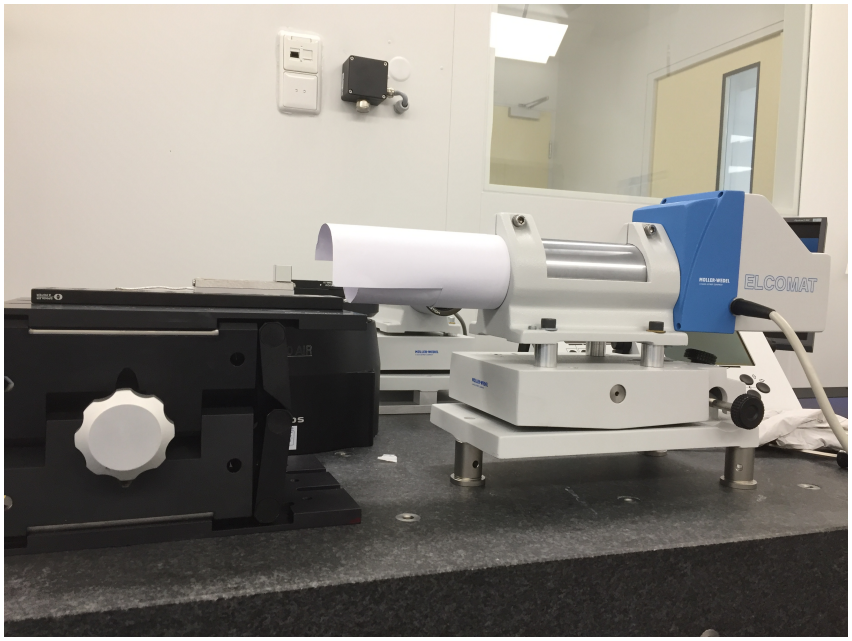

Figure A.15: Configuration of the rotational measurement.

A cubic mirror is glued on the moving bar of the actuator. The autocollimator detects the angle of its front surface. Different tests were made to test the repeatability.

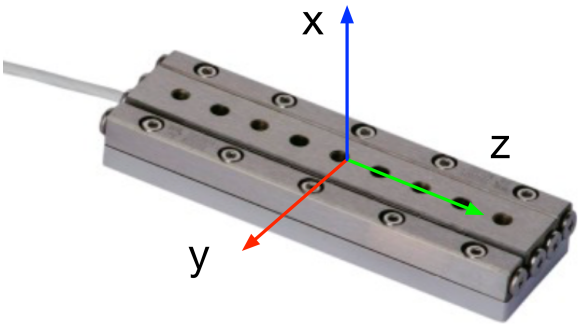

Figure A.16: Direction convention of this rotation measurement.

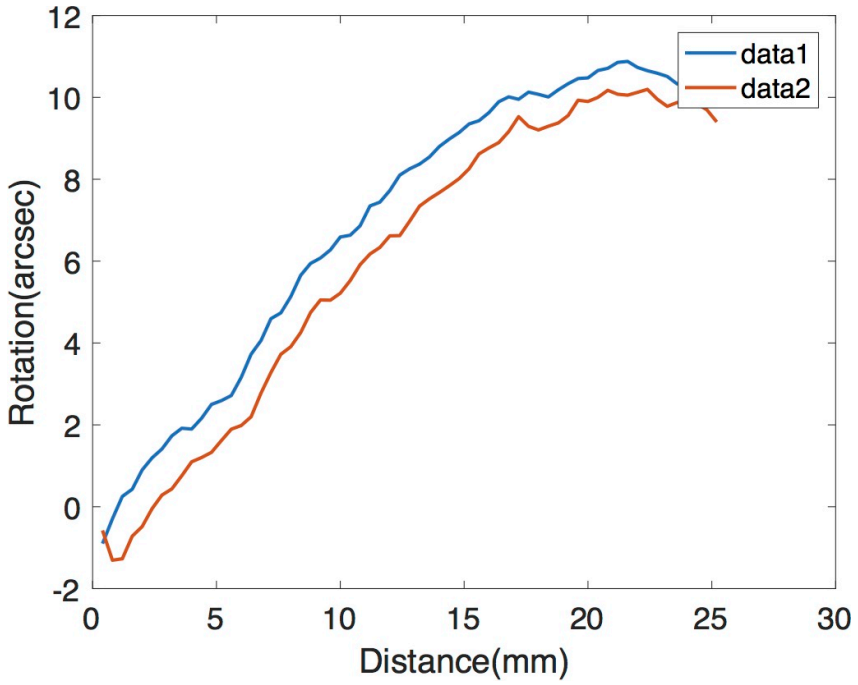

Figure A.17: Rotation of the actuator in x axis as observed along the entire travel range.

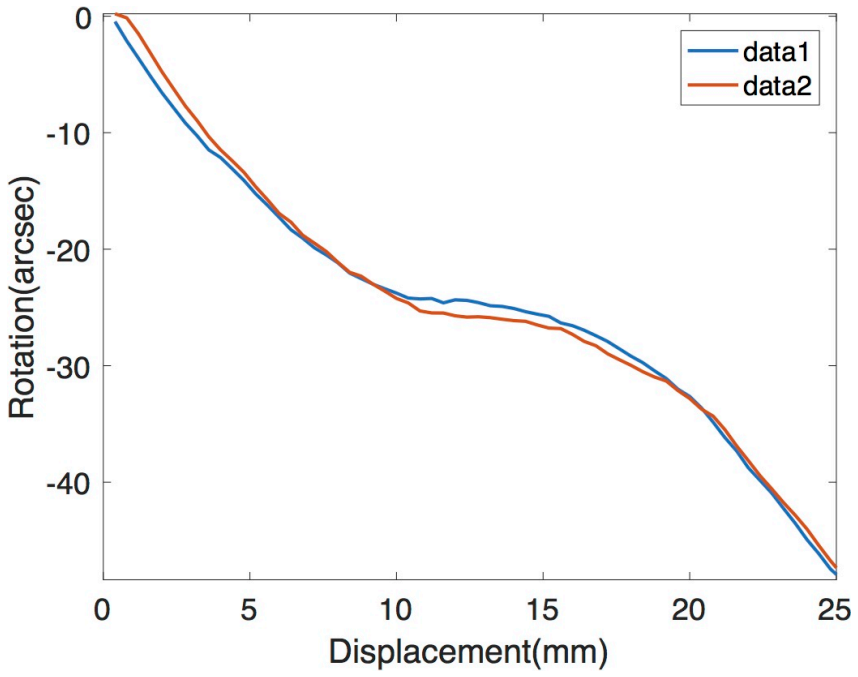

Figure A.18: Rotation of the actuator in y axis as observed along the entire travel range.

It can be seen that the rotation around the y axis is about 50″, while the rotation around the x axis is only 12″. The repeatability is better than 1″ for both axises.

A.7 Calibration experience

A.7.1 Capacitive sensor range

Based on the measurement range specified by the manufacturer of the capacitive sensor, the sensor is able to operate in the following ranges listed in A.2.

Table A.2: Specified aspects of the capacitive sensor manufacturer.

Level	Range (µm)
Extended	125 – 625
Standard	125 – 375
Fine	75 – 125
Ultra fine	20 – 30

During the actual measurement shown in table B.2, it was found that the maximum range of the capacitive sensor, that would give a useful voltage reading, is 266.5 µm. So the following displacement range, listed in table A.3 was determined to be generated by the piezo actuator for calibration.

Table A.3: Designed measurement range for calibration.

Level	Range (µm)
Extended	250
Standard	125
Fine	75
Ultra fine	20

A.7.2 Vibration of the actuator

After the alignment of the calibration setup was performed according to the method discussed in section 5.4, a test measurement was performed of the actuator. In this test the two channels Interferometer 1 and Interferometer 2 are used to measure the motion of the target.

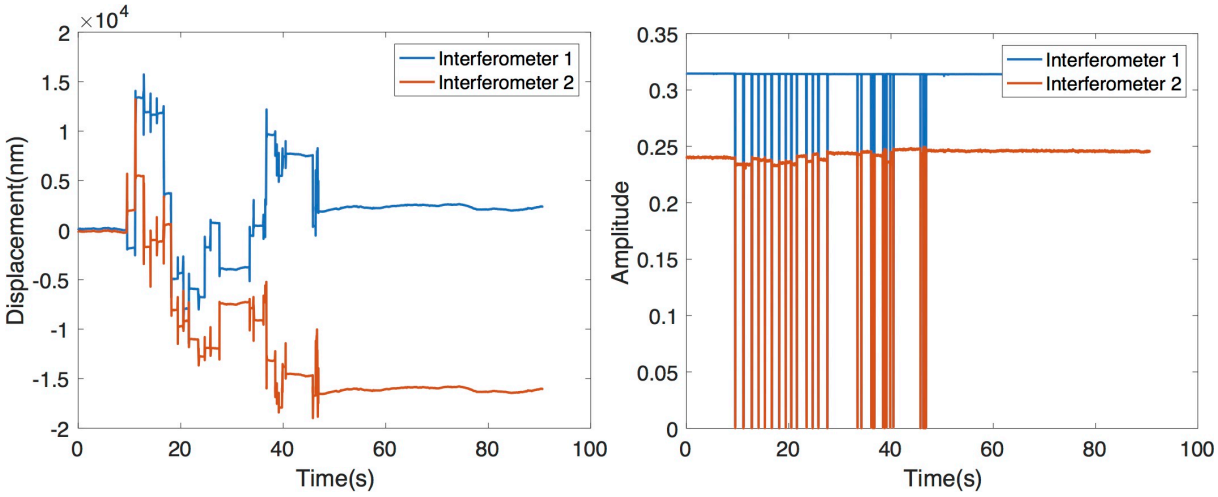

(a) Displacement interpreted by interferometer.

(b) Corresponding amplitude of the interferometer channels.

Figure A.19: Result of a test measurement.

The displacement measured by the interferometer is of the order of 10 µm which is far less than the actual displacement generated by the stage. The difference between the two channels is far too large than was expected. According to the amplitude recorded at the same time, it is observed that during the motion of the stage, the amplitude dropped significantly. At some period it was even close to zero. This drop in amplitude may lead to the lose of the tracking of the phase change detected by the interferometer. The drop in intensity is caused by the vibration of the stage. Eventually, the laser will be misaligned. To confirm this assumption, another test was made. This time the actuator control loop was changed to quite control mode which will produce less noise and vibration. The result is shown in Figure A.20. The displacement was set to be 50 µm and the speed was 2 µm s^{-1}.

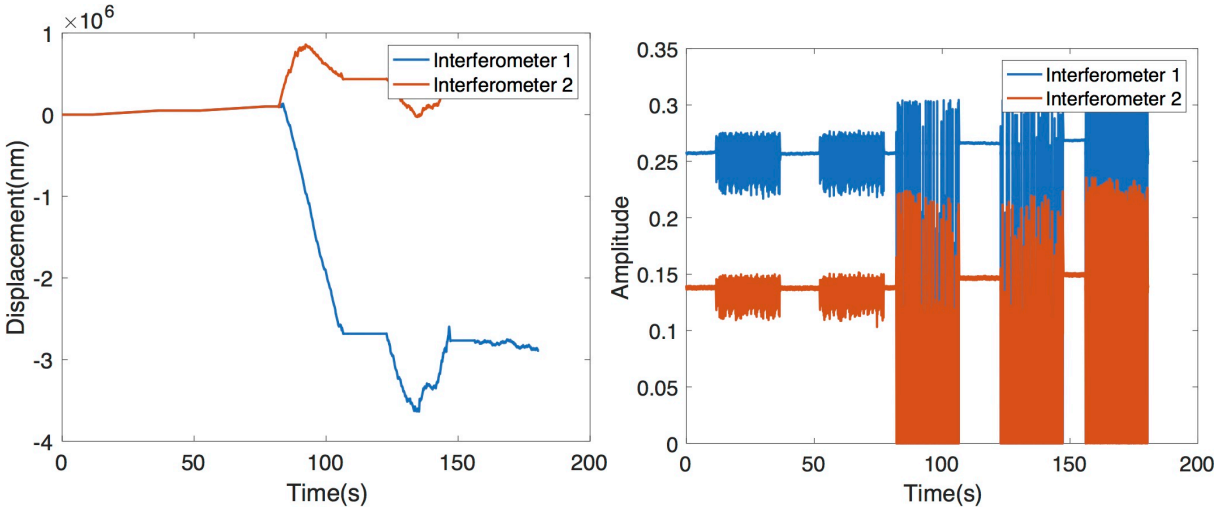

(a) Displacement measured by interferometer (quiet mode).

(b) Corresponding amplitude of the interferometer channels (quiet mode).

Figure A.20: Feasibility test.

From these two figures it could be seen clearly that the misinterpreting of displacement is related to the drop of the amplitude. For the two displacements at quite mode low vibrations are expected, and the drop in amplitude is not significant. The two interferometer channels' output are strongly

correlated with small offset. The displacements produced afterward at normal mode generate large vibration and loud noise,which leads to the drop in amplitude to zero. The phase can not be tracked and is lost resulting in the wrong displacement as interpreted by the data processing procedure.

A.7.3 The optimal control frequency for the actuator

For the currently used actuator, there are two main factors influencing the vibrations: velocity and control loop frequency. A sets of experiments were performed to determine the setting with lowest vibration while still possible to perform calibration.

There are four mode of the actuator controller: closed loop, closed loop(quiet), stepped and manual voltage. Among all of them the closed loop mode is the ideal mode, as it can control the actual displacement, speed and acceleration. As compared to the quiet mode, closed loop allows the user to change the frequency.

In order to find the optimal control frequency, other parameters like speed, displacement and acceleration are kept as constant. Five different frequencies between the lowest 50 Hz to the highest 18 500 Hz are selected for the test. In Figure A.21b, five regions of motion can be distinguished clearly based on the vibration reflected in the amplitude recording. It can be seen that the vibration amplitude increases as the frequency increases. As the interpreted displacement drifts away for the second region of motion, the lowest operating frequency of 50 Hz is determined as the optimal frequency.

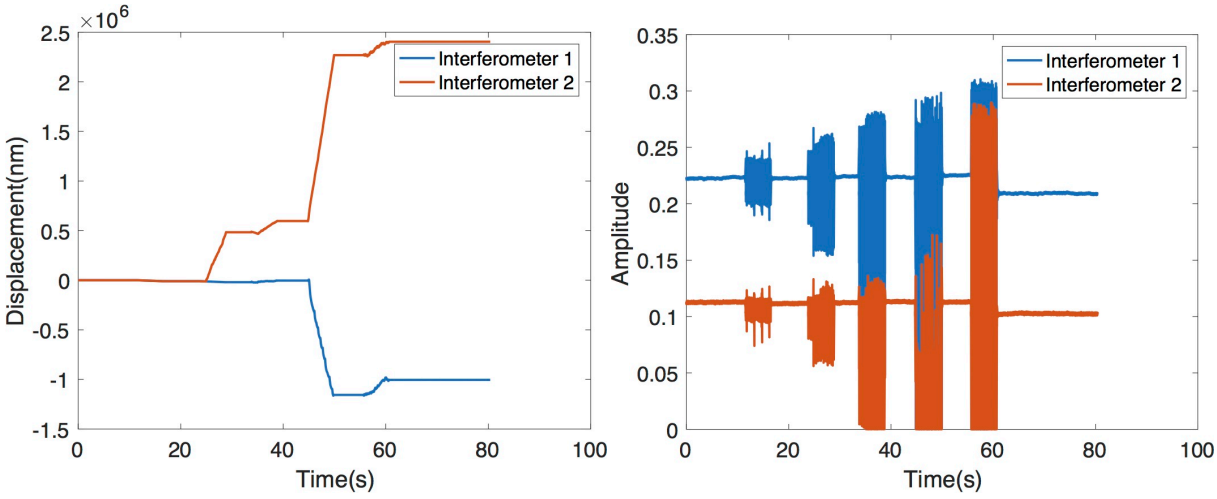

(a) Displacement measured by the interferometer.

(b) Corresponding amplitude of the two interferometer channels.

Figure A.21: Test to find the optimal close loop frequency. Five frequencies: 50 Hz, 100 Hz, 200 Hz, 500 Hz, 5000 Hz are tested and can be distinguished from the amplitude plot. In Figure (a), during the second displacement, the visible change shows the interpreted displacement is of the level of millimeters which is an order higher than the actual displacement. In figure (b), the amplitude recording shows that for higher frequencies larger vibrations will be introduced during the motion.

A.7.4 The optimal velocity for the actuator

A similar test was performed to find the optimal velocity in order to have motion with lowest vibration. Different velocity settings ranging from $0.2\,\mu m\,s^{-1}$ to $200\,\mu m\,s^{-1}$ were tested.

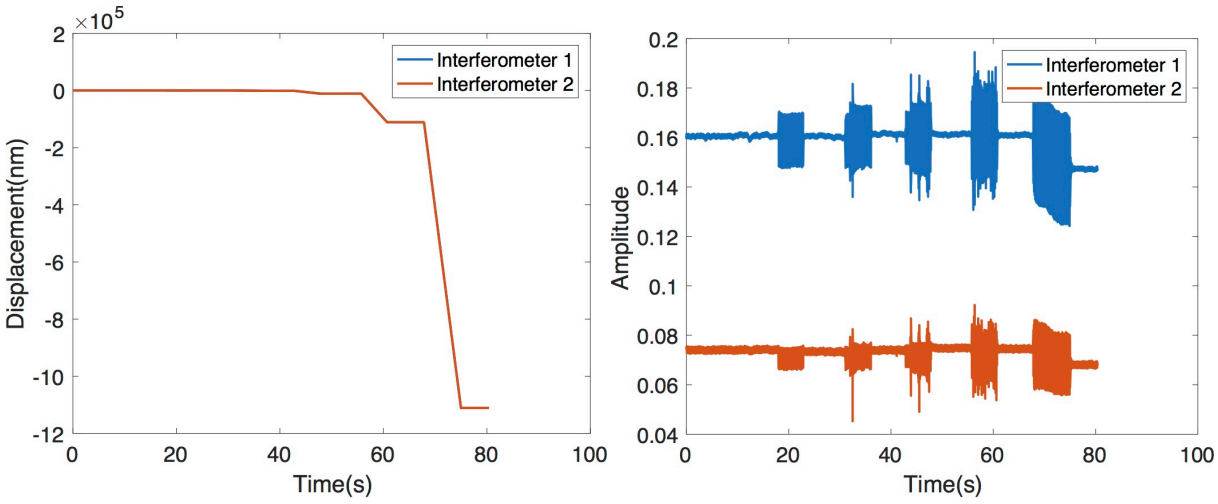

(a) Displacement measured by interferometer.

(b) Corresponding amplitude of the interferometer channels.

Figure A.22: Test to find the optimal velocity setting. Different velocity settings ranging from $0.2\,\mu m\,s^{-1}$ to $200\,\mu m\,s^{-1}$ were tested.

From the displacement plot, it can be deduced that the displacements are all interpreted correctly. And the vibrations as observed from the amplitude recordings only shows a small difference which doesn't influence the result too much. So all the velocity settings can be used at a frequency of 50 Hz based on requirements. A speed of $2000\,\mu m\,s^{-1}$ could not be reached for this frequency setting.

A.8 Overall operation description

A.8.1 Operation of the system

There are some things to pay attention to, in order to operate the interferometer with a nice experience of measurement

- The bolts and nuts that are used to seal the gap between the lid and the vacuum chamber should be fastened symmetrically around the rectangular lid.
- The bolts should not be fastened too much at one time. Instead of having a tightly fastened connection, at the beginning bolts can be fastened at a medium level. When the pressure goes below 1000 mbar, bolts can be fastened more easily as the pressure goes down.
- As the o-ring is compressed a lot during the evacuation process. It will be too late to release the bolts when the chamber is completely vented. If that happens, the bolts will withstand too much force especially since it can not be guaranteed that all bolts are sharing the same amount of load. So, when the pressure goes up to 1 mbar all bolts can be untightened a little bit. As pressure goes up it is necessary to check again and again to make sure the threads will not be damaged due to the large force on the bolts by the vacuum chamber.

A.8.2 Turn on the ion pump

The ion pump has to work below 1×10^{-5} mbar. As the cavity in the nearby chamber is in vacuum most of the time, the configuration before the ion pump start should be that valve 1, which connects

to the turbo pump is open and valve 2 connecting to the ion pump is closed. When the pressure reaches 1×10^{-4} mbar valve 2 can be opened.

Appendix B

Data sheet

B.1 Thermal expansion coefficient

Table B.1: Thermal expansion coefficients of materials.

Material	Thermal expansion coefficient µm/(m K)
Aluminum	22.2
Stainless steel (304)	17.3
Brass	19
N-BK7	7.1
Invar	1.5
Fused silica	0.57
Zerodure	0.07

B.2 Capacitive sensor measurement

Table B.2: Measurement of the working range of the capacitive sensor.

In/Out of range	Sensor output (V)	Controller output (V)	position of the stage (nm)
out	10.76	150.54	18,019,544
out	10.76	148.51	18,013,965
out	10.76	142.52	18,008,041
out	10.77	135.86	18,001,440
in	10.49	131.43	17,997,157
in	...	...	...
in	−10.36	-140.59	17,723,372
out	−10.6	-149.83	17,672,901
out	−10.6	-149.78	17,621,799
out	−10.6	-149.75	17,572,157

B.3 Capacitive sensor

Data sheet - LION Precision capacitive sensors

Extended range

Proby body	Sensor size	Extended range (µm)	Linearity error (% full scale)	Resolution RMS (nm)
C1, C2	A	250 to 2.250	0,45	20
C30, C36	B	250 to 1.500	0,20	20
C30, C36	D	125 to 625	0,20	9
C3, C5, C6	D	125 to 625	0,15	9
C3, C5, C6	E	N.A.	-	-
C3, C5, C6, R3, N2	F	60 to 140	0,85	7
R2	H	3.000 to 9.000	0,25	180

Standard range

Proby body	Sensor size	Standard range (µm)	Linearity error (% full scale)	Resolution RMS (nm)
C1, C2	A	500 to 1.000	0,20	12
C30, C36	B	250 to 750	0,15	10
C30, C36	D	125 to 375	0,10	10
C3, C5, C6	D	125 to 375	0,10	9
C3, C5, C6	E	100 to 200	0,15	10
C3, C5, C6, R3, N2	F	50 to 100	0,30	5
R2	H	5.000 to 7.500	0,20	100

Fine range

Proby body	Sensor size	Fine range (µm)	Linearity error (% full scale)	Resolution RMS (nm)
C1, C2	A	225 to 275	0,20	1,5
C30, C36	B	125 to 175	0,20	2,0
C30, C36	D	75 to 125	0,15	2,4
C3, C5, C6	D	75 to 125	0,15	2,0
C3, C5, C6	E	75 to 100	0,15	4,0
C3, C5, C6, R3, N2	F	20 to 30	0,25	1,5
R2	H	-	-	-

Ultrafine range

Proby body	Sensor size	Ultrafine range (µm)	Linearity error (% full scale)	Resolution RMS (nm)
C1, C2	A	-	-	-
C30, C36	B	-	-	-
C30, C36	D	20 to 30	0,20	0,4
C3, C5, C6	D	20 to 30	0,15	0,4
C3, C5, C6	E	-	-	-
C3, C5, C6, R3, N2	F	-	-	-
R2	H	-	-	-

Probe bodies

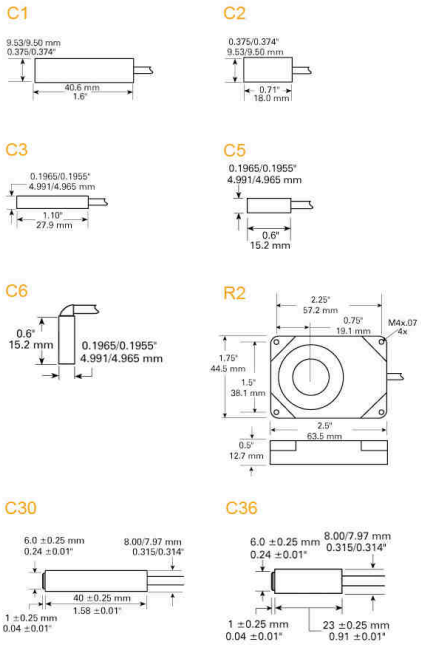

Sensor sizes

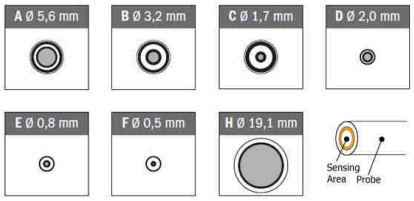

Unique resolutions with custom calibrations: Some examples

Sensing area	Range (µm)	Near gap (µm)	Resolution RMS (nm)	Bandwidth (Hz)	Notes
B	10	20	0,040	1.000	Used larger "B" sized sensing area for "D" ultrafine calibration and decreased bandwidth
C	2	10	0,097	13.700	Decreased range
D	50	75	0,126	122	Decreased bandwidth
C	10	10	0,144	14.000	Decreased near gap
B	250	20	0,529	1.100	Decreased near gap, custom range, decreased bandwidth
A	2.000	25	15,50	15.400	Decreased near gap

IBS Precision Engineering
Tel: +31 40 2901270
E-mail: info@ibspe.com
Internet: www.ibspe.com

B.4 Control module for capacitive sensor

Specifications

Power Requirements	±15 VDC ± 10% @ 130 mA each
Linearity Error	±0.3% Full Scale or better, dependent on calibration
Bandwidth	Static to 10KHz ±5% -3dB: 20 KHz Typical
Ranges	Dual; Selectable per calibration (DMT12/22 Only)
Meets ANSI/ASME B5.54 Standard	Yes
Probe Interchangeability	Yes, typical sensitivity variation 2% for same probe model
Operating Temperature	4°-66°C 40°-150°F
Thermal Stability	0.3% F.S.
Oscillator Frequency	Probe cable: < 12 feet - 1MHz, > 12 ft - 500KHz
Output Impedance	0Ω
Noise Output	6 mV p-p @ 10KHz B.W.

B.5 Piezo actuator

Linear Positioners

SLC-2475

Nanometer Precision Linear Positioner

resolution	travel range
< 1nm	49 mm
normal load	**non magnetic**
30 N (3 kg)	available
vacuum	**size**
down to 10^{-11} mbar	75x24x10.5 mm^3

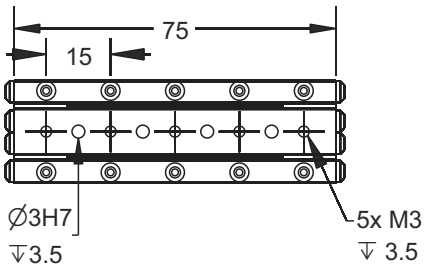

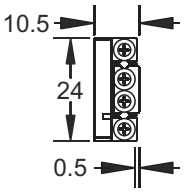

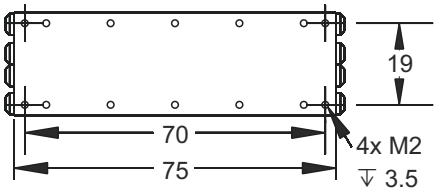

Linear dimensions are given in mm.

SLC-2475

Mechanical Properties	
blocking force F_B	> 3.5 N
max. normal force F_N	30 N
max. lift force F_L	> 1.5 N
positioner dimension	75 x 24 x 10.5 mm[3]
weight	90 g
pitch torque M_P	18.1 N m
yaw torque M_Y	18.1 N m
roll torque M_R	3.9 N m

Positioning	
travel	≙ 24.5 (49) mm
step width	1 - 1,500 nm①
scan range	> 1.5 µm
scan resolution	< 1 nm
velocity	> 20 mm/s
max. frequency	18.5 kHz

Closed-Loop with -S	
sensor resolution	1 nm
repeatability	≙ 75 nm②

Closed-Loop with -L③	
sensor resolution	4 nm
closed loop resolution	50 nm (H)CU 4 nm MCS
repeatability	≙ 1 µm (H)CU ≙ 150 nm MCS

Closed-Loop with -M③	
sensor resolution	100 nm
closed loop resolution	500 nm (H)CU 100 nm MCS
repeatability	≙ 2.5 µm (H)CU ≙ 0.5 µm MCS

Materials and Vacuum Options④
steel base (-ST), titanium base (-TI)
non magnetic materials (-NM)
black anodized (-BK)
integrated connecting elements (-O)
external support for increased M_Y, M_R (-W)
high precision bearing (-P)
increased blocking force (-D, +1.5 N)
-HV (10^{-6} mbar), -UHV / -UHVT (10^{-11} mbar)

① for low-vibration mode (-LV), for scan-mode < 1 nm, otherwise 50 - 1,500 nm

② measured over the complete travel range, for shorter travel much better

③ with mechanical end stops, 3 mm reduced travel

④ positioner dimensions, mounting holes and travel range may vary and can be customized

⑤ all holes M1.6, no dowel holes, screwing depth: min. 3 mm, max. 3.5 mm

B.6 Ion pump (REVION 35)

Technical Data

	REVION® 35	REVION® 55	REVION® 75
■ Flange connection*	DN40CF	DN63CF	DN100CF
■ Dimensions (L x W x H)	235 x 130 x 194 mm	235 x 130 x 206 mm	235 x 130 x 208 mm
■ Weight	15 kg	16 kg	17 kg
■ Nominal pumping speed (N_2)	32 l/s	52 l/s	67 l/s
■ UHV_9 pumping speed** (N_2)	24 l/s	37 l/s	47 l/s
■ Start pressure	1×10^{-4} mbar		
■ Ultimate pressure	$\leq 1 \times 10^{-11}$ mbar		
■ Bakeout temperature	■ With magnet/cable: 250 °C (in operation) ■ Without magnet/cable: 450 °C		
■ HV connection	10 kV SHV		
■ Pumping element	Conventional diode		
■ HV cable	With blade receptacle; Length: 3, 6, 10 m		
■ Accessories (optional)	Heating element		

* QCF flanges increase the conductance and the pumping speed by up to 15 %

** Pumping speed at a pressure of 1×10^{-9} mbar

Technical Data REVION® CU-100

■ Power supply	24 V DC
■ Output voltage	Max. 7 kV, adjusted to pressure range
■ Max. power	100 W
■ Accuracy of the pressure display	± 30 % of reading (10^{-5} to 10^{-9} mbar)
■ Features	■ Easy and safe interlock solution ■ No fan
■ Histogram	Current/pressure curve, 24 h display
■ Set points	2 (configurable)
■ Interface	RS232
■ Dimensions (L x W x H)	325 x 120 x 102 mm
■ Weight	Ca. 2.5 kg
■ Additional equipment	Connection cable

Controller
REVION® CU-100

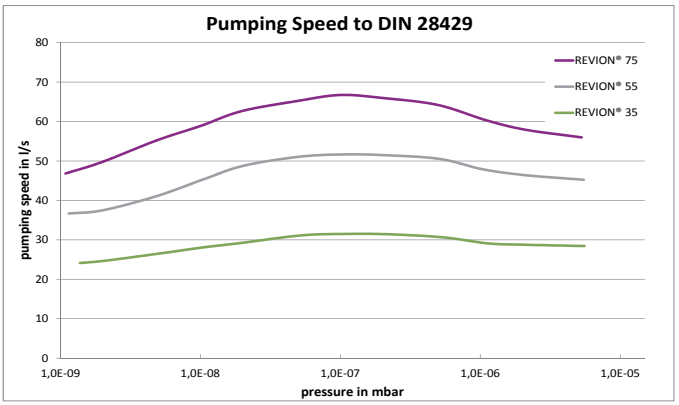

Connection cable for
REVION® CU-100

201501

Also available as noble gas stable versions in our **REVION®** *noble* series.

B.7 Circulator (AC150)

Section 2 General Information

Description and Intended Use

The Thermo Scientific ADVANCED Series of Heated Immersion Circulators are used with refrigerated and heated baths. All immersion circulators can pump to an external system. All circulators have a digital display and easy-to-use touch pad, five programmable setpoint temperatures, acoustic and optical alarms, and offer adjustable high temperature protection.

The circulator is designed for use in a clean laboratory environment and in accordance with the Letter of Compliance located at the end of this manual.

ADVANCED Heated Immersion Circulators

	AC150	AC200
Temperature Range °C °F	Ambient +13 to +150 Ambient +23 to +302	Ambient +13 to +200 Ambient +23 to +392
Temperature Stability °C	±0.01	±0.01
Heater Capacity 230V/115V watts	2000/1200	2000/1200
Circulator Dimensions (H x W x D) mm inches	372 x 165 x 199 14.6 x 6.4 x 7.8	372 x 165 x 199 14.6 x 6.4 x 7.8
Reservoir Depth Requirement mm inches	150 5.9	150 5.9
Fill Level mm (from top of reservoir)	57..22	57..22
Required Reservoir Depth mm	150	150
Net Weight kg/lb	4.2/9.3	4.2/9.3
Pumping Capacity Max flow rate lpm/gpm Max pressure (mbar/psi) Max suction Pump speed steps	 20/5.3 475/6.89 330/4.85 3	 20/5.3 475/6.89 330/4.85 3
Electrical Requirements (Voltage ±10%)	100 V/50 Hz 100 V/60 Hz or 115 V/60 Hz or 230 V/50..60 Hz	100 V/50 Hz 100 V/60 Hz or 115 V/60 Hz or 230 V/50..60 Hz
Connectivity Remote sensor port USB port Multi function port RS232/RS485/Ethernet/LAN Analog I/O	 Yes No No Optional No	 Yes Yes Yes Optional Optional

- Performance specifications established in accordance with DIN 12876 (using water at 70°C).
- Lower temperature ranges available with supplemental cooling.
- The maximum bath wall thickness for circulators that have a factory installed clamp is 26 mm.
- Thermo Fisher Scientific reserves the right to change specifications without notice.

B.8 Turbo pump (HiCube 80 CF)

13 Technical data and dimensions

13.1 General

Basic principles for the Technical Data of Pfeiffer Vacuum Turbopumps:

- Recommendations of PNEUROP committee PN5
- ISO 21360; 2007: "Vacuum technology - Standard methods for measuring vacuum-pump performance - General description"
- ISO 5302; 2003: "Vacuum technology - Turbomolecular pumps - Measurement of performance characteristics"
- Ultimate pressure: using a test dome and a 48 hrs. period of baking out
- Gas throughput: water cooling; backing pump = rotary vane pump (10 m^3/h)
- Cooling water consumption: at max. gas throughput, cooling water temp. 25 °C
- Integral leak rate: using a Helium concentration of 100 %, period 10 s
- Sound pressure level: Distance 1 m to the pump

Conversion table: pressure units

	mbar	bar	Pa	hPa	kPa	Torr mm Hg
mbar	1	$1 \cdot 10^{-3}$	100	1	0.1	0.75
bar	1000	1	$1 \cdot 10^{5}$	1000	100	750
Pa	0.01	$1 \cdot 10^{-5}$	1	0.01	$1 \cdot 10^{-3}$	$7.5 \cdot 10^{-3}$
hPa	1	$1 \cdot 10^{-3}$	100	1	0.1	0.75
kPa	10	0.01	1000	10	1	7.5
Torr mm Hg	1.33	$1.33 \cdot 10^{-3}$	133.32	1.33	0.133	1

1 Pa = 1 N/m^2

Conversion table: gas throughput units

	mbar·l/s	Pa·m^3/s	sccm	Torr·l/s	atm·cm^3/s
mbar·l/s	1	0.1	59.2	0.75	0.987
Pa·m^3/s	10	1	592	7.5	9.87
sccm	$1.69 \cdot 10^{-2}$	$1.69 \cdot 10^{-3}$	1	$1.27 \cdot 10^{-2}$	$1.67 \cdot 10^{-2}$
Torr·l/s	1.33	0.133	78.9	1	1.32
atm·cm^3/s	1.01	0.101	59.8	0.76	1

13.2 Technical data

Parameter	HiCube 80 Eco	HiCube 80 Eco	HiCube 80 Eco
Flange (in)	DN 63 ISO-K	DN 63 CF-F	DN 40 ISO-KF
Pumping speed for N_2	67 l/s	67 l/s	35 l/s
Pumping speed backing pump at 50 Hz	0.50 m^3/h	0.50 m^3/h	0.50 m^3/h
Ultimate pressure	$< 1 \cdot 10^{-7}$ hPa	$< 1 \cdot 10^{-7}$ hPa	$< 1 \cdot 10^{-7}$ hPa
Sound pressure level	≤ 52 dB (A)	≤ 52 dB (A)	≤ 52 dB (A)
Mains requirement	115 V, 50/60 Hz; 230 V, 50/60 Hz	115 V, 50/60 Hz; 230 V, 50/60 Hz	115 V, 50/60 Hz; 230 V, 50/60 Hz
Mains requirement: power consumption	230 W	230 W	230 W
Weight	17 kg	17 kg	17 kg
Backing pump	MVP 015	MVP 015	MVP 015

Acronyms

AOM Acousto-optic modulator.

BIPM International Bureau of Weights and Measures.

BS Beamsplitter.

CTE coefficient of thermal expansion.

EOM Electrico optical modulator.

H Half wave plate.

He-Ne Helium-Neon.

LDBS Lateral displacement beamsplitter.

LP Low-pass.

M Mirror.

PBS Polarizing beamplitter.

PD Photo detector.

PDH Pound–Drever–Hall.

PID proportional-integral-derivative.

Q Quarter wave plate.

RR Retro reflector.

TNO Netherlands Organisation for Applied Scientific Research.

TU Delft Delft University of Technology.

UHV Ultra high vacuum.

UV Ultra violet.

VSL Van Swinden Laboratory, the Netherlands' National Metrology Institute.

Bibliography

[1] J. D. Ellis, *Optical metrology techniques for dimensional stability measurements*. PhD thesis, TU Delft, Delft University of Technology, 2010.

[2] A. S. van de Nes and D. Voigt, *Picometer Resolution Heterodyne Interferometry for Short to Medium Term Dimensional Stability Measurments*. Universitätsbibliothek Ilmenau, 2014.

[3] BIPM, "What is metrology?," 2004.

[4] R. P. Crease, "Critical point chinese metrology," *Physics World*, p. 19, September 2011.

[5] "The international metre commission (1870-1872)."

[6] P. Tipler and G. Mosca, *Physics for Scientists and Engineers*. No. pts. 1-33 in Physics for Scientists and Engineers, W. H. Freeman, 2007.

[7] S. Ezekiel, "Res.6-005 understanding lasers and fiberoptics."

[8] M. Okaji and H. Imai, "A practical measurement system for the accurate determination of linear thermal expansion coefficients," *Journal of Physics E: Scientific Instruments*, vol. 17, no. 8, p. 669, 1984.

[9] H. Kogelnik and T. Li, "Laser beams and resonators," *Appl. Opt.*, vol. 5, pp. 1550–1567, Oct 1966.

[10] E. D. Black, "An introduction to pound–drever–hall laser frequency stabilization," *American Journal of Physics*, vol. 69, no. 1, pp. 79–87, 2001.

[11] R. W. P. Drever, J. L. Hall, F. V. Kowalski, J. Hough, G. M. Ford, A. J. Munley, and H. Ward, "Laser phase and frequency stabilization using an optical resonator," *Applied Physics B*, vol. 31, pp. 97–105, Jun 1983.

[12] B. Edlén, "The refractive index of air," *Metrologia*, vol. 2, no. 2, p. 71, 1966.

[13] K. Birch and M. Downs, "An updated edlén equation for the refractive index of air," *Metrologia*, vol. 30, no. 3, p. 155, 1993.

[14] K. Birch and M. Downs, "Correction to the updated edlén equation for the refractive index of air," *Metrologia*, vol. 31, no. 4, p. 315, 1994.

[15] PFEIFFER, *Introduction to high and ultra high vacuum production*.

[16] "Cleaning aluminum for vacuum applications."

[17] R. Reid, "Cleaning for vacuum service," tech. rep., Cern, 1999.

[18] M. Pisani, A. Yacoot, P. Balling, N. Bancone, C. Birlikseven, M. Çelik, J. Flügge, R. Hamid, P. Köchert, P. Kren, U. Kuetgens, A. Lassila, G. B. Picotto, E. Şahin, J. Seppä, M. Tedaldi, and C. Weichert, "Comparison of the performance of the next generation of optical interferometers," *Metrologia*, vol. 49, no. 4, p. 455, 2012.

[19] S. Wetzels, *Laser based displacement calibration with nanometre accuracy*. Technische Universiteit Eindhoven, 1998.

[20] S. J. A. G. Cosijns, *Displacement laser interferometry with sub-nanometer uncertainty*. Technische Universiteit Eindhoven, 2004.

[21] Y.-C. Wang, L.-H. Shyu, and C.-P. Chang, "Fabry–pérot interferometer utilized for displacement measurement in a large measuring range," *Review of Scientific Instruments*, vol. 81, no. 9, p. 093102, 2010.

[22] M. Çetintaş and M. Çelik, "Long-range displacement measurements using sideband modulation method," *Measurement Science and Technology*, vol. 28, no. 7, p. 075202, 2017.

[23] M. M. H. David Dornfeld, *precisionMaunfacturing*. Springer, 2007.

[24] H. Haitjema, P. Schellekens, and S. Wetzels, "Calibration of displacement sensors up to 300 μm with nanometre accuracy and direct traceability to a primary standard of length," *Metrologia*, vol. 37, no. 1, p. 25, 2000.

[25] Lion Precision, *Error Sources: Probe/Target Angle*, lt02-0012 ed., March 2004.